Durham E-Theses

Investigation of Anion Resonances Using Photoelectron Spectroscopy and Density Functional Theory

MENSA-BONSU, GOLDA

Investigation of Anion Resonances Using Photoelectron Spectroscopy and Density Functional Theory

A thesis submitted in partial fulfilment for the degree of Doctor of Philosophy in Chemistry

Golda Mensa-Bonsu

Department of Chemistry

Durham University

2020

ABSTRACT

The structure and dynamics of temporary excited states of anions (resonances) has been probed using a combination of photoelectron (PE) spectroscopy and computational methods. Such resonances are important in understanding electron-driven chemistry. Here, photoexcitation from an anion to an excited state of the anion that lies in the electronic continuum is closely related to the analogous electron impact resonances. A particular emphasis is placed on how non-covalent interactions in clusters affect these dynamics. Two-dimensional (2D) PE spectroscopy is employed which provides fingerprints of resonance dynamics. Additionally, computational methods are used to aid the interpretation of experimental results and to lay a foundation for future studies. To demonstrate the applicability of these methods, we have probed a range of different anionic systems of relevance to astro-, bio-, and plasma-chemistry as well as fundamental chemical reaction dynamics. We studied the dynamics of anthracene resonances, showing that resonances overall decay by electron detachment. Time-dependent density-functional theory (TDDFT) calculations in conjunction with a stabilisation method could assign all observed resonances. For the *para*-benzoquinone radical anion, the addition of a single water molecule was found to lead to a dramatic enhancement in the ability for resonances to form the ground-state anion. Larger water clusters similarly showed that ground-state formation was facile. Clusters of the *para*-benzoquinone radical with other *para*-benzoquinone molecules showed dissociation dynamics following the excitation of a resonance. Finally, the cluster of the iodide anion and trifluoromethyl iodide was studied as a reactive intermediate in an S_N2 reaction, in which the stereochemistry has been reversed from the traditional backside attack to a frontside attack pre-reaction complex. Overall, the interplay between TDDFT and 2D PE spectroscopy is shown to provide exquisite insight into the electronic structure of complex anionic clusters and their resonances, despite the complex structure of many of these clusters. This provides a stepping stone to studying larger and more complex anionic systems.

ACKNOWLEDGEMENTS

I would like to take this opportunity to thank the many people who have helped me during my three years of research at Durham University and without whom this thesis would not have been possible. Firstly, I would sincerely like to thank my supervisors Professors David Tozer and Jan Verlet for their constant advice, support and encouragement, often above and beyond the call of duty. I am also very grateful to Dr. Joshua Rogers, Professor Mark Wilson and Dr. Basile Churchod for your assistance over the years with research related matters. I hope that I have been able to repay you all with good fashion advice and by keeping you abreast with current affairs.

From a personal perspective, I owe a huge debt of gratitude to my family, especially to my parents and Arnie. Thank you for being a constant source of love and support during my PhD. Special thanks must also go to the members of CG200X and CG264, past and present, who have made my time here at Durham so enjoyable. In particular Andrew, Cate and Lewis, you guys were not only nice work colleagues but true friends.

DECLARATION & STATEMENT OF COPYRIGHT

The material contained within this thesis has not previously been submitted for a degree at Durham University or any other university. The research reported within this thesis has been conducted by the author unless indicated otherwise.

LIST OF PUBLICATIONS

This thesis is based in part on the following publications:

Mensa-Bonsu, G., Tozer, D.J. and Verlet, J.R.R.
Photoelectron spectroscopic study of $I^-\cdot ICF_3$: A Frontside Attack S_N2 Pre-reaction Complex.
Phys. Chem. Chem. Phys., 2019, **21**, 13977.

Mensa-Bonsu, G., Lietard, A., & Verlet, J. R. R.
Enhancement of electron accepting ability of *para*-benzoquinone by a single water molecule.
Phys. Chem. Chem. Phys., 2019, **21**, 21689.

Mensa-Bonsu, G., Wilson, M. R., Tozer, D. J., & Verlet, J. R. R.
Photoelectron spectroscopy of *para*-benzoquinone cluster anions.
J. Chem. Phys., 2019, **151**, 204302.

Mensa-Bonsu, G., Lietard, A., Tozer, D. J., & Verlet, J. R. R.
Low energy electron impact resonances of anthracene probed by 2D photoelectron imaging of its radical anion.
J. Chem. Phys., 2020, **152**, 174303.

Other publications:

Anstöter, C.S., Mensa-Bonsu, G., Nag, P. *et al.*
Mode-specific vibrational autodetachment following excitation of electronic resonances by electrons and photons.
Phys. Rev. Lett., 2020, **124**, 203401.

LIST OF ABBREVIATIONS

ADE	Adiabatic detachment energy
CAP	Complex absorbing potential
CGTO	Contracted Gaussian-type orbital
CMOS	Complementary metal oxide semiconductor
DCS	Discretised continuum state
DD	Direct detachment
DFT	Density functional theory
DIB	Diffuse interstellar band
EA	Electron affinity
eBE	Electron binding energy
EELS	Electron energy-loss spectroscopy
eKE	Electron kinetic energy
FWHM	Full-width half-maximum
GGA	Generalised gradient approximation
GTO	Gaussian-type orbital
HF	Hartree-Fock
HOMO	Highest occupied molecular orbital
IC	Internal conversion
ID	Indirect detachment
ISM	Interstellar medium
IVR	Internal vibrational redistribution
KS	Kohn-Sham

LDA	Local density approximation
LUMO	Lowest unoccupied molecular orbital
MCP	Microchannel plate
MM	Molecular mechanics
MO	Molecular orbital
OPO	Optical parametric oscillator
PAH	Polycyclic aromatic hydrocarbon
pBQ	*para*-Benzoquinone
PE	Photoelectron
PES	Potential energy surface
PMT	Photomultiplier tube
POP	Polar onion peeling
pTQ	*para*-Toluquinone
QM	Quantum mechanical
RESP	Restrained electrostatic potential
SEVI	Slow photoelectron velocity-map imaging
S_N1	Unimolecular nucleophilic substitution
S_N2	Bimolecular nucleophilic substitution
SOMO	Singly occupied molecular orbital
STO	Slater-type orbital
TDDFT	Time-dependent density-functional theory
TE	Thermionic emission
TOF	Time-of-flight
VDE	Vertical detachment energy

VMI   Velocity map imaging

VR   Vibrational relaxation

ZPVE   Zero-point vibrational energy

CONTENTS

CHAPTER 1

INTRODUCTION

From semiconducting solar cells to anti-cancer drug delivery, the chemical processes involving negatively charged molecular ions span a wide range of research areas within the physical and biological sciences. The focus of this thesis is the study of anions that are of relevance to differing fields, some of which are outlined in Section 1.1. Metastable excited states of isolated anions and their gas phase experimental probes are then considered.

1.1 ANIONS IN NATURE

1.1.1 SIMPLE CHEMICAL REACTIONS

Organic and inorganic chemistry are littered with examples of reactions in which anions are employed, representing some of the most basic yet fundamental processes within chemistry, that often act as vital steps in the biological synthesis and industrial preparation of many compounds.[1] Anions also lie at the heart of concepts such as basicity and pH.[2] Therefore, even when considering processes involving neutral systems, anions may also feature indirectly as part of the chemical environment in which the process takes place.

Owing to its excess negative charge and thus enhanced electron density, anions often feature as nucleophiles, able to donate an electron pair for the purpose of covalent bonding.[3] It has been well documented in studies probing the ability of nucleophiles to react with the positively charged electrophilic core, *i.e.* the nucleophilicity, that an increased rate of reaction is achieved through the use of an anionic nucleophile in place of its neutral counterpart.[4] Hence, the discovery of novel anionic nucleophiles remains a vibrant area of research within chemistry.

Nucleophiles are able to partake in addition reactions, in which the electron rich species is added across a π bond, resulting in the formation of additional σ bonds.[3] This mechanism is of additional significance as it forms the initial step of anion polymerisation techniques.[5] Nucleophiles can also participate in substitution reactions, where the electron-donating nucleophile reacts with a positively-charged electrophile to replace a leaving group. In these reactions it is possible for anions to possess dual roles, as either the attacking or leaving species. Nucleophilic substitution reactions proceed predominately via either an S_N1 or S_N2 mechanism which are depicted in Figures 1.1 and 1.2. S_N1 reactions are characterised by the initial departure of the leaving group, X, which is prompted by the cleavage of the C–X bond. This results in the formation a planar carbocation intermediate bearing a formal charge of +1. As the leaving group is no longer in the immediate vicinity, the nucleophile, Nu, is then free to attack the electrophilic intermediate from either side, giving rise to a racemic mixture of enantiomeric products. In contrast to this two-step process, the S_N2 mechanism is concerted and does not involve any intermediates. Typically, C–Nu bond formation and C–X cleavage occur simultaneously through a transition state, leading to the formation of an inverted product (Figure 1.2b).[3]
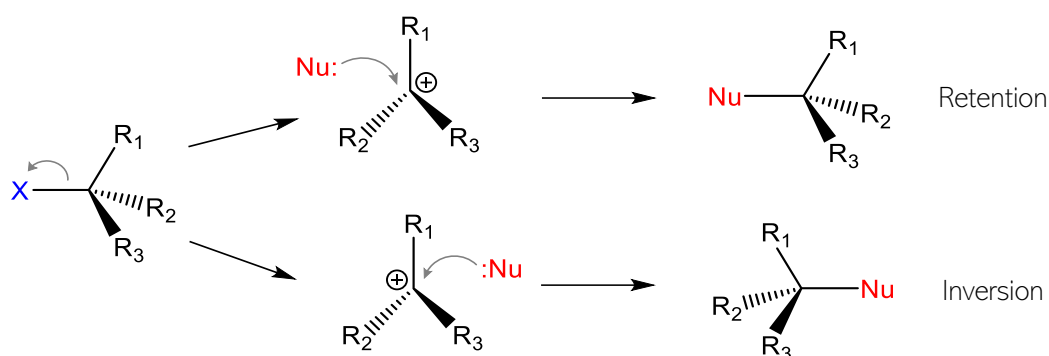
Figure 1.1: The mechanism of an S$_N$1 reaction, in which the nucleophile and leaving group are denoted as Nu and X, respectively. Substitution results in a racemic mixture of different stereoisomers.
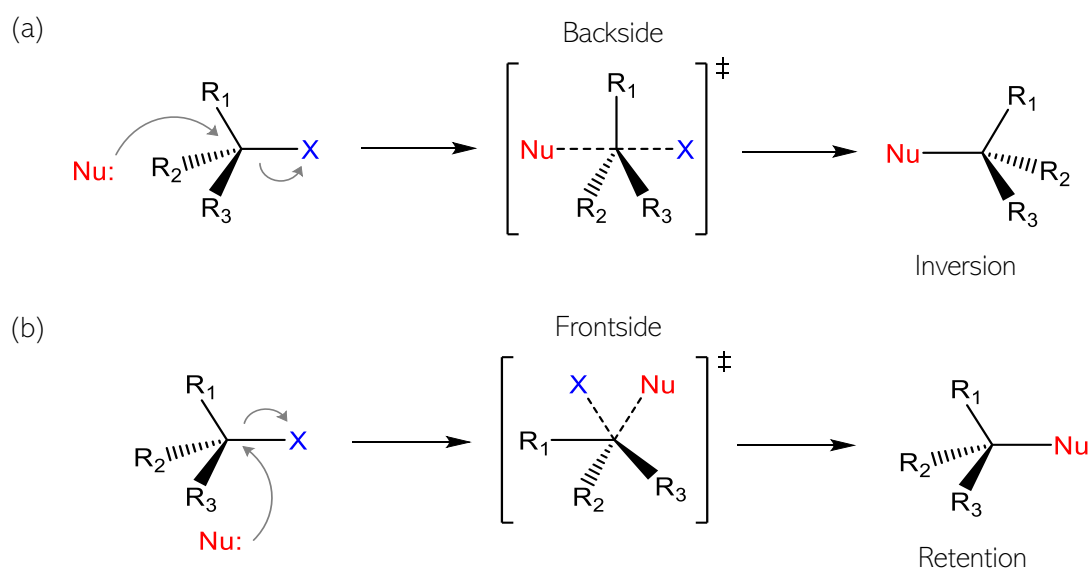
Figure 1.2: S$_N$2 reactions depicting **(a)** backside and **(b)** frontside nucleophilic attack mechanisms in which the nucleophile and leaving group are denoted as Nu and X, respectively.

Due to the steric hinderance caused by the departing leaving group, nucleophilic attack in an S$_N$2 reaction often occurs via the backside, *i.e.* at 180° degrees to the leaving group, as depicted in Figure 1.2a.[3] However, other mechanisms of S$_N$2 nucleophilic attack are possible, such as a frontside attack where the nucleophilic attack and the departure of the leaving group occur on the same side of the electrophile (see Figure 1.2b). S$_N$2 reactions that proceed via a frontside attack mechanism result in the retention of the initial configuration at the electrophilic carbon atom.[6,7] The mechanistic differences between S$_N$1 and S$_N$2 reactions are reflected in

3

their respective rate laws. S_N1 reactions are unimolecular and involve only the leaving group in its rate determining step. Conversely, the rate of S_N2 reactions is bimolecular and depends on both the leaving group and the nucleophile.[3]

Many of the nucleophilic reactions discussed here have been studied as isolated species, devoid from complex interactions with the environment, through the application of spectroscopic methods, which provides exquisite insight into the basic physical chemistry underpinning such reactions.[8–14] As an example, McAnoy *et al.* used mass spectrometry to characterise the gas-phase reaction mechanism of neutral dimethyl methylphosphonate (DMMP), $CH_3PO(OCH_3)_2$, with the hydroperoxide anion, OOH^-. In this reaction, the peroxide species is thought to act as a decontaminant, degrading DMMP, a chemical warfare agent stimulant. The $[CH_3PO(OCH_3)O]^-$ product ion observed in the resulting mass spectrum is indicative of an S_N2 pathway which leads to the demethylation of DMMP, while deprotonation of DMMP yields the other major product ion $[CH_2PO(OCH_3)_2]^-$. Comparison of measured branching ratios revealed a significantly faster rate of reaction for the S_N2 pathway.[15]

1.1.2 BIOLOGICAL SYSTEMS

Anions also play an important role in the function of various biological systems. This is particularly true of inorganic anions as they are involved in vital processes such as metabolic reactions, muscular contraction and photosynthesis. A key example is phosphate, which has the empirical formula PO_4^{3-} but is commonly found in nature in the form of its conjugate acid, hydrogen phosphate, which can exist in many different charge states due to its polyprotic nature. For example, at physiological pH inorganic phosphate is most commonly found in its $[HPO_4]^{2-}$ and $[H_2PO_4]^-$ forms.[16,17] Arguably, the most easily identifiable role of phosphate is within the structure of DNA, where alternating phosphate anions linked to sugar residues via phosphodiester bonds form the backbone of the double helix.[16,18]

Phosphate is also a key component in many molecules that are involved in metabolic and photosynthetic reactions.[18,19] For example, adenosine triphosphate (ATP) is a molecule which acts as an energy source for most cellular processes in plants and biological organisms and thus, is intimately connected to respiration and photosynthesis in which ATP is used up but also generated.[16,18] ATP exists in a –4 charge state at physiological pH due to its three phosphate groups.[20] However, this charge is readily altered during energy transfer when ATP undergoes cleavage of its high-energy phosphoric anhydride bonds (dephosphorylation) and

interconverts to a di- or ultimately, mono-phosphate ion, forming the oxidised adenosine phosphate alongside hydrogen phosphate, HPO_4^{2-}. Conversely, the production of ATP via the addition of a phosphate group to adenosine diphosphate permits the storage of potential energy in the phosphoric bonds. In respiration, ATP is generated by the glycolysis and oxidative phosphorylation pathways. In photosynthesis, ATP production is light mediated and occurs in photosystem II via photophosphorylation.[16,18]

While the biological systems involve many large and intricate complexes to achieve function, specific steps and reactions can be identified and studied. Although the gas phase is not relevant to biology, the study of gaseous (an)ions does provide access to the intrinsic properties of the biologically active anions that can inform about possible activity. For example, using gas-phase spectroscopy, it can be shown that guanine has the lowest ionisation potential.[21] Several DNA related molecules,[22–29] including ATP,[30–32] have been studied in the gas phase with a particular focus aimed at understanding how the environment changes the spectroscopic properties of anions.

These studies have been extended to a variety of anions with wider biological applications, including those that are exploited for commercial use. Recent investigations by Dessent and co-workers have analysed the effectiveness of commonly used sunscreen molecules through the determination of their photodegradation pathways.[33,34] Gas-phase UV laser dissociation studies of oxybenzone in its deprotonated and protonated forms effectively act as a probe into the performance of the molecule in different pH environments and reveal significant differences between the UVA–UVC absorption profiles of the deprotonated and protonated species, with absorption by the anion observed across a wider range of wavelengths in the UVA region. Contrastingly, reduced photodepletion intensities were recorded for the anion within the UVB region. Similar trends were observed in solution phase with basic conditions, suggesting that these results may be replicated with sunscreens during practical use. The authors identify the main photodissociation pathway of the anion as one involving significant electron loss and the production of free radicals, raising questions as to its use in the solution phase.[33]

1.1.3 INTERSTELLAR MEDIUM

One of the earliest studies exploring the possibility of molecular anions in the interstellar medium (ISM) was conducted in 1973 by Dalgarno and McCray, who theorised

possible formation mechanisms of neutral species within molecular clouds using simple anions such CH_2^- and CN^-.[35] This area of the ISM is of significance as star formation is known to occur in dense regions of interstellar clouds, where gaseous material, mainly molecular hydrogen, is vital for formation.[36] As such, understanding reaction processes which may produce or deplete the gaseous neutral molecules is critical.

Over thirty years later, the hypotheses of Dalgarno and McCray were advanced by McCarthy et $al.$,[37] who were the first to detect an interstellar molecular anion. The discovery of C_6H^- in the interstellar cloud TMC-1 was followed in relatively quick succession by that of C_4H^-, C_8H^-, C_3N^- and CN^-.[38–41] The seemingly rich anion chemistry present within molecular clouds has led to a research focus on further anion detection and quantification of their abundances. However, since the flurry of discoveries of these few anions, there have been no additional anions found. Nevertheless the discovery of simple interstellar anions has led to speculation that larger anions are present within or reacting with cosmic dust grains.[42] The so-called gas-grain interactions are of great importance as dust grains are thought to act as formation sites, on which significant processes such as H_2 formation are believed to take place.[43,44] Various models have implicated polycyclic aromatic hydrocarbons (PAHs) in such processes. These molecules act as an ideal formation site as they account for two thirds of the interstellar dust grain surface and are comprised of numerous H atoms, to which a second hydrogen can bond. In addition to formation reactions, interstellar anions such as PAHs engage in various regulatory processes including the photoelectric heating of molecular gas and the regulation of ion-molecule dynamics in the ISM, which is achieved through their engagement in charge exchanges with cations.[43]

Although interstellar PAHs are yet to be detected,[45] they are thought to be highly abundant in the ISM, responsible for up to 20% of carbon in interstellar clouds. The high polarisability of the PAH π electron cloud allows it to participate efficiently in electron attachment processes, leading to the likely formation of a PAH anion.[43] A significant number of potential PAH anions in the ISM were characterised in a theoretical study by Omont, which concluded that were it not for the accretion of PAHs on to dust grains, PAH anions would account for the majority of negative charge in diffuse clouds.[46]

Further credence has been given to the possibility of interstellar PAH anions by virtue of the diffuse interstellar band (DIB) problem. Upon inspection, a commonly shared feature emerges from the absorption spectra of almost all astronomical objects: a series of spectral

bands in the visible to near-IR region. These spectral lines have relatively broad edges and are therefore referred to as DIBs. Since their discovery in the early 1900s, many have speculated about the absorbing species or "carrier" responsible for DIBs.[46–51] A number of key observations have shed light on the characteristics of the carrier.[51–53] Amongst them was the observed lack of commonality between the bands, in terms of their profiles and energies, which suggests that DIBs do not originate from one common carrier, but many different absorbers.[54,55] Despite these revelations, the majority of DIB carriers remain unidentified causing McCall *et al.* to describe the dilemma as the "longest standing unsolved problem in spectroscopy".[54]

Buoyed by the recent confirmation of the closely related ion C_{60}^+ as a DIB carrier,[56] PAH anions have been suggested as possible candidates. Analysis carried out by Duley and Kuzmin suggests that the low-energy vibrational progressions present in the DIB spectra of several stars arise due to the torsional motions of carbonaceous, ring-based, floppy molecules such as PAHs.[57] Evidence supporting the anionic nature of the carrier can be found in the absorption spectra of several PAHs anions which display features that lie within the same spectral range as DIBs.[58] Besides PAHs, other carbon-based anions such as CH_2CN^- have been suggested as carriers.[59,60] However, the confirmation of cyano-derivatives and other molecular anions as DIB carriers relies on further characterisation of their electronic and rovibrational spectral properties.[60]

In conjunction with electronic structure calculations,[61–65] gas-phase spectroscopy is frequently employed to investigate the photophysical properties of interstellar anions.[66–70] As most species in the ISM exist in the gas phase, the relevance of this experimental method to interstellar chemistry is perhaps more transparent. Recent examples of its use include a study by Chacko *et al.* in which the temporary anion (resonance) states of FeO^- (accessed by collision excitation) were investigated to better understand the depletion pathways of interstellar FeO. The authors identify and characterise two resonance states at *ca.* 3.3 eV from which prompt dissociative decay occurs, forming mostly Fe^-. Noting the feasibility of dissociative electron attachment in interstellar conditions and agreement with literature regarding the interstellar abundance of Fe^-, the authors make the case for implementation of dissociative electron attachment pathways via resonances in astrochemical models of FeO depletion in the molecular cloud Sagittarius B2.[70]

1.2   ISOLATED ANIONS

Isolated anions are characterised by low electron detachment energies. That is to say, typically electron affinities (EA) of neutral molecules are < 5 eV, unlike their ionisation energies which typically require > 7 eV. A consequence of the low detachment energy of a typical molecular anion, X^-, is that many (if not all) of its excited states lie energetically above the detachment energy, rendering them metastable with respect to electron loss.[71–73] These electronic states are referred to as temporary anion states or resonances. Resonances are able to spontaneously undergo an electron loss process termed autodetachment, which simultaneously leads to the ejection of an electron into the detachment continuum of the neutral and the reformation of the neutral molecule.[72,74,75] Consequently, the lifetimes of resonances are typically short and occur on a femtosecond to picosecond timescale, dependent on the character of the resonance.[74]
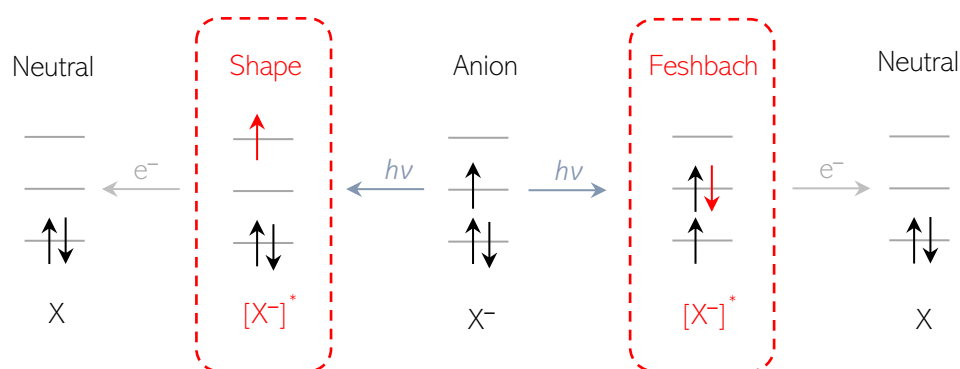
Figure 1.3: The electronic configurations of shape and Feshbach anion resonances, where red arrows represent the excited electron (with reference to the anion ground state).

Resonances can be characterised according to their electronic structure and generally fall into one of two categories: shape or Feshbach resonances. Shape resonances correspond to those for which the excess electron that is autodetached resides in an unfilled orbital of the ground-state electronic configuration of the neutral molecule (Figure 1.3). Electron emission from a shape resonance is restricted by a potential barrier present at short range. The barrier arises from the non-zero angular momentum component of the molecular orbital (MO). As shown in Figure 1.4, when the angular momentum quantum number, l, is greater than zero, an imbalance between the attractive potential and repulsive centrifugal potential results in the creation of a centrifugal barrier. The centrifugal potential scales as l^2/r^2. In practice, a shape resonance will form if an electron with a non-zero value of l collides with a molecule. To escape

confinement in the potential well, an electron must tunnel through this centrifugal barrier and escape into the continuum and therefore has a finite lifetime, typically on the order of 10s of fs.[72,75–77]
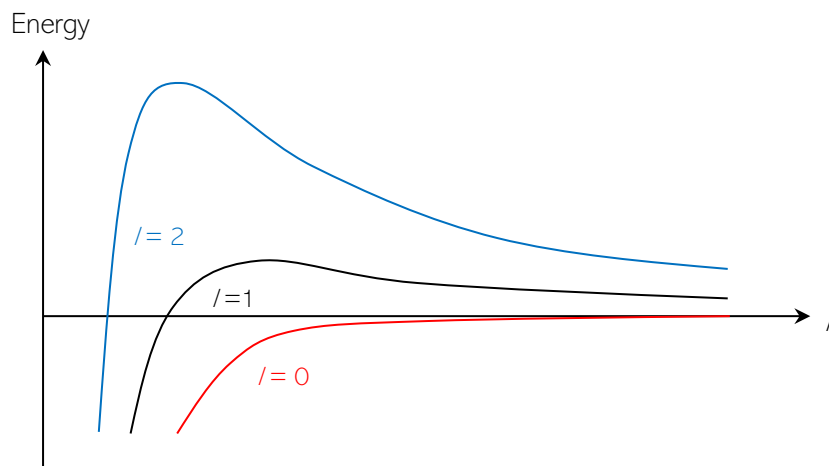
Figure 1.4: Effective potentials experienced by electrons residing in orbitals with varying angular momenta, l, shown here as a function of the electron-nuclear distance, r. In this schematic barrier heights are not to scale.

As shown in Figure 1.3, Feshbach resonances have an electronic configuration such that a one electron loss from the anion leads to an excited state electronic configuration of the neutral.[75] This does not mean that the ground state of the neutral cannot be formed upon autodetachment but that to do so necessitates electron rearrangement. Consequently, Feshbach resonances exhibit considerably longer lifetimes than shape resonances, typically on the order of 100s of fs to a few ps.[73,74,77]

1.3   DECAY PATHWAYS

The autodetachment process leading to the ground state of the neutral molecule is a decay channel available to all resonances. However, for longer-lived resonances a number of alternative pathways by which energy can be redistributed are possible and may compete with autodetachment if they occur on similar or faster timescales.[74]

Internal conversion (IC) is one such example. IC is a radiationless de-excitation process, in which the molecule undergoes a transition between two electronic states of the same spin multiplicity as shown in Figure 1.5. Adhering to the conservation of energy principle,

systems that have undergone IC and have lost electronic energy must gain energy in the lower-lying electronic state, which it does in the form of vibrational excitation leading to a vibrationally hot final state. While the initial vibrational excitation can be into specific vibrational modes of the molecule, with time, this excess energy can be redistributed between the internal vibrational degrees of freedom of the isolated system (*i.e.* internal vibrational redistribution or IVR). Note that IVR is not included in Figure 1.5 as Jablonski diagrams are typically drawn for condensed phase molecules where intramolecular vibrational relaxation (labelled VR in Figure 1.5) leads to energy transfer to the surroundings via molecular collisions. IC can proceed on an ultrafast timescale. Specifically, IC through conical intersections that lie along the initial trajectory of nuclear motion on an excited state can lead to IC on the timescale of 10s of fs. For resonances, IC is therefore able to compete directly with autodetachment and represents an efficient formation pathway for a ground state anion.[78]

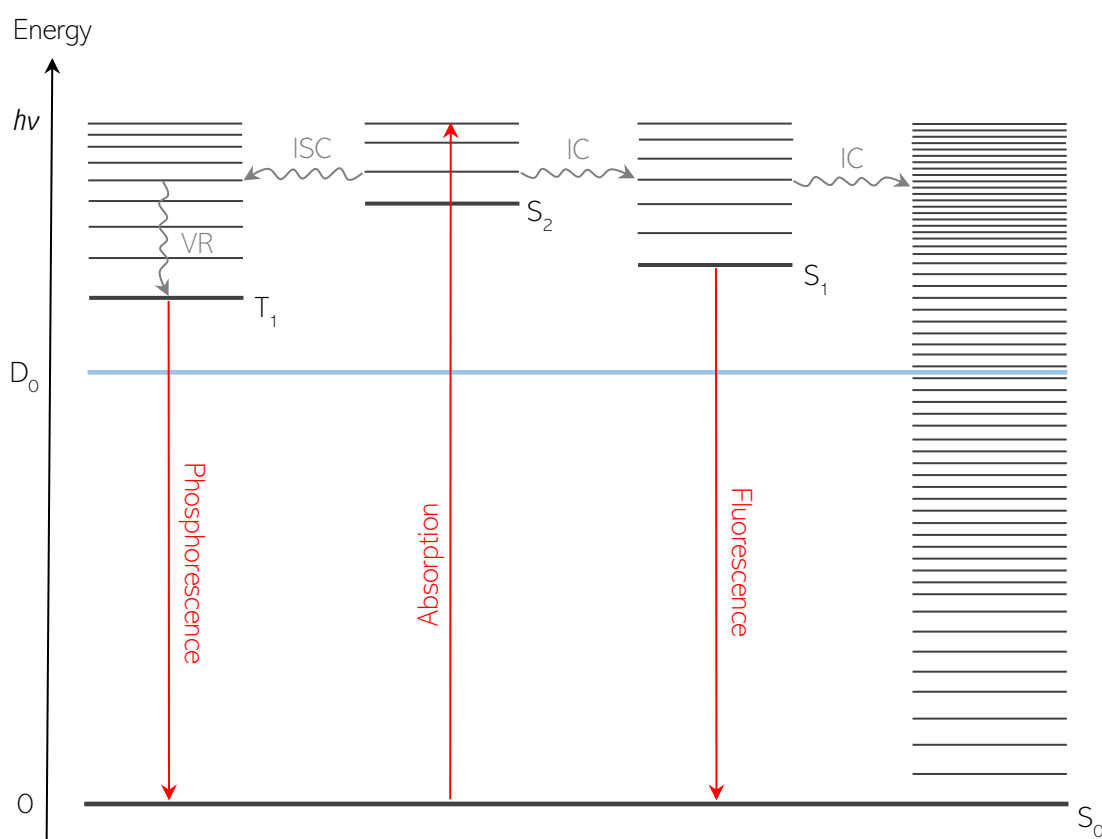**Figure 1.5:** Jablonski diagram depicting a number of radiative and non-radiative decay pathways available following excitation from the ground state of the anion (S_0), where ISC and VR denote intersystem crossing and vibrational relaxation, respectively. Internal conversion (IC) provides a pathway back to S_0, from which the neutral ground state (D_0) can be accessed through thermionic emission.

Another possible decay channel for resonances is dissociation, where the anion is the pivotal intermediate in the dissociative electron attachment process,

$$AB + e^- \rightarrow [AB^-]^* \rightarrow A + B^-.$$

In this, resonances facilitate the capture of an electron by the formation of fragmented ground state products where one of the products is a stable anion. Following excitation to a resonance state, it is possible for dissociation to occur in two ways: (i) directly on the excited state, if the resonance formed is of a repulsive nature or (ii) indirectly via a series of IC processes resulting in the vibrationally hot anion ground state, which is then followed by unimolecular dissociation on the ground electronic state.[79]

Resonances can decay to the ground state of the corresponding anion through IC that outcompetes autodetachment. In such a case, the internal (vibrational) energy of the anion must be above the electron detachment energy because the initial resonance was unbound (conservation of energy). Hence, even in the ground electronic state, the anion is subject to electron loss. However, in this case the autodetachment process is very different now and is statistical in nature. IVR has redistributed energy through all the vibrational modes and there is a possibility that the energy of these modes lies above the electron detachment energy, resulting in electron emission. The statistical (Boltzmann) sampling of these modes leads to the emission of low-energy electrons that occurs on a μs to ms timescale and this emission is often coined thermionic emission. Note that thermionic emission is in competition with unimolecular dissociation described above and the dominant process is often determined by the relative barriers – the electron affinity for thermionic emission and the bond energy for unimolecular dissociation.

1.4   PROBES OF RESONANCES

Arguably the most powerful method used in the study of anion resonances is 2D electron energy-loss spectroscopy (EELS). In this method, a beam of electrons with defined kinetic energy impact onto a gaseous sample of neutral molecules. Interaction of the electrons with the sample may result in the inelastic scattering of the electrons, *i.e.* energy exchange and deflection from their initial path (as predetermined by the incident angle).[80] 2D EELS measures changes in the kinetic energy of the outgoing electrons (eKE) as a function of the incident electron energy (E_i), providing information as to the respective final and initial vibrational

states accessed by the incident electron.[81,82] 2D EELS was developed by Allan in the 2000s following two initial 2D EELS experiments and has been used exclusively by his group to characterise anion resonances in the gas phase.[82–84]

One such molecule to which this method has been applied is acrylonitrile (CH_2CHCN), for which the resulting 2D EELS spectrum has been reproduced in Figure 1.6.[85] The spectrum, measured between $E_i = 0.095 – 0.9$ eV with a scattering angle of 135°, contains a number of typical features which will briefly be discussed. Beginning with analysis of the low energy region of the spectrum, a vertical feature is observed at $\Delta E = 0$ (where ΔE is the electron energy loss) which is representative of the elastic processes occurring at each value of E_i and is referred to as the elastic ridge. At a particular incident energy, the maximum value of ΔE is equal to that of E_i and corresponds to an outgoing electron with eKE ~ 0. This scenario gives rise to diagonal features that occur along the threshold line. Information regarding resonance dynamics can be inferred through patterns within the spectrum. Horizontally arranged spectral peaks indicate the energy of the resonance which decays into various vibrational states, while peaks falling along vertical lines reveal the final vibrational state of the neutral molecule. Aside from the threshold line, other diagonal lines (labelled A, B and C) upon which several features occur can be observed in Figure 1.6. These diagonally arranged peaks are atypical in a 2D EELS spectrum and point towards selectivity of the vibrational modes deexcited during autodetachment.[81,82,85,86]
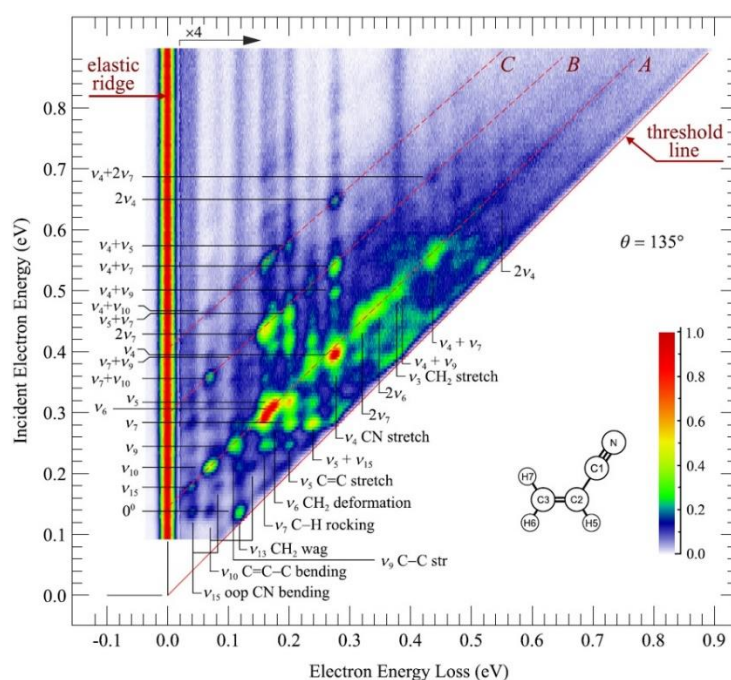

Figure 1.6: 2D electron energy loss spectrum of acrylonitrile measured at a scattering angle of 135°. This figure has been reproduced from Ref [85].

1.5   PHOTOELECTRON SPECTROSCOPY

Thus far, the formation of anion resonances has been discussed predominantly in terms of electron attachment to a neutral molecule. However, resonances can also be accessed by photoexcitation of an anion,

$$X + e^- \rightarrow [X^-]^* \leftarrow X^- + h\nu$$

representing two pathways by which to examine temporary anion states. Anion photoelectron (PE) spectroscopy utilises the detachment pathway to characterise the electronic properties and dynamics of anions. The term PE spectroscopy refers to a variety of experimental techniques in which the kinetic energy of the detached electron are dispersed and measured following photodetachment or ionisation of a species.[73] PE spectroscopic techniques vary according to the source of the ionising radiation used, which consequently determines the electronic states that are probed. X-ray PE spectroscopy employs X-rays with a photon energies up to 1.5 keV, and can be used to examine core electrons.[87] Ultraviolet PE spectroscopy uses UV photons with an energy of between 10 - 45 eV to eject valence electrons. Because electron affinities are lower than ionisation potentials, PE spectroscopy of the valence electrons of anions can be performed with lower energy photons, typically with photon energies of 3 - 6 eV.

The principles of PE spectroscopy are rooted in the photoelectric effect, where the absorption of photons with energies above a threshold causes the ejection of electrons from a material. For materials, this threshold is the work function. In the case of anion PE spectroscopy, this threshold is the electron affinity (EA) of the molecule and represents the minimum amount of energy the incident photon must possess for photodetachment of the electron to occur.[88]

The mechanism of PE spectroscopy is outlined schematically in Figure 1.7. Following the absorption of a photon by the anion and the ensuing excitation of the molecule into a virtual state, an electron will be photoejected with a defined kinetic energy that is equal to

$$\text{eKE} = h\nu - \text{EA}, \tag{1.1}$$

where both the eKE and $h\nu$ are quantities that can be determined from the experiment. The outgoing electron will be detached into the continuum of the neutral. The kinetic energies of the photodetached electrons will differ according to which vibrational level of the neutral state the molecule has relaxed into. In a PE spectrum, this difference will be evident as a series of narrow bands known as a vibrational progression.[72,74] In line with the Born-Oppenheimer

approximation, which assumes that electrons move much faster than nuclei due to the considerable difference in their respective masses, the photodetachment process is considered instantaneous with respect to nuclear motion. As such, the relative intensities of the vibrational progression are governed solely by the overlap of the vibrational wavefunctions of the initial, $\Psi_{v'}^{i}$, and final states, $\Psi_{v''}^{f}$, *i.e.* the Franck-Condon overlap, which is given as[89]

$$\langle \Psi_{v'}^{i} | \Psi_{v''}^{f} \rangle. \tag{1.2}$$

In the case of PE spectroscopy, the initial and final states would correspond to the lowest vibrational level of the anion and the particular vibrational level of the neutral accessed following electron photodetachment, respectively.

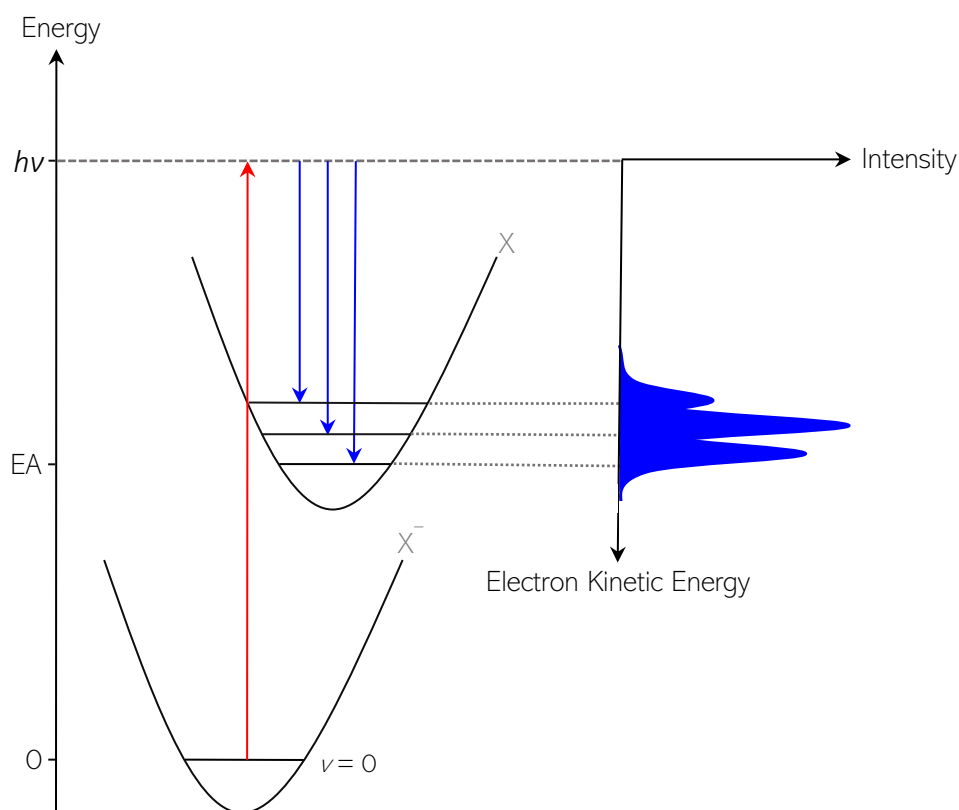**Figure 1.7:** Pictorial representation of photoelectron spectroscopy in which the absorption of a photon is followed by ejection of an electron into the neutral continuum and the reformation of the neutral.

PE spectra can be either plotted as a function of eKE or, perhaps more intuitively, as a function of the electron binding energy, eBE = $h\nu$ – eKE. When the initial and final states are

the ground electronic states of the anion and neutral in their $v = 0$ level, the eBE = EA. But more generally, eBE represents a measure of how strongly electrons are bound to the anion.

1.6   2D ANION PHOTOELECTRON SPECTROSCOPY

Through the measurement of PE spectra, one can gain vibrational and energetic information regarding the anion and neutral states. However, as outlined earlier, anions also have excited states and most of these lie in the continuum that is accessed in PE spectroscopy. Therefore, the photon energy used may excite a resonance and the dynamics and autodetachment from these will be imprinted on the resulting PE spectrum. Although it is possible to identify resonances from a PE spectrum obtained at a single wavelength, a more comprehensive picture of resonance character and dynamics is likely to be gained by viewing changes in the eKE distribution over a range of hv. This method is known as frequency resolved (or 2D) PE spectroscopy.[74]

2D PE spectra are often presented as a false-colour map similar to 2D EELS (see Figure 1.6). Figure 1.8 shows a cartoon of such a 2D PE spectrum. Decay mechanisms and resonance dynamics can be ascertained from characteristic patterns in eKE distributions. Decay dynamics can generally be partitioned into direct and indirect processes. Direct detachment (DD) processes occur when the absorption of a photon simply leads to the instantaneous detachment of an electron from the anion and do not involve excitation to an intermediary electronic state. DD processes must – by conservation of energy – result in an increase in the measured eKE with increasing photon energy and therefore, are represented by diagonal features, such as that shown in Figure 1.8. Indirect processes are those in which resonance-mediated dynamics occur and include resonance autodetachment and thermionic emission. These processes are typically indicated by off-diagonal features, red shifted in kinetic energy with respect to the diagonal DD features.[73,74]
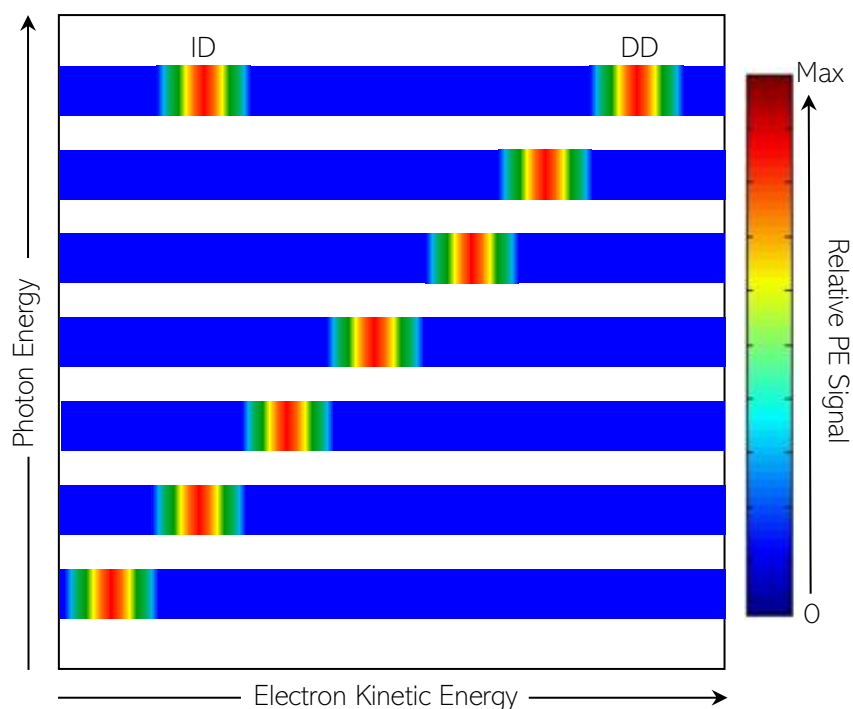
Figure 1.8: Exemplar 2D photoelectron spectrum in which direct detachment (DD) processes are represented by diagonal features that occur at energies above the electron affinity of the molecule. Red-shifted, off-diagonal features correspond to indirect detachment (ID) pathways.

1.7 VELOCITY MAP IMAGING

Traditional PE spectroscopy experiments are often modified by the use of an alternative measurement technique of the eKE.[90] One such modification is the inclusion of velocity map imaging (VMI) in experiments. VMI differs to the traditional PE spectroscopy detection instrument as the kinetic energy of the electrons are determined from the velocity distribution of the photofragments, instead of time-of-flight measurements.[91]

The main advantages of VMI over more traditional time-of-flight spectrometers is a higher detection efficiency and the ability to measure photoelectron angular distributions.[92,93] VMI uses an electrostatic lens which focuses the photodetached electrons to a single spot on the detector based on the electrons' velocities but irrespective of the electrons' initial positions.[91,94] VMI therefore yields relatively high resolution with near unit collection efficiency and, because it is not based on time-of-flight, is equally sensitive to very low energy electrons.

A core benefit of VMI is the ease with which angular distribution information can be collected.[93] The angular distribution of the photoelectrons is of importance as it provides

information as to the shape of the orbital from which the electron was ejected. It is possible to measure the angular distribution of electrons with respect to the polarisation of the laser beam by incorporating other spectroscopic techniques into PE spectroscopy, such as a hemispherical analyser or time-of-flight spectrometers.[74,90,92] However, the use of these spectrometers requires varying the polarisation of the laser or the angle of the spectrometer, which is not necessary in VMI.[90]

1.8   AIMS

The preceding sections illustrate the significant role anions play within in a diverse range of scientific fields and the unique insight that can be gained through the study of the species in the gas phase using experimental methods. Photoelectron spectroscopy is one such technique that is routinely exploited for this purpose. However, a vast number of studies that employ this method consider only the isolated species. When investigating the photophysical properties of the anion, it is important to also recognise the unique chemical environment within which the anion resides. Hence, it is also necessary to probe clusters of the anion. Relevant clusters to consider include micro-solvated and oligomer anion complexes, which often represent prototypical biological systems. Studying anion clusters is also of relevance to reactive organic systems as it can be representative of the pre-reaction complex or transition state formed. With this in mind, the central aim of this thesis is to apply frequency-resolved photoelectron spectroscopy to anionic clusters to probe how microhydration and oligomerisation affect the spectroscopy and decay dynamics of the anion. Additionally, this thesis aims to demonstrate how photoelectron spectroscopy can be used to characterise and control a classic organic reaction.

Another key objective of this thesis is to provide insight into the photophysical properties of clusters through the characterisation of their anion resonances. For this purpose, both experimental and computational techniques will be employed. It is hoped that a relatively simple computational methodology can be developed to identify the energetic location and nature of the resonances. While higher level electronic structure calculations could provide an increased level of accuracy, the objective here is to demonstrate how density functional theory and the basis set stabilisation method can be utilised as an inexpensive, user-friendly aid, to qualitatively inform complementary spectroscopic studies.

17

1.9 REFERENCES

(1)   DePuy, C. H.; Grabowski, J. J.; Bierbaum, V. M. Chemical Reactions of Anions in the Gas Phase. *Science* **1982**, *218* (4576), 955–960.

(2)   Baker, F. J.; Silverton, R. E. 5 - Some Fundamentals of Chemistry. In *Introduction to Medical Laboratory Technology (Fifth Edition)*; Baker, F. J., Silverton, R. E., Eds.; Butterworth-Heinemann, **1976**; pp 77–111.

(3)   Clayden, J.; Greeves, N.; Warren, S.; Wothers, P. *Organic Chemistry*; OUP Oxford: Oxford ; New York, **2001**.

(4)   Ouellette, R. J.; Rawn, J. D. Nucleophilic Substitution and Elimination Reactions. In *Organic Chemistry*; Ouellette, R. J., Rawn, J. D., Eds.; Elsevier: Boston, **2014**; pp 333–356.

(5)   Quirk, R. P. Anionic Polymerization. In *Encyclopedia of Polymer Science and Technology*; American Cancer Society, **2002**.

(6)   Xie, J.; Hase, W. L. Rethinking the S_N2 Reaction. *Science* **2016**, *352* (6281), 32–33.

(7)   Zhang, X.; Ren, J.; Tan, S. M.; Tan, D.; Lee, R.; Tan, C.-H. An Enantioconvergent Halogenophilic Nucleophilic Substitution (S_N2X) Reaction. *Science* **2019**, *363* (6425), 400–404.

(8)   Tsukuda, T.; Kondow, T. Anionic Polymerization in the Gas-Phase Cluster of 2-Chloroacrylonitrile. *J. Phys. Chem.* **1992**, *96* (14), 5671–5673.

(9)   Tsukuda, T.; Kondow, T. Intracluster Anionic Polymerization of $(CH_2=CXCN)_m$ (X = H, D, CH_3, and Cl) in Collision with High-Rydberg Rare Gas Atoms and Electrons. In *Physics and Chemistry of Finite Systems: From Clusters to Crystals*; Jena, P., Khanna, S. N., Rao, B. K., Eds.; NATO ASI Series; Springer Netherlands: Dordrecht, **1992**; pp 1147–1152.

(10)   Cyr, D. M.; Scarton, M. G.; Johnson, M. A. Photoelectron Spectroscopy of the Gas-phase S_N2 Reaction Intermediates $I^-\cdot CH_3I$ and $I^-\cdot CD_3I$: Distortion of the CH_3I at the "'Ion-Dipole'" Complex. *J. Chem. Phys.* **1993**, *99* (6), 4869–4872.

(11)   Strode, K. S.; Grimsrud, E. P. Gas Phase S_N2 Nucleophilic Displacement Reactions at Atmospheric Pressure by the Photodetachment-Modulated Electron Capture Detector. *Int. J. Mass Spectrom. Ion Process.* **1994**, *130* (3), 227–236.

(12)   Caldwell, G.; Magnera, T. F.; Kebarle, P. S_N2 Reactions in the Gas Phase. Temperature Dependence of the Rate Constants and Energies of the Transition States. Comparison with Solution. *J. Am. Chem. Soc.* **1984**, *106* (4), 959–966.

(13)   Wester, R.; Bragg, A. E.; Davis, A. V.; Neumark, D. M. Time-Resolved Study of the Symmetric S_N2-Reaction $I^- + CH_3I$. *J. Chem. Phys.* **2003**, *119* (19), 10032–10039.

(14)   Langer, J.; Matejcik, S.; Illenberger, E. The Nucleophilic Displacement (S_N2) Reaction $F^- + CH_3Cl \rightarrow CH_3F + Cl^-$ Induced by Resonant Electron Capture in Gas Phase Clusters. *Phys. Chem. Chem. Phys.* **2000**, *2* (5), 1001–1005.

(15)   McAnoy, A. M.; Paine, M. R. L.; Blanksby, S. J. Reactions of the Hydroperoxide Anion with Dimethyl Methylphosphonate in an Ion Trap Mass Spectrometer: Evidence for a Gas Phase α-Effect. *Org. Biomol. Chem.* **2008**, *6* (13), 2316–2326.

(16)   Garett, R. H.; Grisham, C. M. *Biochemistry*, 4th ed.; Brooks/Cole: Boston, **2008**.

(17)   Bianchi, A.; Bowman-James, K.; García-España, E. Aspects of Anion Coordination from Historical Perspectives. In *Anion Coordination Chemistry*; John Wiley & Sons, Ltd, **2011**; pp 1–73.

(18)   Campbell, N. A.; Reece, J. B. *Biology*, 8th ed.; Pearson: England, **2010**.

(19)   Takeda, E.; Taketani, Y.; Morita, K.; Tatsumi, S.; Katai, K.; Nii, T.; Yamamoto, H.; Miyamoto, K. Molecular Mechanisms of Mammalian Inorganic Phosphate Homeostasis. *Adv. Enzyme Regul.* **2000**, *40* (1), 285–302.

(20)   Sabirov, R. Z.; Okada, Y. ATP Release via Anion Channels. *Purinergic Signal.* **2005**, *1* (4), 311–328.

(21)   Yang, X.; Wang, X.-B.; Vorpagel, E. R.; Wang, L.-S. Direct Experimental Observation of the Low Ionization Potentials of Guanine in Free Oligonucleotides by Using Photoelectron Spectroscopy. *Proc. Natl. Acad. Sci.* **2004**, *101* (51), 17588–17592.

(22)   Wincel, H. Microhydration of Deprotonated Nucleobases. *J. Am. Soc. Mass Spectrom.* **2016**, *27* (8), 1383–1392.

(23)   Kočišek, J.; Pysanenko, A.; Fárník, M.; Fedor, J. Microhydration Prevents Fragmentation of Uracil and Thymine by Low-Energy Electrons. *J. Phys. Chem. Lett.* **2016**, *7* (17), 3401–3405.

(24)   Denifl, S.; Ptasińska, S.; Hanel, G.; Gstir, B.; Probst, M.; Scheier, P.; Märk, T. D. Electron Attachment to Gas-Phase Uracil. *J. Chem. Phys.* **2004**, *120* (14), 6557–6565.

(25)   Wang, C.-R.; Nguyen, J.; Lu, Q.-B. Bond Breaks of Nucleotides by Dissociative Electron Transfer of Nonequilibrium Prehydrated Electrons: A New Molecular Mechanism for Reductive DNA Damage. *J. Am. Chem. Soc.* **2009**, *131* (32), 11320–11322.

(26)   Huber, D.; Beikircher, M.; Denifl, S.; Zappa, F.; Matejcik, S.; Bacher, A.; Grill, V.; Märk, T. D.; Scheier, P. High Resolution Dissociative Electron Attachment to Gas Phase Adenine. *J. Chem. Phys.* **2006**, *125* (8), 084304.

(27)   Dawley, M. M.; Tanzer, K.; Carmichael, I.; Denifl, S.; Ptasińska, S. Dissociative Electron Attachment to the Gas-Phase Nucleobase Hypoxanthine. *J. Chem. Phys.* **2015**, *142* (21), 215101.

(28)   Wang, P.; Xu, H.-G.; Cao, G.-J.; Zhang, W.-J.; Xu, X.-L.; Zheng, W.-J. Nonconventional Hydrogen Bonds between Silver Anion and Nucleobases: Size-Selected Anion Photoelectron Spectroscopy and Density Functional Calculations. *J. Phys. Chem. A* **2017**, *121* (46), 8973–8981.

(29)   Nichols, C. M.; Wang, Z.-C.; Lineberger, W. C.; Bierbaum, V. M. Gas-Phase Reactions of Deprotonated Nucleobases with H, N, and O Atoms. *J. Phys. Chem. Lett.* **2019**, 4863–4867.

(30)   Schinle, F.; Crider, P. E.; Vonderach, M.; Weis, P.; Hampe, O.; Kappes, M. M. Spectroscopic and Theoretical Investigations of Adenosine 5′-Diphosphate and Adenosine 5′-Triphosphate Dianions in the Gas Phase. *Phys. Chem. Chem. Phys.* **2013**, *15* (18), 6640–6650.

(31)   Cercola, R.; Matthews, E.; Dessent, C. E. H. Photoexcitation of Adenosine 5'-Triphosphate Anions in Vacuo: Probing the Influence of Charge State on the UV Photophysics of Adenine. *J. Phys. Chem. B* **2017**, *121* (22), 5553–5561.

(32)   Asakawa, D.; Mizuno, H.; Toyo'oka, T. Gas-Phase Stability of Negatively Charged Organophosphate Metabolites Produced by Electrospray Ionization and Matrix-Assisted Laser Desorption/Ionization. *J. Am. Soc. Mass Spectrom.* **2017**, *28* (12), 2561–2568.

(33)   Wong, N. G. K.; Berenbeim, J. A.; Hawkridge, M.; Matthews, E.; Dessent, C. E. H. Mapping the Intrinsic Absorption Properties and Photodegradation Pathways of the Protonated and Deprotonated Forms of the Sunscreen Oxybenzone. *Phys. Chem. Chem. Phys.* **2019**, *21* (26), 14311–14321.

(34)   Wong, N. G. K.; Berenbeim, J. A.; Dessent, C. E. H. Direct Observation of Photochemical Free Radical Production from the Sunscreen 2-Phenylbenzimidazole-5-Sulfonic Acid via Laser-Interfaced Mass Spectrometry. *ChemPhotoChem* **2019**, *3* (12), 1231–1237.

(35)   Dalgarno, A.; McCray, R. A. The Formation of Interstellar Molecules from Negative Ions. *Astrophys. J.* **1973**, *181*, 95–100.

(36)   Shull, J. M.; Beckwith, S. Interstellar Molecular Hydrogen. *Ann. Rev. Astron. Astrophys.* **1982**, *20*, 163–190.

(37) McCarthy, M. C.; Gottlieb, C. A.; Gupta, H.; Thaddeus, P. Laboratory and Astronomical Identification of the Negative Molecular Ion C_6H^-. *Astrophys. J. Lett.* **2006**, *652* (2), L141.

(38) Cernicharo, J.; Guélin, M.; Agúndez, M.; Kawaguchi, K.; McCarthy, M.; Thaddeus, P. Astronomical Detection of C_4H^-, the Second Interstellar Anion. *Astron. Astrophys.* **2007**, *467*, L37–L40.

(39) Brünken, S.; Gupta, H.; Gottlieb, C. A.; McCarthy, M. C.; Thaddeus, P. Detection of the Carbon Chain Negative Ion C_8H^- in TMC-1. *Astrophys. J. Lett.* **2007**, *664* (1), L43.

(40) Thaddeus, P.; Gottlieb, C. A.; Gupta, H.; Brünken, S.; McCarthy, M. C.; Agúndez, M.; Guélin, M.; Cernicharo, J. Laboratory and Astronomical Detection of the Negative Molecular Ion C_3N^-. *Astrophys. J.* **2008**, *677* (2), 1132.

(41) Agundez, M.; Cernicharo, J.; Guelin, M.; Kahane, C.; Roueff, E.; Klos, J.; Aoiz, F. J.; Lique, F.; Marcelino, N.; Goicoechea, J. R.; Garcia, M. G.; Gottlieb, C. A.; McCarthy, M. C.; Thaddeus, P. Astronomical Identification of CN^-, the Smallest Observed Molecular Anion. *Astron.Astrophys.* **2010**, *517*, L2.

(42) Cordiner, M. A.; Charnley, S. B. Gas-Grain Models For Instellar Anion Chemistry. *Astrophys. J.* **2012**, *749* (2), 120.

(43) Verstraete, L. The Role of PAHs in the Physics of the Interstellar Medium. *EAS PublSer* **2011**, *46*, 415–426.

(44) Gry, C.; Boulanger, F.; Nehmé, C.; Habart, E.; Falgarone, E. H_2 Formation and Excitation in the Diffuse Interstellar Medium. *Astron. Astrophys.* **2002**, *391* (2), 675–680.

(45) Gudipati, M. S.; Yang, R. In-Situ Probing of Radiation-Induced Processing of Organics in Astrophysical Ice Analogs - Novel Laser Desorption Laser Ionization Time-of-Flight Mass Spectroscopic Studies. *Astrophys. J.* **2012**, *756* (1), L24.

(46) Omont, A. Physics and Chemistry of Interstellar Polycyclic Aromatic Molecules. In *Polycyclic Aromatic Hydrocarbons and Astrophysics*; Léger, A., d'Hendecourt, L., Boccara, N., Eds.; NATO ASI Series; Springer Netherlands: Dordrecht, **1987**; pp 371–372.

(47) Salama, F.; Bakes, E. L. O.; Allamandola, L. J.; Tielens, A. G. G. M. Assessment of the Polycyclic Aromatic Hydrocarbon-Diffuse Interstellar Band Proposal. *Astrophys. J.* **1996**, *458* (2 PART I), 621–636.

(48) Geballe, T. R. The Diffuse Interstellar Bands - a Brief Review. *J. Phys. Conf. Ser.* **2016**, *728*, 062005.

(49) van der Zwet, G. P.; Allamandola, L. J. Polycyclic Aromatic Hydrocarbons and the Diffuse Interstellar Bands. In *Light on Dark Matter*; Israel, F. P., Ed.; Astrophysics and Space Science Library; Springer Netherlands, **1986**; pp 233–236.

(50) Steglich, M.; Bouwman, J.; Huisken, F.; Henning, T. Can Neutral and Ionized Polycyclic Aromatic Hydrocarbons Be Carriers of the Ultraviolet Extinction Bump and the Diffuse Interstellar Bands? *Astrophys. J.* **2011**, *742* (1), 2.

(51) Snow, T. P.; Le Page, V.; Keheyan, Y.; Bierbaum, V. M. The Interstellar Chemistry of PAH Cations. *Nature* **1998**, *391* (6664), 259–260.

(52) McCall, B. J.; Griffin, R. E. On the Discovery of the Diffuse Interstellar Bands. *Proc. R. Soc. Lond. Math. Phys. Eng. Sci.* **2013**, *469* (2151).

(53) Snow, T. P. The Unidentified Diffuse Interstellar Bands as Evidence for Large Organic Molecules in the Interstellar Medium. *Spectrochim. Acta Part -Mol. Biomol. Spectrosc.* **2001**, *57* (4), 615–626.

(54) McCall, B. J.; Drosback, M. M.; Thorburn, J. A.; York, D. G.; Friedman, S. D.; Hobbs, L. M.; Rachford, B. L.; Snow, T. P.; Sonnentrucker, P.; Welty, D. E. Studies of the Diffuse Interstellar Bands. IV. The Nearly Perfect Correlation between λλ6196.0 and 6613.6. *Astrophys. J.* **2010**, *708* (2), 1628–1638.

(55) Moutou, C.; Krelowski, J.; d'Hendecourt, L.; Jamroszczak, J. On Correlations between Diffuse Interstellar Bands. *ArXivastro-Ph9912560* **1999**.

(56) Campbell, E. K.; Holz, M.; Gerlich, D.; Maier, J. P. Laboratory Confirmation of C_{60}^+ as the Carrier of Two Diffuse Interstellar Bands. *Nature* **2015**, *523* (7560), 322–323.

(57) Duley, W. W.; Kuzmin, S. Vibronic Progressions in Several Diffuse Interstellar Bands. *Astrophys. J.* **2010**, *712* (2), L165–L168.

(58) Cox, N. L. J. The PAH-DIB Hypothesis. *EAS Publ. Ser.* **2011**, *46*, 349–354.

(59) Cordiner, M. A.; Sarre, P. J. The CH_2CN^- Molecule: Carrier of the λ8037 Diffuse Interstellar Band? *Astron. Astrophys.* **2007**, *472* (2), 537–545.

(60) Fortenberry, R. C.; Crawford, T. D.; Lee, T. J. The Possible Interstellar Anion CH_2CN^-: Spectroscopic Constants, Vibrational Frequencies, and Other Considerations. *Astrophys. J.* **2013**, *762* (2), 121.

(61) Yang, Z.; Snow, T. P.; Bierbaum, V. M. Computational Studies of Gas Phase Reactions of Carbon Chain Anions with N and O Atoms. *Phys. Chem. Chem. Phys.* **2010**, *12* (40), 13091–13098.

(62) Hammoutène, D.; Hochlaf, M.; Senent, M. Structure and Electronic Spectra of the C_6^- Anion. *Mon. Not. R. Astron. Soc.* **2012**, *424*, 1224–1231.

(63) Majumdar, L.; Das, A.; Chakrabarti, S. K. Spectroscopic Characteristics of the Cyanomethyl Anion and Its Deuterated Derivatives. *Astron. Astrophys.* **2014**, *562*, A56.

(64) Fortenberry, R. C.; Lukemire, J. A. Electronic and Rovibrational Quantum Chemical Analysis of C_3P^-: The Next Interstellar Anion? *Mon. Not. R. Astron. Soc.* **2015**, *453* (3), 2824–2829.

(65) Gianturco, F. A.; Satta, M.; Yurtsever, E.; Wester, R. Formation of Anionic C, N-Bearing Chains in the Interstellar Medium via Reactions of H^- with HC_xN for Odd-Valued *x* from 1 to 7. *Astrophys. J.* **2017**, *850* (1), 42.

(66) Lakin, N. M.; Güthe, F.; Tulej, M.; Pachkov, M.; Maier, J. P. Spectroscopy of Excited States of Carbon Anions above the Photodetachment Threshold. *Faraday Discuss.* **2000**, *115* (0), 383–393.

(67) Yen, T. A.; Garand, E.; Shreve, A. T.; Neumark, D. M. Anion Photoelectron Spectroscopy of C_3N^- and C_5N^-. *J. Phys. Chem. A* **2010**, *114* (9), 3215–3220.

(68) Aravind, G.; Nrisimhamurty, M.; Mane, R. G.; Gupta, A. K.; Krishnakumar, E. Probing Electronic States of TaC and Observation of a Stable Excited State of TaC^- by Anion-Photoelectron Spectroscopy. *Phys. Rev. A* **2015**, *92* (4), 042503.

(69) Kim, J. B.; Weichman, M. L.; Neumark, D. M. Low-Lying States of FeO and FeO^- by Slow Photoelectron Spectroscopy. *Mol. Phys.* **2015**, *113* (15–16), 2105–2114.

(70) Chacko, R.; Banhatti, S.; Mane, R. G.; Gupta, A. K.; Aravind, G. Depletion of FeO in the Interstellar Medium via Its Anion Resonances. *Astrophys. J.* **2018**, *865* (1), 66.

(71) Rienstra-Kiracofe, J. C.; Tschumper, G. S.; Schaefer, H. F.; Nandi, S.; Ellison, G. B. Atomic and Molecular Electron Affinities: Photoelectron Experiments and Theoretical Computations. *Chem. Rev.* **2002**, *102* (1), 231–282.

(72) Simons, J. Molecular Anions. *J. Phys. Chem. A* **2008**, *112* (29), 6401–6511.

(73) Henley, A.; Fielding, H. H. Anion Photoelectron Spectroscopy of Protein Chromophores. *Int. Rev. Phys. Chem.* **2019**, *38* (1), 1–34.

(74) Anstöter, C. S.; Bull, J. N.; Verlet, J. R. R. Ultrafast Dynamics of Temporary Anions Probed through the Prism of Photodetachment. *Int. Rev. Phys. Chem.* **2016**, *35* (4), 509–538.

(75) Millar, T. J.; Walsh, C.; Field, T. A. Negative Ions in Space. *Chem. Rev.* **2017**, *117* (3), 1765–1795.

(76) Dehmer, J. L. Shape Resonances in Molecular Fields. In *Resonances*; ACS Symposium Series; American Chemical Society, **1984**; Vol. 263, pp 139–163.

(77) Simons, J. Roles Played by Metastable States in Chemistry. *Acs Symp. Ser.* **1984**, *263*, 3–16.

(78) Jablonski diagram https://chem.libretexts.org/Bookshelves/Physical_and_Theoretical_Chemistry_Textbook_Maps/Supplemental_Modules_(Physical_and_Theoretical_Chemistry)/Spectroscopy/Electronic_Spectroscopy/Jablonski_diagram (accessed Nov 17, 2019).

(79) Munro, J. J.; Harrison, S.; Fujimoto, M. M.; Tennyson, J. A Dissociative Electron Attachment Cross-Section Estimator. *J. Phys. Conf. Ser.* **2012**, *388* (1), 012013.

(80) Hofer, F.; Schmidt, F. P.; Grogger, W.; Kothleitner, G. Fundamentals of Electron Energy-Loss Spectroscopy. *IOP Conf. Ser. Mater. Sci. Eng.* **2016**, *109*, 012007.

(81) Hotop, H. Michael Allan - Electron Impact Spectroscopy at Its Best*. *Eur. Phys. J. D* **2016**, *70* (10), 200.

(82) Allan, M.; Regeta, K.; Gorfinkiel, J.; Masin, Z.; Grimme, S.; Bannwarth, C. Recent Research Directions in Fribourg: Nuclear Dynamics in Resonances Revealed by 2-Dimensional EEL Spectra, Electron Collisions with Ionic Liquids and Electronic Excitation of Pyrimidine. *Eur. Phys. J. D* **2016**, *70*.

(83) Reddish, T.; Currell, F.; Comer, J. Studies of the 2 eV Shape Resonance in N_2 using a Two-Dimensional Scanning Technique. *J. Phys. [E]* **1988**, *21* (2), 203–207.

(84) Currell, F.; Comer, J. Observation of Friction in the Nuclear Dynamics of CO_2^- near the Equilibrium Geometry of the Negative Ion. *Phys. Rev. Lett.* **1995**, *74* (8), 1319–1322.

(85) Regeta, K.; Allan, M. Autodetachment Dynamics of Acrylonitrile Anion Revealed by Two-Dimensional Electron Impact Spectra. *Phys. Rev. Lett.* **2013**, *110* (20), 203201.

(86) Regeta, K.; Allan, M. Two-Dimensional Spectra of Electron Collisions with Acrylonitrile and Methacrylonitrile Reveal Nuclear Dynamics. *J. Chem. Phys.* **2015**, *142* (18), 184307.

(87) 5.3: Photoelectron Spectroscopy https://chem.libretexts.org/Bookshelves/Physical_and_Theoretical_Chemistry_Textbook_Maps/Book%3A_Surface_Science_(Nix)/5%3A_Surface_Analytical_Techniques/5.3%3A_Photoelectron_Spectroscopy (accessed Nov 18, 2019).

(88)   Photoelectron Spectroscopy: Theory
         https://chem.libretexts.org/Bookshelves/Physical_and_Theoretical_Chemistry_Textbo
         ok_Maps/Supplemental_Modules_(Physical_and_Theoretical_Chemistry)/Spectroscop
         y/Photoelectron_Spectroscopy/Photoelectron_Spectroscopy%3A_Theory (accessed
         Nov 18, 2019).

(89)   Condon, E. U. Coupling of Electronic and Nuclear Motions in Diatomic Molecules. In
         Selected Scientific Papers of E.U. Condon; Barut, A. O., Odabasi, H., van der Merwe,
         A., Eds.; Springer: New York, NY, **1991**; pp 30–34.

(90)   Thorin, S. Design and Construction of a Velocity-Map Imaging Spectrometer. Master's
         Thesis, Lund University, **2004**.

(91)   Parker, D. H.; Eppink, A. T. J. B. Velocity Map Imaging: Applications in Molecular
         Dynamics and Experimental Aspects. In *Imaging in Molecular Dynamics: Technology
         and Applications*; Whitaker, B. J., Ed.; Cambridge University Press: Cambridge, **2003**;
         pp 20–64.

(92)   Andrews, D. H. Anion Photoelectron Spectroscopy. PhD Thesis, University of Colorado
         Boulder, **2006**.

(93)   León, I.; Yang, Z.; Liu, H.-T.; Wang, L.-S. The Design and Construction of a High-
         Resolution Velocity-Map Imaging Apparatus for Photoelectron Spectroscopy Studies of
         Size-Selected Clusters. *Rev. Sci. Instrum.* **2014**, *85* (8), 083106.

(94)   Reid, M. Velocity Map Imaging: From Gases to Surfaces. PhD Thesis, The University
         of Manchester, **2013**.

CHAPTER 2

EXPERIMENTAL METHODS

This chapter provides an overview of the experimental procedure employed in the photoelectron spectroscopic studies presented in this thesis. Specifically, details of the instrumentation and data processing techniques are presented alongside a discussion regarding the experimental parameters that can be obtained. The aspects of the experimental setup covered in this chapter have been reported in detail in previous publications by Josh Rogers,[1,2] who developed the experimental arrangement.

2.1 THE CLUSTER EXPERIMENT

To characterise gas-phase anions resonances experimentally, frequency-resolved photoelectron spectroscopy was employed using velocity map imaging (VMI) as an electron spectrometer.[3] A schematic diagram of the instrument in which anions are generated, mass-selected and irradiated is presented is in Figure 2.1. The experiment is referred to as the cluster experiment and can be divided into three regions: molecular-beam anion source, time-of-flight (TOF) and VMI detection, each of which will be discussed in the following subsections.

2.1.1 ANION SOURCE REGION

The generation of anions occurs within the source region of the cluster machine, which is typically operated at ~5×10^{-5} mbar and is labelled as Region **A** in Figure 2.1. A neutral molecular beam is generated when neutral molecules seeded in a carrier gas are ejected through a fast solenoid valve (Even-Lavie) that has a repetition rate of up to 1 kHz.[4] As the valve opens, gas exits through its orifice and subsequently undergoes a supersonic expansion into vacuum, where the analyte molecules are expanded in the carrier gas, forming cold molecular clusters. Throughout this thesis, either argon or helium has been used as the carrier gas. The molecular beam is intersected by an electron beam (300 eV of kinetic energy and a 1 mA beam current) which causes the formation of anions. Anions are produced by secondary electron attachment: carrier gas atoms are ionised by the 300 eV electrons to produce low-energy secondary electrons, which in turn can attach onto the analyte. The pulsed gas valve is mounted on a translation rod, allowing the position at which ionisation occurs within the expansion to be altered. The resulting molecular beam containing neutral, cations and anions is then directed into the mass spectrometer (Section 2.1.2).

The setup of the source region requires the sample to be in a gaseous phase. The Even-Lavie valve can be heated up to 250°C, permitting the study of molecules, which have a low vapour pressure at room temperature.
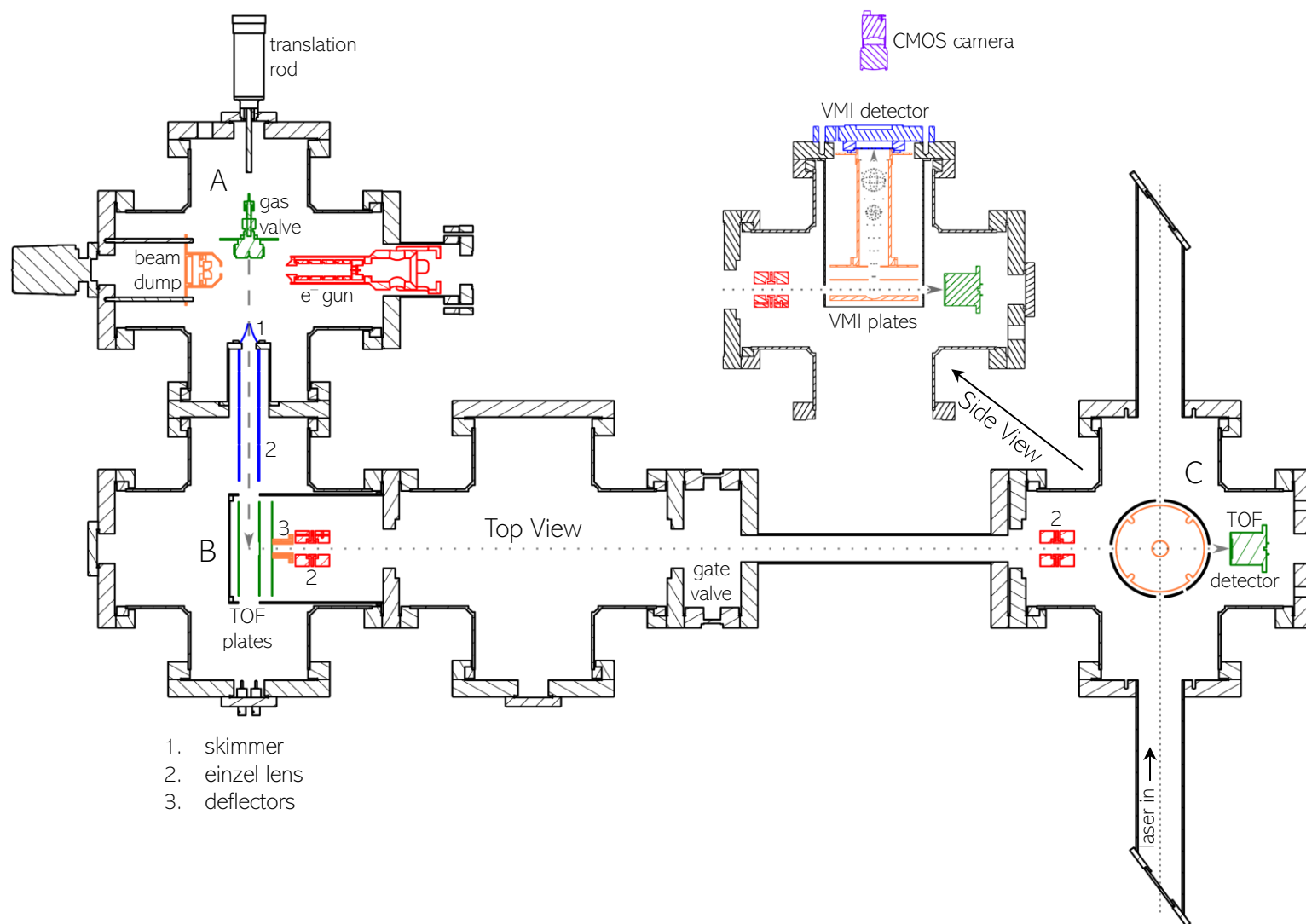
Figure 2.1: Schematic diagram of the cluster experiment as viewed from the top. **A** is the source region where anions are generated via electron impact of a pulsed neutral molecular beam. **B** is the time-of-flight region in which the ion of interest is mass selected. The anions initially pass through a set of time-of-flight plates and a drift tube, prior to entering Region **C**, the detection region, where the mass spectrometer is located. In this region, photoelectrons are generated through irradiation of the ion by incoming nanosecond laser pulses and imaged using a velocity map imaging PE spectrometer. A side view of the VMI assembly is shown in the inset. This figure has been reproduced from Ref [2].

2.1.2 TIME-OF-FLIGHT REGION

Electron impact of the molecular beam results in the formation of different anions alongside unionised neutral species and cations. These molecules travel collectively towards the TOF region, where the anion of interest can be extracted from the ion beam. This region is located 0.38 m from the pulsed valve and is labelled **B** in Figure 2.1. The TOF chamber has a typical operating pressure of $\sim5\times10^{-7}$ mbar.

The molecular beam enters the TOF region between the repeller and middle extractor plates (separated by 25 mm) and are rapidly pulsed at –3.00 and –2.68 kV, respectively. The difference in voltages accelerates the anions along the time-of-flight axis, while the pathway of neutral species within the molecular beam remain unaffected and cations are directed into the repeller. The anions are extracted perpendicularly from the beam to ensure that neutral molecules do not enter the detection region and are instead pumped out of the machine by a turbomolecular pump. The anions pass through the final, grounded TOF plate and into the 1.2 m drift region with $\sim$2.8 keV of kinetic energy. A set of deflectors and an einzel lens immediately follow the TOF plates, which aligns and collimates the emerging ion beam, respectively. As the anions travel along the drift region, they separate into ion packets according to their respective masses, allowing the anionic composition of the molecular beam to determined.

2.1.3 DETECTION REGION

SELECTION OF ANIONS

The end of the TOF drift region is marked by entry into the detection chamber, referred to as Region **C** in Figure 2.1. The detection chamber is typically operated at ultrahigh vacuum pressures of up to $\sim5\times10^{-7}$ mbar. To maintain the high pressure in this chamber, particularly when venting other chambers of the instrument, the detection region can be isolated from the preceding TOF region through the use of a gate valve. Located in the detection region is the latter part of a TOF spectrometer for the purpose of anion detection and a VMI assembly for the imaging of photoelectrons, the details of which have been discussed in the following section.

The TOF detector is comprised of a microchannel plate (MCP), coupled to a phosphor scintillator, followed by a photomultiplier tube (PMT). Ion packets emerging from the drift

region first pass through a fine steel mesh, which is held at 0 V, before striking the MCP which generates electrons from the anions. The front of the MCP can be held at high potential (up to +5 kV) which accelerates the anions into the MCP, providing enhanced detection efficiency, especially at high mass. The MCP also serves to amplify the electron signal which is achieved through secondary emission. A small difference in the voltage bias applied across the front and rear of the MCP, (+5.0 and +5.8 kV, respectively), provides the electron multiplication gain ($\sim 10^4$). Upon exiting the MCP, the electrons are further accelerated towards the phosphor screen (held at +8 kV). As the incident electrons strike the phosphor screen, a flash of light is generated, signalling the conversion of the electrons into photons. The PMT then converts the photons back into electrons, generating an electron current which is measurable by the oscilloscope.

DETECTION OF PHOTOELECTRONS

Immediately before the TOF detector, is the velocity map imaging spectrometer, which is used to map the velocity vectors of photodetached electrons onto a position sensitive detector. The VMI assembly has a similar setup to that of the TOF spectrometer and is comprised of a set of VMI plates, dual MCPs, phosphor screen and a position sensitive complementary metal oxide semiconductor (CMOS) camera.

The stack of three VMI plates comprises of repeller (bottom), extractor (middle) and front (top) plates arranged vertically over 36 mm, with the repeller plate lying 20 mm from the middle, extractor plate. Ion packets arriving in the detection chamber pass through a second einzel lens and over the repeller plate, entering from the side (perpendicular to the VMI axis). Between the repeller and extractor plates is the ion-laser interaction region, in which laser pulses are timed to perpendicularly intersect the ion packet of interest, resulting the photodetachment of an electron. At the centre of the extractor and front (top) plates are holes with respective diameters of 15 and 16 mm, which permit the passage of photoelectrons through the plates. The repeller plate is pulsed to –470 V, while the extractor plate is held at –35 V. The sizable reduction in voltage between the repeller and extractor plates minimises the number of ions passing through the VMI plates, thus reducing possible noise.

Linking the front plate to the dual MCPs at the front of the VMI detector, is a short drift tube. The front plate, drift tube and front surface of the MCP stack are all maintained statically at +650V, generating a field free region in which the cloud of photodetached

electrons arrange into a Newton sphere and expand upwards towards the detector. The electron signal is then amplified by the dual microchannel plates. The front is held at +0.65 kV, the back at +2.05 kV and the phosphor screen at +6.00 kV. Upon exiting the MCPs, the electrons strike the phosphor screen, generating a flash of light which is captured by a CMOS camera. The computer program LabVIEW interfaces the camera with the computer, allowing the raw photoelectron images to be acquired and further analysed.

2.2   LASER SYSTEM

The VMI spectrometer detailed in the previous section requires the use of a laser to generate photoelectrons. The experimental results presented in this thesis were obtained using a pulsed, nanosecond, tuneable optical parametric oscillator (OPO) (Continuum Horizon I), pumped by the third harmonic (355 nm) of a Nd:YAG laser (Continuum Surelite SL II-10). This produces ~5 ns laser pulses with a bandwidth of <10 cm^{-1} at a repetition rate of 10 Hz. The nanosecond laser is tuneable between 192–2750 nm, permitting the measurement of frequency-resolved photoelectron spectra over a broad photon energy range. A schematic of the laser setup is shown in Figure 2.2.
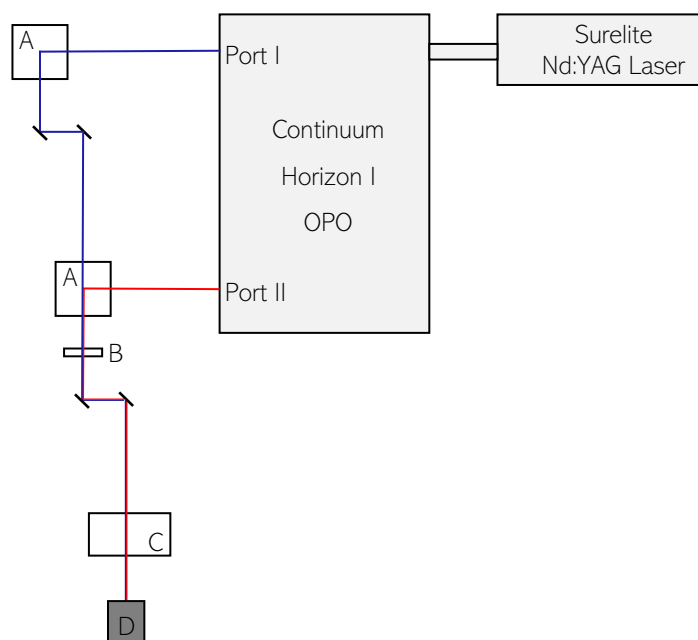
Figure 2.2: The layout of the nanosecond Nd:YAG laser system (Continuum Horizon I OPO pumped by a Continuum Surelite laser). The OPO laser has two output ports and their use is dependent on wavelength - Port I for 192 – 400 nm and Port II for 400 – 2750 nm. Emerging laser pulses pass through periscopes (A) and a λ/2 phase retardation plate (B), before entering the detection chamber through a CaF$_2$ window mounted on the side of the chamber (C). Unabsorbed photons collect in a beam dump (D) in the detection chamber.

2.3 DATA ANALYSIS

2.3.1 RECONSTRUCTION OF PHOTOELECTRON IMAGES

During the velocity-map-imaging process, the photodetached electrons expand upwards towards the detector in a 3D Newton sphere. As the electrons reach the detector surface, the 3D sphere is flattened onto the surface, creating a 2D map of the electrons' velocity vectors, that is imaged by the camera. The conversion of the electrons from three- to two-dimensional space results in the loss of some velocity vector information. As such, the 3D sphere needs to be reconstructed following data acquisition. It should be noted that reconstruction is only possible if the underlying 3D distribution only depends on two variables, *e.g.* has cylindrical symmetry. More specifically, the symmetry axis of the laser needs to be parallel to the detector's surface.

The 3D image is reconstructed using the polar onion peeling (POP) algorithm.[5] As a sphere is projected into a 2D circular image during the VMI process, working in polar coordinates is the most natural coordinate system. Therefore, the Cartesian image is first converted to polar coordinates. The POP algorithm then works by recognising that an infinitely narrow velocity distribution will produce a ring of a given radius and will have a contribution at smaller radii from the crushing of the 3D sphere onto a 2D plane. This contribution can be easily calculated for a given ring (with a given photoelectron angular distribution) and has been tabulated. As each ring only contributes to smaller radii, the POP algorithm starts at the outermost radius of the image and determines the intensity and angular distribution of the ring at this radius. From this, it looks-up the tabulated signal at smaller radii for that distribution and subtracts this from the total image. It then increments to a smaller radius and repeats the process for all radii. This then leaves a central slice through the 3D distribution.

2.3.2 CALIBRATION OF PHOTOELECTRON SPECTRA

The PE spectra presented in this thesis were calibrated using the PE spectrum of atomic iodide, which is presented in Figure 2.3 alongside the raw VMI image. Photodetachment from I$^-$ with photon energies of 4.00 eV or higher results in the direct detachment of an electron to either spin orbit state of neutral iodide, $^2P_{1/2}$ and $^2P_{3/2}$. This produces a distinct spectrum in which the two direct detachment features are separated by

0.942648 eV. In addition to the spin-orbit coupling value, the electron affinity of iodine is well known and has been reported with high precision as 3.0590465 eV.[6] The spectral resolution of the instrument is $\Delta eKE/eKE = 2.6\%$.
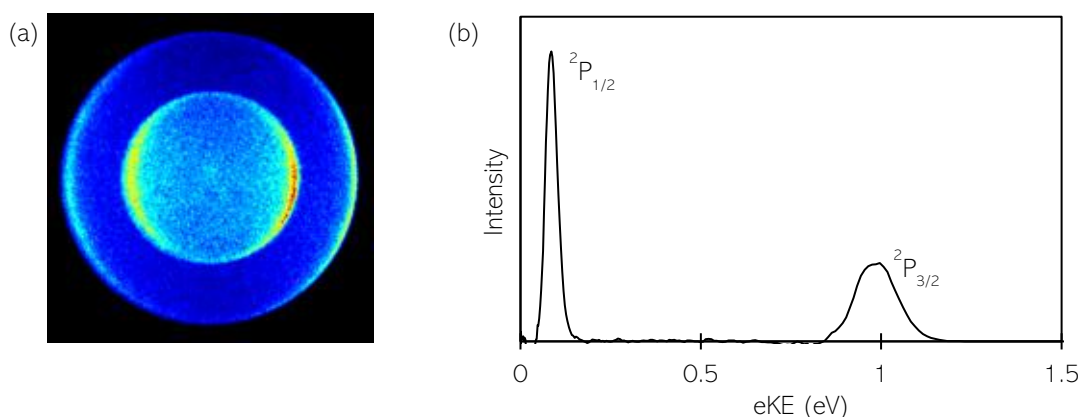

Figure 2.3: **(a)** The raw velocity map image of I^- measured at 4.1 eV, from which **(b)** the 1D photoelectron spectrum of I^- is constructed. The polarisation axis of the laser in **(a)** is vertical.

2.3.3 DETERMINATION OF ADIABATIC AND VERTICAL DETACHMENT ENERGIES

While this thesis is primarily concerned with the characterisation of electronic excited states, some ground state properties of the neutral have been determined to provide a complete picture of the relevant photophysical processes. Ground state properties of the neutral measurable from the photoelectron spectra include the measurement of adiabatic and vertical detachment energies, referred to as the ADE and VDE, respectively.

The ADE, or electron affinity, is defined in Figure 2.4 as the difference between the anion and neutral states, when both species are in the lowest ro-vibrational levels of their respective electronic ground states. The ADE is a threshold quantity that gives the energetic requirement for electron detachment from the anion to form a neutral species, and thus provides an indication of the thermodynamic stability of the initial anion. If a molecule has a positive ADE value, its anion is considered to be thermodynamically stable as it lies energetically below the neutral. Conversely, a negative value of EA is an indication of an unstable anion as the anionic form of the molecule lies energetically above that of the neutral parent species.[7,8]

The ADE can be determined from the energy at which the onset of the direct detachment feature occurs in photoelectron spectra.[9] Specifically, this can be ascertained by

fitting the falling edge of the direct detachment peak to a linear function which has a gradient of 1. Through extrapolation of this line down to zero eKE the ADE can be obtained. Unless otherwise stated, this method has been used throughout this thesis to ascertain the ADE and typically produces an error in the region of ±0.02 eV for the molecules studied in the following chapters. However, it is not always possible to measure the detachment values to this degree of accuracy, *e.g.* in cases where the PE signal is low or where the shape of the direct detachment band is influenced by another spectral detachment feature that is present at close energy. Instead, the ADE may be obtained through visual inspection of the 1D PE spectra, where the onset energy of the direct detachment band is determined by eye at the lowest photon energy possible. The resulting eKE is then subtracted from the photon energy to give the ADE. The lower degree of accuracy in this method is reflected by the increased error associated with the resulting detachment energy, which is typically ±0.1 eV for the molecules studied in this thesis.
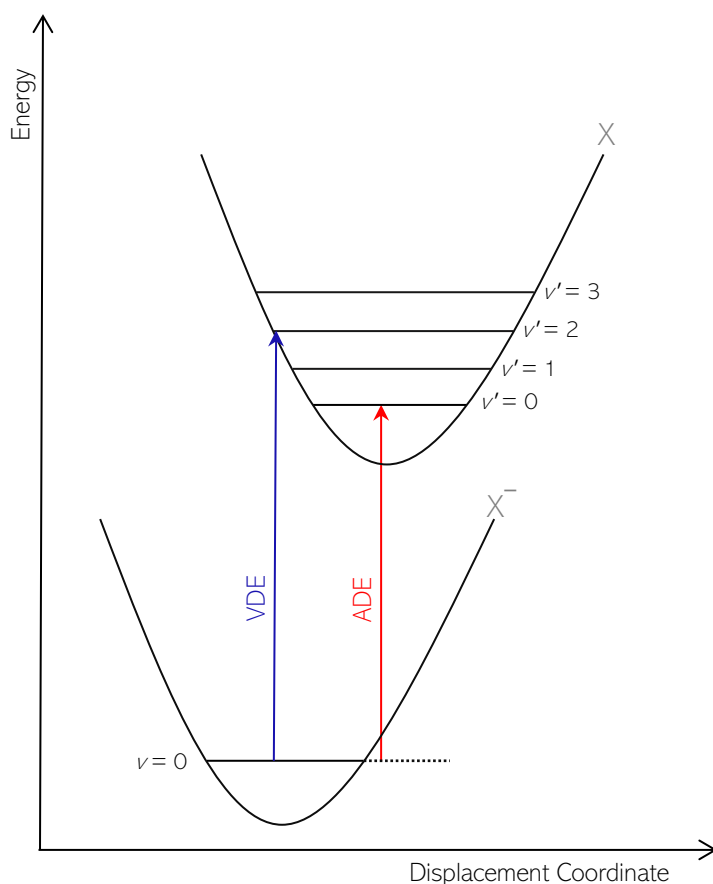

Figure 2.4: A qualitative representation of the vertical and adiabatic detachment energies as differences between the electronic states of the anion, X^- and neutral, X.

Often, the $v' = 0 \leftarrow v = 0$ (0-0) transition is not the most intense feature in the spectrum, as its Franck-Condon factor may be lower than to higher lying vibrational levels. The VDE of an anion is an alternative parameter that can be determined for the anion and neutral at the same (anion) geometry (Figure 2.4).[7,8] Within PE spectra, the VDE corresponds to the photon energy at which the direct detachment feature is most intense, *i.e.* the maximum of the direct detachment peak.[9] Throughout this thesis, the peak maximum has been obtained by visual inspection of the 1D PE spectra. Although there are more accurate ways to ascertain the experimental VDE, the level of accuracy provided by this method is satisfactory to draw qualitative conclusions regarding the spectroscopy and dynamics of the various systems that have been studied.

The determination of experimental ADEs and VDEs provides a benchmarking parameter for the computational data obtained. In this thesis, the calculated detachment energies were obtained using density functional theory (DFT) optimisation and single-point energy calculations to compute the absolute energy values for the relevant species, where[8]

$$\text{ADE} = E_{(\text{optimised neutral})} - E_{(\text{optimised anion})}$$

$$\text{VDE} = E_{(\text{neutral at optimised anion geom.})} - E_{(\text{optimised anion})}.$$

It should be noted that the above calculations do not include a vibrational correction to the optimisation energies, *i.e.* the zero-point vibrational energy (ZPVE) correction. The optimisation energy calculated by DFT gives the total energy of a system lying at the bottom of its potential well. The ZPVE correction keeps the total energy of the system in line with Heisenberg's uncertainty principle which requires the minimum energy of a quantum mechanical system to lie above that of its potential well. Omission of the ZPVE correction will inevitably introduce an error in the computed detachment energies. However, given that the theoretical detachment energies are used in reference to their experimental counterparts, the exclusion of the ZPVE correction is warranted if the energetic value of the correction is lower than the PE spectral resolution.

2.4 REFERENCES

(1)   Rogers, J. Photoelectron Spectroscopy of $(C_6F_6)_n^-$ and $(C_6F_6)I^-$ Clusters in a Novel Instrument. PhD Thesis, Durham University, **2017**.

(2)   Rogers, J. P.; Anstöter, C. S.; Bull, J. N.; Curchod, B. F. E.; Verlet, J. R. R. Photoelectron Spectroscopy of the Hexafluorobenzene Cluster Anions: $(C_6F_6)_n^-$ (n = 1–5) and $I^-(C_6F_6)$. *J. Phys. Chem. A* **2019**, *123* (8), 1602–1612.

(3)   Eppink, A. T. J. B.; Parker, D. H. Velocity Map Imaging of Ions and Electrons Using Electrostatic Lenses: Application in Photoelectron and Photofragment Ion Imaging of Molecular Oxygen. *Rev. Sci. Instrum.* **1997**, *68* (9), 3477–3484.

(4)   Even, U.; Jortner, J.; Noy, D.; Lavie, N.; Cossart-Magos, C. Cooling of Large Molecules below 1 K and He Clusters Formation. *J. Chem. Phys.* **2000**, *112* (18), 8068–8071.

(5)   Roberts, G. M.; Nixon, J. L.; Lecointre, J.; Wrede, E.; Verlet, J. R. R. Toward Real-Time Charged-Particle Image Reconstruction Using Polar Onion-Peeling. *Rev. Sci. Instrum.* **2009**, *80* (5), 053104.

(6)   Piani, G.; Becucci, M.; Bowen, M. S.; Oakman, J.; Hu, Q.; Continetti, R. E. Photodetachment and Dissociation Dynamics of Microsolvated Iodide Clusters. *Phys. Scr.* **2008**, *78* (5), 058110.

(7)   Simons, J. Molecular Anions. *J. Phys. Chem. A* **2008**, *112* (29), 6401–6511.

(8)   Rienstra-Kiracofe, J. C.; Tschumper, G. S.; Schaefer, H. F.; Nandi, S.; Ellison, G. B. Atomic and Molecular Electron Affinities: Photoelectron Experiments and Theoretical Computations. *Chem. Rev.* **2002**, *102* (1), 231–282.

(9)   Henley, A.; Fielding, H. H. Anion Photoelectron Spectroscopy of Protein Chromophores. *Int. Rev. Phys. Chem.* **2019**, *38* (1), 1–34.

CHAPTER 3

COMPUTATIONAL METHODS

The theoretical basis for the computational techniques used throughout this thesis is considered in this chapter, beginning with a discussion centred on the Schrödinger equation and its relevance to quantum mechanical methods. Justification for the use of density functional theory based methods in the study of larger electronic systems is given, in addition to a discussion regarding the choice of functionals and basis sets employed in calculations. This chapter concludes with theoretical aspects to consider when treating anions using electronic structure methods.

3.1 THE ELECTRONIC SCHRÖDINGER EQUATION

Quantum mechanical (QM) computational methods provide a complimentary means by which to study the electronic states of anions. The aim of computational QM methods is to solve the Schrödinger equation, from which the ground and excited state properties of a quantum system can be described.[1] The Schrödinger equation can be expressed in its time-independent form as

$$\hat{H}\Psi(\boldsymbol{r}, \boldsymbol{R}) = E\Psi(\boldsymbol{r}, \boldsymbol{R}), \tag{3.1}$$

where $\hat{H}$ is the Hamiltonian operator, Ψ is the wavefunction, E is the total energy of the system. The variables in Equation 3.1 are defined by all of the electrons and nuclei in the system, where $\boldsymbol{r}$ and $\boldsymbol{R}$ give the electronic and nuclear coordinates, respectively.[1,2] The Hamiltonian operates on the wavefunction to return the system energy and is defined as the sum of the kinetic $\hat{T}$ and potential $\hat{V}$ energy operator terms with respect to the electronic and nuclear interactions

$$\hat{H} = \hat{T}_e(\boldsymbol{r}) + \hat{T}_n(\boldsymbol{R}) + \hat{V}_{ee}(\boldsymbol{r}) + \hat{V}_{ne}(\boldsymbol{r}, \boldsymbol{R}) + \hat{V}_{nn}(\boldsymbol{R}), \tag{3.2}$$

where $\hat{T}_e$ and $\hat{T}_n$ correspond to the electronic and nuclear kinetic energy operators, respectively, $\hat{V}_{ee}, \hat{V}_{ne}$ and $\hat{V}_{nn}$ denote the electron-electron repulsion, nuclear-electron attraction and nuclear-nuclear repulsion energy operators, respectively.[2,3]

The Schrödinger equation can be simplified through the implementation of the Born-Oppenheimer approximation. Given the large difference in mass between electrons and nuclei, the motion of nuclei is significantly slower than that of the electrons within the system. Therefore, the electronic and nuclear motions within the Schrödinger equation can be decoupled through the use of separate terms to describe the nuclear and electronic parts of the wavefunction. The difference in motion can be considered so sizable as to allow the near-instantaneous response of electrons to changes in nuclear motion. Consequently, the nuclear position is regarded as stationary with respect to the electronic motion, allowing the electronic Schrödinger equation to be solved at fixed nuclear coordinates

$$\hat{H}_{elec}\Psi_{elec}(\boldsymbol{r}; \boldsymbol{R}) = E_{elec}(\boldsymbol{R})\Psi_{elec}(\boldsymbol{r}; \boldsymbol{R}). \tag{3.3}$$

In this case, $\boldsymbol{R}$ becomes a parameter upon which the electronic Hamiltonian, its eigenstates and eigenvalues depend. Given that Equation 3.3 does not consider nuclear motion, the electronic Hamiltonian takes the form

$$\hat{H}_{elec} = \hat{T}_e(\boldsymbol{r}) + \hat{V}_{ee}(\boldsymbol{r}) + \hat{V}_{ne}(\boldsymbol{r}; \boldsymbol{R}) + \hat{V}_{nn}(\boldsymbol{R}), \tag{3.4}$$

where $\hat{V}_{nn}$ becomes an additive constant which systematically shifts the eigenvalues.[1,2,4] The solutions to Equation 3.3 give rise to the concept of a potential energy surface (PES), in which the electronic energy of a system is determined as a function of its nuclear configuration.[4]

3.2   DENSITY FUNCTIONAL THEORY

For a one-electron system, the Schrödinger equation can be solved exactly, obtaining the electronic energy and the wavefunction. For a system containing N electrons, the wavefunction is defined by $3N$ spatial + N spin variables. Due to the wavefunction's dependency on N, it becomes exponentially difficult to compute solutions to the wavefunction as the size of the system increases. Density functional theory (DFT) reduces the difficulty of solving the Schrödinger equation for larger systems, by circumventing the wavefunction and instead, using electron density as its central quantity. As electron density is determined only by three Cartesian coordinates, the complexity of the problem is, in principle, greatly reduced.[1,4]

The quantitative basis of DFT was provided by Hohenberg and Kohn,[5] who proved the relationship between electron density and the ground-state properties of a system. The first Hohenberg-Kohn theorem uses a *reductio ad absurdum* argument to demonstrate that the ground-state electron density, $\rho(r)$, of a system uniquely determines the external potential, $v_{\text{ext}}(\boldsymbol{r})$. The external potential refers to the nuclear Coulomb attraction experienced by the electrons, *i.e.* $\hat{V}_{ne}$ in Equation 3.4. The conclusion of this argument is significant as it proves that the electron density can be used to calculate the external potential and the number of electrons $N,$ in terms of which the Hamiltonian is expressed. Through the calculation of the Hamiltonian, solutions to the Schrödinger equation and thus, the ground-state properties of a system can be determined. It then follows that the total electronic energy of the system in its ground state, E, can be expressed in as a functional of the electron density as

$$E[\rho] = F[\rho] + \int v_{\text{ext}}(\boldsymbol{r})\rho(\boldsymbol{r})d\boldsymbol{r}, \qquad (3.5)$$

where $F[\rho]$ is a universal density functional which can be applied to any system to describe its kinetic and electron-electron interaction potential energy contributions,

$$F[\rho] = T[\rho] + V_{\text{ee}}[\rho]. \qquad (3.6)$$

The second Hohenberg-Kohn theorem provides a variational principle, where the exact density minimises Equation 3.5, subject to the constraint that N remains constant.[1,4–7]

The Hohenberg-Kohn theorem is purely a proof of existence and does not provide a method for obtaining an explicit form of the kinetic energy or electron-electron interaction terms.[1] A solution to this can be found in the Kohn-Sham (KS) method,[8] the framework upon which modern DFT is built. This approach introduces a system of non-interacting particles moving in an effective potential. The electron density of the non-interacting system, $\rho(\boldsymbol{r})$, is expressed in terms of one-electron orbitals, φ_i and is constructed to equal the electron density of the real, interacting system,

$$\rho(\boldsymbol{r}) = \sum_i^N |\varphi_i(\boldsymbol{r})|^2 .$$

(3.7)

These orbitals are obtained from the KS equations

$$\left(-\frac{1}{2}\nabla^2 + v_{\text{ks}}(\boldsymbol{r})\right)\varphi_i(\boldsymbol{r}) = \epsilon_i\varphi_i(\boldsymbol{r}),$$

(3.8)

where v_{ks} is the KS potential which can further be defined as

$$v_{\text{ks}}(\boldsymbol{r}) = v_{\text{ext}}(\boldsymbol{r}) + v_{\text{J}}(\boldsymbol{r}) + v_{\text{xc}}(\boldsymbol{r}),$$

(3.9)

where v_{ext} is the external potential, v_{J} is the classical Coulombic potential and v_{xc} is the exchange-correlation potential, which is unknown.

The kinetic energy of the non-interacting system can be expressed exactly as

$$T_{\text{s}}[\rho] = -\frac{1}{2}\sum_{i=1}^N \varphi_i(\boldsymbol{r})\nabla^2\varphi_i(\boldsymbol{r})d\boldsymbol{r},$$

(3.10)

with its value lying close to the kinetic energy of the real interacting system. The difference in energy between the two systems is accounted for by the addition of a corrective term to T_{s} (Equation 3.12). A first approximation for V_{ee} can be found in the form of the classical Coulomb energy

$$J[\rho] = \frac{1}{2}\iint \frac{\rho(\boldsymbol{r})\rho(\boldsymbol{r}')}{|\boldsymbol{r} - \boldsymbol{r}'|}d\boldsymbol{r}d\boldsymbol{r}',$$

(3.11)

with the difference between J and V_{ee} assigned to a non-classical corrective term. In the KS method, these corrective terms are grouped together and are referred to as the exchange-correlation energy functional,

$$E_{xc}[\rho] = (T[\rho] - T_s[\rho]) + (V_{ee}[\rho] - J[\rho]). \tag{3.12}$$

The total energy of the system can then be redefined as

$$E[\rho] = T_s[\rho] + J[\rho] + E_{xc}[\rho] + \int v_{ext}(\boldsymbol{r})\rho(\boldsymbol{r})d\boldsymbol{r}. \tag{3.13}$$

In practice, all of the functional terms in Equation 3.13 can be computed exactly with the exception of the exchange-correlation energy functional which is unknown and therefore must be approximated.[1,2,6,8,9]

3.3   TIME-DEPENDENT DENSITY FUNCTIONAL THEORY

KS-DFT provides a practical method for studying the ground state properties of a static system. The Hohenberg-Kohn theorem relies on a variational principle and thus, renders its use unsuitable to the general excited state case, which requires the calculation of higher lying states. If the properties of excited electronic states are to be investigated, a time-dependent extension of DFT, TDDFT must be employed.[6,9]

TDDFT involves studying the response of a dynamic system to a time-dependent external potential, *i.e.* the potential arising from an external field applied to the system such as a magnetic field.[9,10] The formal basis of TDDFT lies within the Runge-Gross theorem,[11] the time-dependent analogue of the first Hohenberg-Kohn theorem within DFT, in which the relationship between the electron density, $\rho(\boldsymbol{r},t)$ and time-dependent external potential, $v(\boldsymbol{r},t)$ is proven for a many-body system evolving from an initial given state. With knowledge of the exact electron density, the external potential can be determined, which itself can be used to identify the Hamiltonian, allowing the time-dependent Schrödinger equation to be solved.[6,9,11]

To calculate the total energy of a dynamic system, time-dependent Kohn-Sham equations can be constructed. Similarly to the ground-state case, the time-dependent KS model uses a system of non-interacting particles occupying one-electron orbitals, $\varphi_i(\boldsymbol{r},t)$ which yield the same electron density as the real, interacting system. The time-dependent KS equations are

$$\left(-\frac{1}{2}\nabla^2 + v_{ks}(\boldsymbol{r},t)\right)\varphi_i(\boldsymbol{r},t) = i\frac{\partial}{\partial t}\varphi_i(\boldsymbol{r},t), \tag{3.14}$$

where

$$v_{ks}(\boldsymbol{r},t) = v_{ext}(\boldsymbol{r},t) + v_J(\boldsymbol{r},t) + v_{xc}(\boldsymbol{r},t). \tag{3.15}$$

$v_{xc}(\boldsymbol{r},t)$ is unknown and must be approximated.[6,9]

3.4 EXCHANGE-CORRELATION FUNCTIONALS

Numerous classes of density functionals exist to approximate the exchange-correlation energy term, with their development prompted by the lack of a truly "universal" functional that is applicable to all systems and properties.[2] Functionals are arranged in the so-called "Jacob's Ladder" of approximations, where each higher rung of the ladder represents a step closer to chemical accuracy.[2,6] The simplest approximations are local density approximation (LDA) functionals, which locally apply expressions that are exact for a uniform gas, making them particularly suited to the study of bulk solids.

LDA functionals provide a starting point for more sophisticated approximations of the exchange-correlation term. One such example is the generalised gradient approximation (GGA) functionals which improves the description through the inclusion of a gradient correction term that takes some account of the inhomogeneity of the electron density.[1–3,6,7]

Arguably the most commonly used functional, B3LYP,[12] belongs to a grouping known as hybrid functionals, in which a fraction of the exactly computed exchange interaction energy is included.[1,2] The exchange energy is the energy lowering associated with the Pauli principle which requires the many-body wavefunction to be antisymmetric with respect to an interchange of any two electron space-spin coordinates. Hartree-Fock (HF) theory satisfies the anti-symmetry requirement through its use of Slater determinants which express the electronic wavefunction as an antisymmetrised product of single-particle orbitals and gives rise to the HF exchange term which is exact

$$E_{\text{x}}^{\text{HF}} = -\frac{1}{2}\sum_{i,j}^{\text{occ}} \int \frac{\psi_i^*(\boldsymbol{r})\psi_j^*(\boldsymbol{r'})\psi_j(\boldsymbol{r})\psi_i(\boldsymbol{r'})}{|\boldsymbol{r}-\boldsymbol{r'}|} d\boldsymbol{r}d\boldsymbol{r'},$$

(3.16)

where the occupied orbitals, ψ_i and ψ_j, possess parallel spins.[2,4,13] B3LYP incorporates 20% exact HF exchange in addition to the B88 exchange and Lee Yang Parr correlation GGA functionals which act as correction terms to the local density spin approximation exchange-correlation functional. Three parameters, which are fitted to experimental data, are used to determine the amount of exact exchange and GGA correction terms included in B3LYP.[1,2,12]

While the addition of a fraction of exact exchange enhances the performance of exchange-correlation functionals, hybrid functionals still suffer from inaccuracies in areas such as the calculation of long-range excitations (e.g. excitations of a Rydberg or charge transfer

nature).[14,15] Long-range corrected functionals such as CAM-B3LYP and ωB97X were formulated with a partition of the short- and long-range interaction terms to improve the description of long range excitations. Range separation allowed the incorrect long-range interaction term to be described with an increased accuracy using exact HF exchange, while the short-range interactions were approximated using DFT exchange.[14–17]

3.5   BASIS SETS

DFT calculations necessitate the use of a basis set, a set of one-electron functions, to provide a mathematical description of a system's molecular orbitals. Slater-type orbitals (STOs) and Gaussian-type orbitals (GTOs) are common choices. In comparison to GTOs, STOs are regarded as a more accurate representation of hydrogenic orbitals as they display the correct radial dependence at short and long range. GTOs fail to reproduce the distinct electron cusp at short range and decay to zero too rapidly at long range.

Although STOs provide a superior description, they are computationally expensive, making the use of GTOs preferential. A combination of GTOs is often used to reproduce the radial accuracy of an STO. In this case, the functions are referred to as Gaussian primitives and are arranged in a linear combination, with n Gaussian primitives forming a single contracted GTO function, CGTO,

$$\phi_{\mathrm{CGTO}} = A \sum_{i=1}^{n} c_i x^a y^b z^c e^{-\zeta r^2}$$

(3.17)

where A is a normalisation constant, c_i is a contraction coefficient, x, y and z are atom centred Cartesian co-ordinates, a, b and c are positive integers which sum to describe the angular momentum of the function and ζ is an exponent that controls the radial extent of the primitive with inverse proportionality—an increasing value of ζ corresponds to decreasing diffuseness of the orbital. r is the radial distance from the nucleus.[1,2,4]

A popular family of basis sets employing CGTOs are those developed by Pople *et al.*[18–21] These basis sets are categorised as split-valence as a single CGTO is used to describe the core 1s orbital, in comparison to the valence region, for which multiple CGTOs are employed. Split-valence basis sets aim to reduce computational expense by the minimal use of functions on the chemically unperturbed core orbital, while maintaining computational accuracy through

the enhanced description of the chemically significant valence orbitals which are involved in bonding. Pople basis sets are usually denoted as *N-MP*G where *N, M* and *P* are positive integers that give the number of primitives used to compose each CGTO and G denotes the use of Gaussian functions. The number of integers before and after the hyphen give the number of CGTOs used to describe the core and valence orbitals, respectively.[2,4]

Basis sets are often extended through the use of diffuse functions, which are employed to describe broad electron distributions. Diffuse functions are additional basis functions with small values of ζ that decay slowly at long range. In Pople basis sets, the plus sign (+) signifies the use of diffuse functions. A single + denotes that diffuse functions have been added to heavy atoms. ++ specifies the use of diffusion functions on both light (hydrogen) and heavy atoms.[4,22,23]

Basis sets can be further amended using polarisation functions which account for the asymmetry in charge density that arises from molecular bonding. These functions correspond to extra basis functions of higher angular momenta. In Pople basis sets, the use of polarisation functions can be inferred through two types of notation. One method is to explicitly state in brackets the angular momenta of the additional functions added. The alternative notation style employs an asterisk sign (*). A single asterisk signifies the addition of polarisation functions to heavy atoms, while a double asterisk denotes the use of polarisation functions on light atoms.

3.6   THEORETICAL CONSIDERATIONS OF ANIONS

Special consideration is required when treating anions and their excited states with electronic structure methods to ensure their accurate description. Specifically, within approximate DFT, anions are known to suffer from formal problems relating to the energy of the highest occupied molecular orbital (HOMO). The HOMO is incorrectly computed by many approximate exchange-correlation functionals as a positive value, which corresponds to an unbound electron and fractional electron loss, *i.e.* a fraction of the excess electron is unbound with respect to the molecule and leaves the system The positive HOMOs can yield incorrect neutral electron affinities making this formal issue problematic in practical calculations. The erroneous orbital energies have been attributed to the incorrect long-range behaviour of the exchange-correlation potential and can also be understood from an electronic energy *vs* electron number perspective.[24,25] To account for this deficiency, the use of a long-range

corrected functional is recommended and it is for this purpose that these functionals have been employed extensively throughout this thesis.[14,24]

When investigating anions, a larger, more flexible basis set is required to describe the diffuse nature of the species. In anions, the excess electron is loosely bound, creating a region of electron density that exists at a significant distance from the nuclei in which the excess electron experiences reduced repulsion from the electrons in the valence region. The unique spatial extent of anions can be reflected through the use of diffuse functions, which provide a more accurate description of the decay behaviour of the basis set at larger radial distances. This thesis is concerned with the study of larger molecular anions, for which their diffuse nature is more pronounced, making the use of diffuse functions necessary. The computational studies detailed in this thesis have employed the Pople family of basis sets which have been extended with diffuse functions.[4,22]

The introduction of diffuse functions can be problematic for metastable electronic states which tend to collapse on to approximate solutions of the neutral + electron continuum, *i.e.* discretised continuum states (DCSs).[26] These states appear highly diffuse in nature as they are a description of electron loss, where the electron lies at a considerable distance from the neutral core. Mixing often occurs between the virtual orbitals of DCSs and valence molecular orbitals, resulting in a number of valence states possessing continuum character. As such, the inclusion of DCSs within the computed electronic solutions can result in inaccuracies regarding the character and excitation energies of resonance states. When studying anion resonances using electronic structure methods, it is necessary to incorporate an additional technique within the calculation which will discriminate between DCSs and the states of interest.[22]

A commonly used technique is the stabilisation method, in which trends in the electronic excitation energies are studied in response to the systematic variation of the basis set diffuseness.[27] DCSs are highly sensitive to changes in the diffuseness of the basis set and therefore will rapidly vary their electronic energies as the basis set is scaled. Contrastingly, resonance states and their energies are largely unaffected by changes to the spatial extent of the basis set. In practical calculations, variation in the basis set diffuseness is achieved through the incremental scaling of the basis set exponent, ζ.

The stabilisation method has parallels to the particle-in-a-box model, where the diffuseness of the basis set is akin to the length of the box, L. The rapid variation in energy of the DCSs as a function of basis set diffuseness can be likened to the relationship between L and the energy of the system, which scales inversely quadratically. Particular values of L (or basis set exponent) yield continuum wavefunctions that are of equivalent character, in terms of their energy, amplitude, phase and gradient, to that of the resonance wavefunction at short (valence) radial distances. In stabilisation plots of excitation energy $vs\ \zeta$, these regions correspond to avoided crossings, where both the DCS and resonance are of metastable valence character. An example of such a plot is presented in Figure 3.1, where the energy of the resonance can be identified by eye from a series of avoided crossings between the resonance and DCSs. Within this region of avoided crossings, the energy of the resonance remains stable with changing ζ.[22,28]
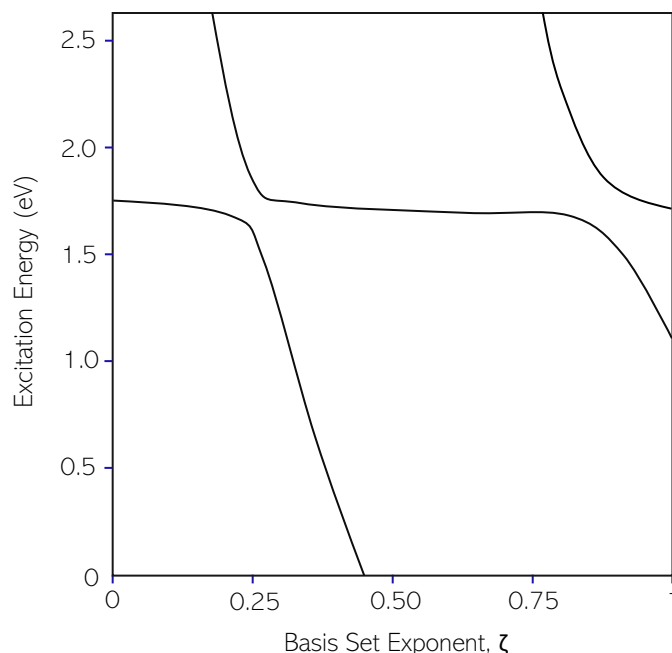

Figure 3.1: Stabilisation plot showing the variation in energy of excited anion states as a function of the basis set exponent.

An alternative to the stabilisation method is the addition of a complex absorbing potential (CAP) in calculations. This method effectively places the DCSs in a box, forcing the continuum wavefunctions to take discrete energy values. The addition of an artificial potential to the peripheral region of the box allows the long-range part of the wavefunction (which describes the detached electron) to be absorbed, leaving the short range, valence part of the function. Both the stabilisation method and CAP enjoy widespread use in the study of anion resonances.[28,29] In a recent benchmark study of small and medium sized anions by Thodika *et*

al.,[30] the performance of these methods were deemed comparable in the determination of resonance energies. A broad aim of this thesis is to test a computationally inexpensive and user-friendly theoretical workflow to aid experimental analysis and provide a qualitative characterisation of anion resonances. The studies presented in the following chapters have utilised the stabilisation method in place of CAP as it requires the optimisation of far fewer parameters and scales less expensively with larger systems, making this technique preferable for the aims of this thesis.

3.7 REFERENCES

(1) Koch, W.; Holthausen, M. C. *A Chemist's Guide to Density Functional Theory*; John Wiley & Sons, **2015**.

(2) Jensen, F. *Introduction to Computational Chemistry*; Wiley, **2007**.

(3) Burke, K.; Wagner, L. O. DFT in a Nutshell. *Int. J. Quantum Chem.* **2013**, *113* (2), 96–101.

(4) Cramer, C. J. *Essentials of Computational Chemistry: Theories and Models*; John Wiley & Sons, **2013**.

(5) Hohenberg, P.; Kohn, W. Inhomogeneous Electron Gas. *Phys. Rev.* **1964**, *136* (3B), B864–B871.

(6) Burke, K. *The ABC of DFT*; University of California, Irvine, **2007**.

(7) Capelle, K. A Bird's-Eye View of Density-Functional Theory. *Braz. J. Phys.* **2002**, *36*.

(8) Kohn, W.; Sham, L. J. Self-Consistent Equations Including Exchange and Correlation Effects. *Phys. Rev.* **1965**, *140* (4A), A1133–A1138.

(9) Ullrich, C. A.; Yang, Z. A Brief Compendium of Time-Dependent Density Functional Theory. *Braz. J. Phys.* **2014**, *44* (1), 154–188.

(10) Gross, E. K. U.; Maitra, N. T. Introduction to TDDFT. In *Fundamentals of Time-Dependent Density Functional Theory*; Marques, M. A. L., Maitra, N. T., Nogueira, F. M. S., Gross, E. K. U., Rubio, A., Eds.; Lecture Notes in Physics; Springer: Berlin, Heidelberg, **2012**; pp 53–99.

(11) Runge, E.; Gross, E. K. U. Density-Functional Theory for Time-Dependent Systems. *Phys. Rev. Lett.* **1984**, *52* (12), 997–1000.

(12) Becke, A. D. Density-functional Thermochemistry. III. The Role of Exact Exchange. *J. Chem. Phys.* **1993**, *98* (7), 5648–5652.

(13) Ioannidis, E. I.; Kulik, H. J. Towards Quantifying the Role of Exact Exchange in Predictions of Transition Metal Complex Properties. *J. Chem. Phys.* **2015**, *143* (3), 034104.

(14) Yanai, T.; Tew, D. P.; Handy, N. C. A New Hybrid Exchange-Correlation Functional Using the Coulomb-Attenuating Method (CAM-B3LYP). *Chem. Phys. Lett.* **2004**, *393* (1), 51–57.

(15)   Tsuneda, T.; Hirao, K. Long-Range Correction for Density Functional Theory. *WIREs Comput. Mol. Sci.* **2014**, *4* (4), 375–390.

(16)   Chai, J.-D.; Head-Gordon, M. Systematic Optimization of Long-Range Corrected Hybrid Density Functionals. *J. Chem. Phys.* **2008**, *128* (8), 084106.

(17)   Chai, J.-D.; Head-Gordon, M. Long-Range Corrected Hybrid Density Functionals with Damped Atom-Atom Dispersion Corrections. *Phys. Chem. Chem. Phys.* **2008**, *10* (44), 6615–6620.

(18)   Ditchfield, R.; Hehre, W. J.; Pople, J. A. Self-Consistent Molecular-Orbital Methods. IX. An Extended Gaussian-Type Basis for Molecular-Orbital Studies of Organic Molecules. *J. Chem. Phys.* **1971**, *54* (2), 724–728.

(19)   Krishnan, R.; Binkley, J. S.; Seeger, R.; Pople, J. A. Self-consistent Molecular Orbital Methods. XX. A Basis Set for Correlated Wave Functions. *J. Chem. Phys.* **1980**, *72* (1), 650–654.

(20)   Pietro, W. J.; Francl, M. M.; Hehre, W. J.; DeFrees, D. J.; Pople, J. A.; Binkley, J. S. Self-Consistent Molecular Orbital Methods. 24. Supplemented Small Split-Valence Basis Sets for Second-Row Elements. *J. Am. Chem. Soc.* **1982**, *104* (19), 5039–5048.

(21)   Gordon, M. S.; Binkley, J. S.; Pople, J. A.; Pietro, W. J.; Hehre, W. J. Self-Consistent Molecular-Orbital Methods. 22. Small Split-Valence Basis Sets for Second-Row Elements. *J. Am. Chem. Soc.* **1982**, *104* (10), 2797–2803.

(22)   Simons, J. Molecular Anions. *J. Phys. Chem. A* **2008**, *112* (29), 6401–6511.

(23)   Bort, J. A.; Rusca, J. B. *Theoretical and Computational Chemistry: Foundations, Methods and Techniques*; Publicacions de la Universitat Jaume I, **2007**.

(24)   Peach, M. J. G.; Teale, A. M.; Helgaker, T.; Tozer, D. J. Fractional Electron Loss in Approximate DFT and Hartree-Fock Theory. *J. Chem. Theory Comput.* **2015**, *11* (11), 5262–5268.

(25)   Kim, M.-C.; Sim, E.; Burke, K. Communication: Avoiding Unbound Anions in Density Functional Calculations. *J. Chem. Phys.* **2011**, *134* (17), 171103.

(26)   Cheng, H.-Y.; Shih, C.-C. Application of the Stabilization Method to the π* Temporary Anion States of Benzene and Substituted Benzenes in Density Functional Theory. *J. Phys. Chem. A* **2009**, *113* (8), 1548–1554.

(27)   Hazi, A. U.; Taylor, H. S. Stabilization Method of Calculating Resonance Energies: Model Problem. *Phys. Rev. A* **1970**, *1* (4), 1109–1120.

(28)   Sommerfeld, T.; Santra, R. Efficient Method to Perform CAP/CI Calculations for Temporary Anions. *Int. J. Quantum Chem.* **2001**, *82* (5), 218–226.

(29)   Sommerfeld, T.; Riss, U. V.; Meyer, H.-D.; Cederbaum, L. S.; Engels, B.; Suter, H. U. Temporary Anions - Calculation of Energy and Lifetime by Absorbing Potentials: The Resonance. *J. Phys. B At. Mol. Opt. Phys.* **1998**, *31* (18), 4107–4122.

(30)   Thodika, M.; Fennimore, M.; Karsili, T. N. V.; Matsika, S. Comparative Study of Methodologies for Calculating Metastable States of Small to Medium-Sized Molecules. *J. Chem. Phys.* **2019**, *151* (24), 244104.

CHAPTER 4

LOW-ENERGY ELECTRON IMPACT RESONANCES OF ANTHRACENE

In this chapter, Frequency-Resolved Anion Photoelectron Imaging has been applied to an open shell system of interstellar relevance, anionic anthracene. This method yields 2D photoelectron plots from which the spectroscopic signature of anthracene has been characterised and possible decay mechanisms of the anion have been inferred. Particular emphasis has been placed on the characterisation of anion resonances and it is for this purpose that a complementary computational study of the molecule has been included. The applicability of time-dependent density functional theory and the basis set stabilisation method to the study of metastable states for a medium sized molecule is demonstrated, providing an evidentiary basis for the extension of these methods to larger systems. This chapter is based on the following publication:

4.1 INTRODUCTION

Polycyclic aromatic hydrocarbons (PAHs) are of interest because of their ubiquity in various research areas including medicinal chemistry, atmospheric sciences, combustion chemistry, astrochemistry and molecular electronics.[1–5] Many of the important properties and uses of PAHs are linked to their electronic structure and excited states. As an example, singlet fission (absorption of a single photon leading to the generation of two electron-hole pairs) in tetracene and pentacene is used in photovoltaic cells and other semiconducting devices,[6–8] although aspects of the mechanism remain unclear.[9] In the context of the interstellar medium (ISM), PAHs are believed to be the main store for carbon and play a role in the processes that govern physical properties of the ISM, such as photoelectric heating of molecular clouds and the regulation of charge balance through reactions with cations.[10,11] PAHs are also of interstellar interest due speculation surrounding their possible role as carriers of the diffuse interstellar bands (DIBs).[12–17] To date, C_{60}^+ has been identified,[18] but other PAHs have yet to be discovered in the ISM.[19] PAHs exist in regions where UV radiation and free electrons are present, making the formation of charged PAHs likely. In particular, the store of low-energy electrons may lead to the formation of anions.[20,21] The identification of interstellar PAH anions and their potential significance in interstellar photochemical processes necessitates the need for a comprehensive understanding of PAH anion formation and the characterisation of their electron impact resonances.[21] Here, we present a frequency-resolved (2D) photoelectron (PE) study of the anthracene radical anion, $C_{14}H_{10}^-$, characterising the anion resonances that lie within the first 3.7 eV of the neutral continuum.

Anthracene is the smallest linear PAH with a positive electron affinity[22] and is often viewed as an ideal test molecule to probe the photophysical properties of PAHs. While there is a wealth of studies pertaining the electronic characteristics of the neutral, much less work has been carried out on the anion, $C_{14}H_{10}^-$.[23–27] Schiedt and Weinkauf used photodetachment and PE spectroscopy on jet-cooled anthracene and its complex with a single water molecule,[25] Song *et al.* studied anionic clusters of anthracene $(C_{14}H_{10})_n^-$ ($n = 1 - 16$) by photoelectron specotroscopy,[26] and more recently, Kregel *et al.* presented a very high resolution slow-electron photoelectron imaging of $C_{14}H_{10}^-$.[27] The latter has accurately determined the electron affinity of anthracene as 0.532(3) eV. The PE spectra by Song *et al.* at wavelengths of 532, 610 and 700 nm contained clear evidence of indirect detachment features that were red-shifted relative to the direct detachment peak accessing the neutral ground state. The spectral range in which this indirect band appeared was consistent with the vertical excitation energy previously

reported for a π* resonance,[23,28] from which autodetachment can occur. While individual PE spectra can indicate the presence of a resonance, it does not encapsulate overall trends in the location and width of resonances or their dynamics. We have developed 2D PE spectroscopy to identify such trends and dynamical fingerprints.[29] As an optical analogue of 2D electron energy loss spectroscopy,[30,31] it also provides a direct link to electron spectroscopy. Several electron impact resonances of $C_{14}H_{10}{}^-$ have also been observed in electron transmission spectra,[28] identifying a number of prominent and well-resolved π* resonances over the first few eV of the continuum.[32–38]

Computationally, there has been some work on characterising $C_{14}H_{10}{}^-$.[37,39–41] However, because of its size and open-shell electronic structure, these have been limited. The size of $C_{14}H_{10}{}^-$ lends itself well to Density Functional Theory (DFT) calculations and provides a platform for extending to larger PAHs. However, open-shell anionic species have traditionally proved more challenging to compute than their neutral counterparts.[42] Dessent used anthracene as a test molecule in a DFT benchmark study of the ground state vibrational properties of the neutral and anion,[39] and Kreger *et al.* showed good agreement between their DFT calculations and vibrational structure in the high-resolution PE spectra.[27] Malloci *et al.* focused on the electronic properties of the anion and computed the five lowest energy resonances as part of a wider time-dependent DFT (TDDFT) study of charged PAHs.[41]

As discussed in the previous chapter, the calculation of resonances has the added complication that, by definition, there are molecular orbitals that will describe the detachment continuum. Therefore, distinguishing valence orbitals from discretised continuum states is of great importance. In the present study, we use the stabilisation method in conjunction with TDDFT calculations to support the interpretation of the 2D PE spectroscopy of $C_{14}H_{10}{}^-$. While the calculations are not of particularly high accuracy, they do appear to capture the overall electronic structure of the observed resonances. Our work shows that, while there are several low-lying resonances that can lead to the formation of a temporary negative ion, there is only a small amount of ground electronic state recovery suggesting that the lifetimes are very short and that anthracene by itself is not likely to form $C_{14}H_{10}{}^-$ upon low-energy electron impact.

4.2   EXPERIMENTAL & COMPUTATIONAL DETAILS

The experimental setup is described in Chapter 3 and has also been presented in detail elsewhere.[43] As such, only details relevant to the current study are given. Solid anthracene (Sigma Aldrich) was heated at 180°C in an Even-Lavie valve[44] and the resulting molecular vapour was expanded through the pulsed valve into vacuum using Ar as a carrier gas (5 bar). Ionisation of the molecular beam expansion via electron impact formed $C_{14}H_{10}^-$ and its clusters, $(C_{14}H_{10})_n^-$. $C_{14}H_{10}^-$ was then mass-selected and the photoelectrons imaged using the velocity map imaging spectrometer.

To aid the characterisation of anion resonances, DFT and TDDFT were employed at the B3LYP/6-311++G level of theory using Gaussian09.[45–48] There are numerous examples within the literature where the use of B3LYP in conjunction with a Pople basis set in studies of PAH anions has produced optimisation and excitation energies which lie within chemical accuracy (0.3 eV) of their respective experimental values.[39–41,49–51] While polarisation functions enhance the qualitative accuracy of calculations through its improved description of intermolecular bonding, use of 6-311++G** in the computation of anthracene's anion resonances (where $\zeta = 100\%$ of its initial value) yielded little difference in excitation energies. To reduce the computational cost associated with the stabilisation calculations, polarisation functions were not employed in this study.

DFT optimisation calculations and vibrational analysis were performed on the open-shell anthracene anion to obtain its minimum energy structure. Theoretical values for the adiabatic and vertical detachment energies were also obtained. Following this, the lowest 50 excited electronic states of anionic anthracene were computed. In addition to the previously stated level of theory, TDDFT calculations were also performed without diffuse functions, using the 6-311G basis set in conjunction with B3LYP.

The basis set stabilisation method has been employed to discriminate between discretised continuum states (DCSs)[51] and resonance states. This technique was implemented using the 6-311++G basis set, in which diffuse functions are added to both carbon and hydrogen atoms. Both diffuse exponents were scaled between 45 - 100% of their initial values in 5% increments. A TDDFT calculation was performed at each exponent value, in which the first 50 excited states of the anion were computed.

4.3 RESULTS AND ANALYSIS

4.3.1 2D PHOTOELECTRON SPECTRUM

Figure 4.1(a) shows the 2D PE spectrum of $C_{14}H_{10}^-$. The 2D map is composed of 137 PE spectra taken at 25 meV photon energy intervals and have been normalised to the total (integrated) PE signal in each spectrum. The 2D PE spectrum has been smoothed using the bilinear interpolation function featured in MATLAB.[52] In Figure 4.1(b), we have reproduced this data and have annotated this with labels to aid the discussion and analysis of these data.
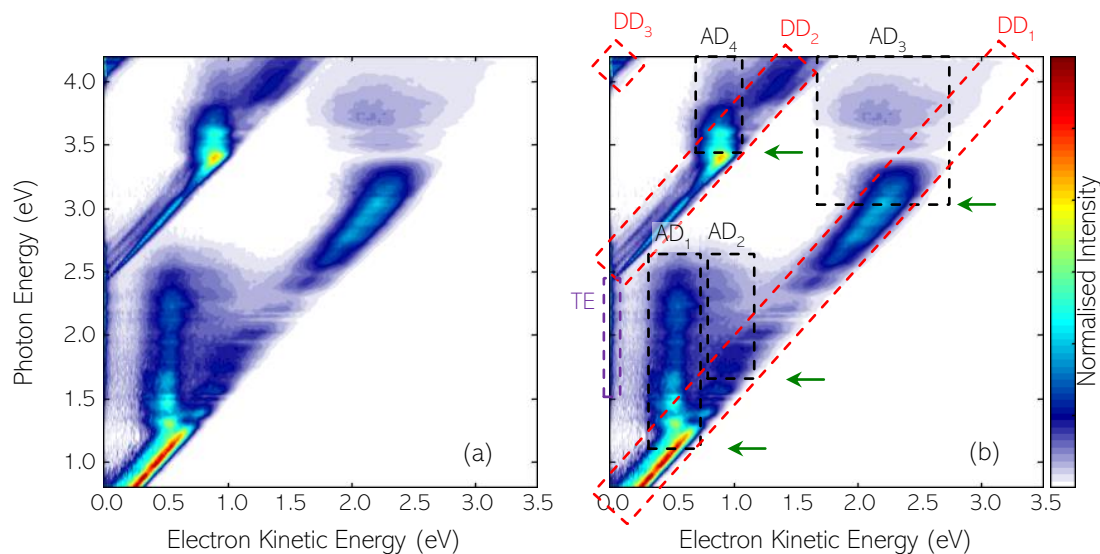

Figure 4.1: **(a)** 2D PE spectrum of $C_{14}H_{10}^-$, normalised to the integrated intensity of each spectrum. **(b)** Annotated version of (a) that includes labels of the various accessible detachment channels: direct detachment (DD), autodetachment (AD), and thermionic emission (TE). Location of resonances derived from the experiment (see text) are shown by green horizontal arrows.

Figure 4.1 contains direct detachment (DD) features, which appear as diagonal features, for which the eKE increases with increasing photon energy ($d(\text{eKE})/d(h\nu) = 1$), as well as indirect autodetachment detachment features (AD), that appear red-shifted relative to the DD features. Three distinct DD features are clearly visible. Extrapolation of these to eKE = 0 eV yields onset energies of 0.53, 2.40, and 4.05 ± 0.02 eV, and we label these direct detachment channels as DD_1, DD_2 and DD_3, respectively.

In addition to the DD channels, a number of AD features can be seen and are highlighted in Figure 4.1(b). The eKE associated with the AD feature appears mostly independent of

photon energy (vertical features in the 2D PE spectrum). To determine the onset at which a given AD channel appears, we have extrapolated these vertical PE features, by eye, to the point where they intersect with the corresponding DD feature. Using this approximate method, the onsets of the AD channels are found to be at photon energies corresponding to $hv \sim 1.1$, 1.6, 2.9 and 3.4 eV for AD_1, AD_2, AD_3, and AD_4, respectively. These estimated onsets have an error of ± 0.1 eV and are indicated by the horizontal arrows in Figure 4.1(b). The inclusion of AD_2 is difficult to appreciate on the 2D PE spectrum and is based on a number of additional considerations as discussed below.
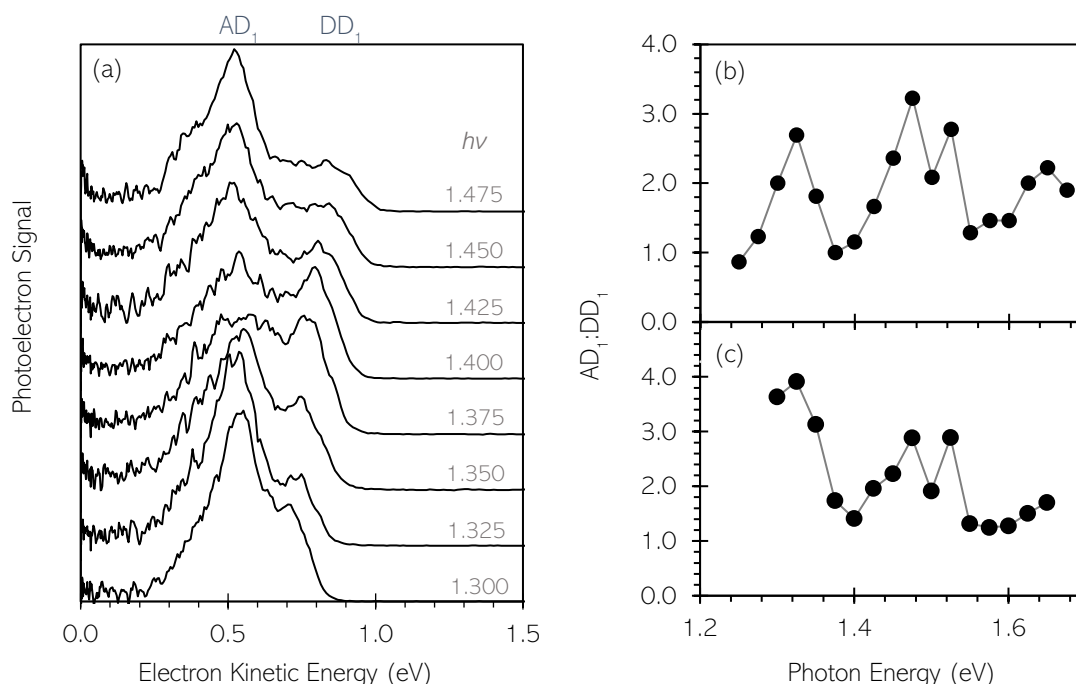

Figure 4.2: **(a)** Photoelectron spectra of anthracene measured between $hv = 1.30$ and 1.45 eV in which the lowest energy direct and indirect detachment features, AD_1 and DD_1 respectively, are present. Ratio of AD_1 and DD_1 intensities are given as a function of photon energy where AD_1:DD_1 has been determined in **(b)** using the peak maxima and in **(c)** using the area underneath Gaussian functions to which the detachment peaks have been fit.

Figure 4.2(a) shows a series of PE spectra taken between $hv = 1.30$ and 1.45 eV that are representative of the region where the AD_1 indirect channel contributes. This clearly shows the red-shift of the AD_1 channel with respect to the corresponding DD_1 channel. However, Figure 4.2(a) shows that the ratio between AD_1 and DD_1 is not constant. For example, at $hv = 1.30$ and 1.45 eV, the ratio of PE signal AD_1:DD_1, is greater than at $hv = 1.38$ eV. Indeed, there is a modulation of the PE signal associated with the AD_1 channel that is out-of-phase with a similar

modulation in the DD_1 channel. To provide a rough analysis of this modulation, the AD_1 and DD_1 signal intensities have been taken as the peak value of each feature. Figure 4.2(b) shows the result of this analysis and clearly shows the out-of-phase oscillation in signal, with a spacing of approximately 175 meV. A more accurate measure of the oscillations in PE signal observed in Figure 4.2(a) can be achieved by fitting the detachment features to line shape functions and measuring the ratio of the area underneath the resulting curves. However, this method is not without complication as it is difficult to ascertain the most appropriate function to employ (*e.g.* Gaussian or Lorentzian) and the appropriate number of functions per detachment feature to use. Nevertheless, a crude fit has been obtained by fitting a single gaussian function to either detachment feature (AD_1 and DD_1) contained within the PE spectra between $hv = 1.3$ and 1.6 eV (Figure 4.2(c)). Though this method produces a difference in magnitude, the qualitative trend in the out-of-phase oscillations observed in Figure 4.2(b) is clearly reproduced. Evidence of similar oscillations are also seen in AD_3 and AD_4, but these are less obvious and we refrain from analysing these channels in a similar manner.

4.3.2 COMPUTATIONAL

TDDFT calculations computing the lowest 50 excited states of the anion as a function of basis set diffuseness give rise to the stabilisation plot shown in Figure 4.3(a). Most excited states are observed to vary in transition energy as the basis set exponent (diffuseness) changes. The states that rapidly change in energy as a function of diffuseness are associated with DCSs, as reflected by the fact that as the effective "box" size is described with increasing diffuseness, the energy levels of the free electron decrease approximately quadratically. Conversely, regions of invariance between the excitation energy and basis set diffuseness exist within the stabilisation plot and are indicated by blue arrows in Figure 4.3(a). These regions give the energetic locations of the lowest lying anion resonances of anthracene. As discussed in Chapter 3.6, the energies of the resonances can be determined from a series of avoid crossings between the resonance and continuum states, in which the DCS takes on the character of a real resonance. For a given resonance, the crossings are independent of basis set variation and occur at the same excitation energy, which can be obtained by eye from the Figure 4.3. A number of avoided crossings are present in the energetically stabilised regions of the plot but are not easily identifiable from Figure 4.3(a). As such, the stabilisation plot has been reproduced in Figure 4.3(b) across a narrower excitation energy range which encompasses the stabilised regions. In

the range where the energy does not change significantly, the DCS has taken on the character of a real resonance and remains so until it undergoes an avoided crossing with another DCS, at which point the resonance will take on the character of that DCS. Despite the series of (avoided) crossings between the states, there are distinct regions over which a state can be identified at a given excitation energy. From Figure 4.3(b), we can clearly distinguish three states corresponding to resonances.
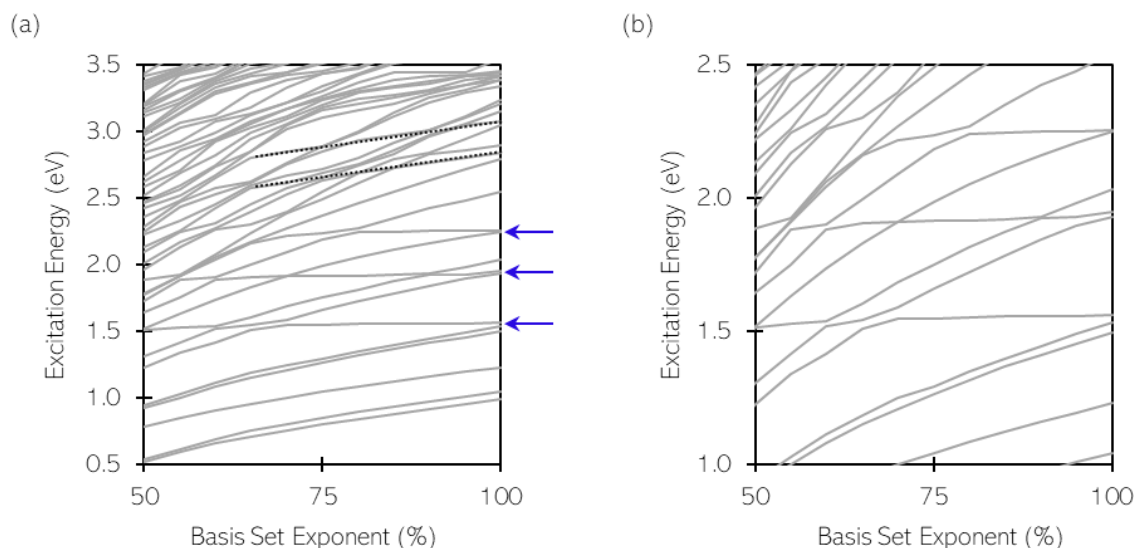

Figure 4.3: **(a)** Stabilisation plot of $C_{14}H_{10}^-$, in which the energies of the lowest 50 excited states have been presented as a function of varying basis set diffuseness. Blue arrows indicate the positions of anion resonances. Dotted lines indicate higher lying resonances. Magnification of the lower lying stabilised regions is presented in **(b)**.

Further characterisation of these resonances has been included in Figure 4.4, where the qualitative nature of the five lowest lying resonances has been determined. For each excited state, the relevant molecular orbitals (MOs) are shown alongside their respective symmetries in Figure 4.4(a). Symmetry labels are derived assuming that anthracene lies in the *y-z* plane with the *z*-axis being the long molecular axis. The MOs were computed using a 6-311G basis set. This is effectively the upper limit of the TDDFT calculations in which the exponent reaches infinity and there are no diffuse functions present. The electronic configurations of the examined resonance states have been presented in Figure 4.4(b), with the symmetry of the state and its computed oscillator strength also stated.
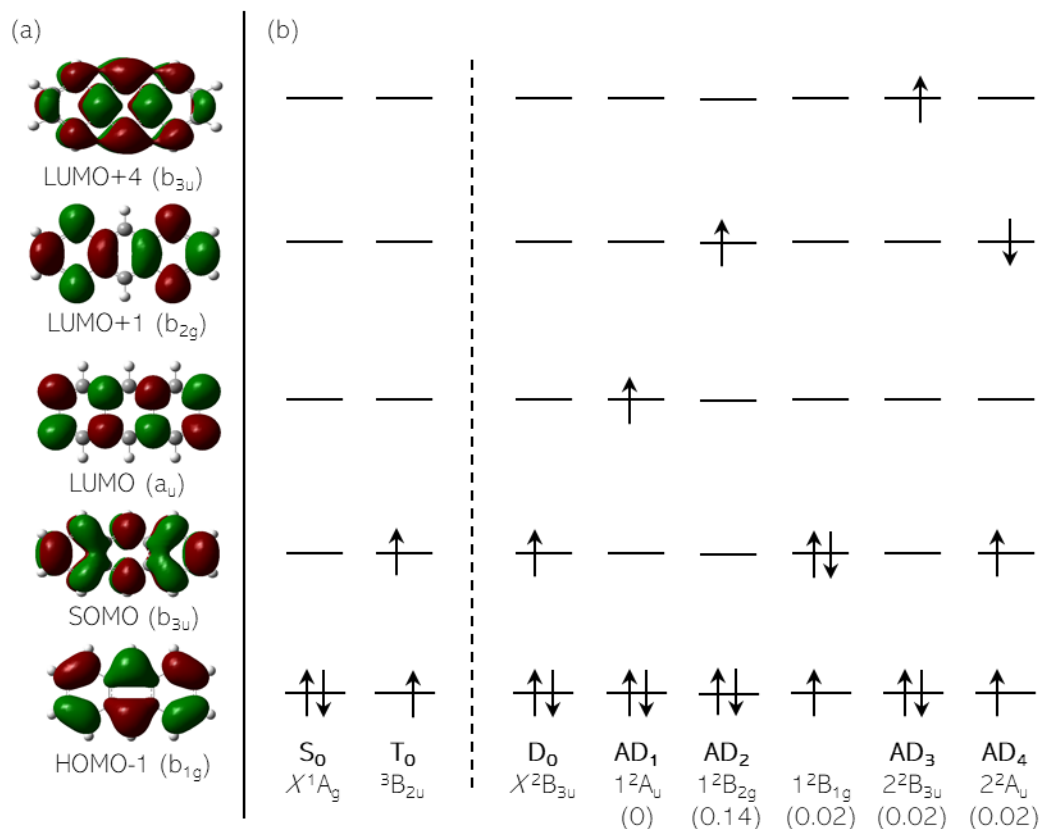
Figure 4.4: (a) Molecular orbitals of the lowest lying neutral and anionic electronic states of anthracene. **(b)** The electronic configurations of these states are shown with their symmetries and computed oscillator strengths in brackets.

Qualitative analysis of the ground state configurations of the anionic and neutral species is provided in Figure 4.4. The ground state of $C_{14}H_{10}{}^-$ has D_{2h} symmetry with an electronic configuration of $(C_{14}H_{10})_n{}^-$ of $\ldots\pi(b_{1g})^2\pi(b_{3u})^1$ corresponding to a ground $X\,^2B_{3u}$ state. The two lowest energy neutral states are included. Loss of the electron in the singly occupied MO (SOMO) of b_{3u} symmetry leads to the neutral ground $X\,^1A_g$ state. The lowest triplet state of the neutral arises from a $\ldots\pi(b_{1g})^1\pi(b_{3u})^1$ configuration leading to a $^3B_{2u}$ state.

The lowest energy resonance, 1^2A_u, corresponds to the excitation of an electron in the SOMO (b_{3u}) to the lowest unoccupied MO (LUMO) (a_u) and has a calculated oscillator strength of zero (symmetry forbidden). This is followed by two close-lying resonances, 1^2B_{2g} and 1^2B_{1g}, that correspond to the transitions LUMO+1 $\leftarrow$ SOMO and SOMO $\leftarrow$ HOMO–1, respectively. The $1^2B_{2g} \leftarrow X\,^2B_{3u}$ transition has the largest oscillator strength. At higher energy, resonances are more difficult to distinguish from the stabilisation plot due to a much higher density of DCSs. Nevertheless, we can identify regions in Figure 4.3(a) (denoted by dotted lines) that are

59

relatively constant in energy. That is, although these states do vary in energy, these changes are less significant in comparison the variations observed for DCSs. Therefore, we tentatively attribute the dotted lines to resonance states, which correspond to the higher energy transitions shown in Figure 4.4 that access the 2^2B_{3u} and 2^2A_u states. Greater certainty in the characterisation of the two higher energy states represented by dotted lines could be achieved through an extrapolation of the stabilisation plot to higher basis set exponent values, *i.e.* towards infinity.

Table 4.1: Computed excitation energies of the lowest lying resonance states of $C_{14}H_{10}^-$, with oscillator strengths in brackets. Mean absolute error values have been calculated through comparison to the approximate energies obtained from our 2D PE spectrum. Energy and error values are stated in eV.

State	TDDFT	Exp.	Error
1^2A_u	1.62 (0)	~1.1	0.52
1^2B_{2g}	2.06 (0.14)	~1.6	0.46
1^2B_{1g}	2.29 (0.02)	-	-
2^2B_{3u}	2.96 (0.02)	~2.9	0.06
2^2A_u	3.52 (0.02)	~3.4	0.12

The excitation energies of the five lowest lying resonance states are given in Table 4.1, where they are compared to experimental values. In a similar fashion to the MOs, the computed energies stated have been obtained using the 6-311G basis set as opposed to that used in the stabilisation calculations. Although calculations employing diffuse functions generally

increase the quantitative accuracy of the computed transition energies, they introduce a higher amount of qualitative inaccuracy through the increased inclusion of DCSs. This problem is excerabated at higher energies due to an increased density of DCSs and thus, complicates the computation of higher lying resonance states and increases its computational expense. Therefore, we have identified the energetic locations of the lowest lying resonances from the stabilisation plot and have cross-referenced these energies and MO transitions with that obtained from the 6-311G calculations.

4.4   DISCUSSION

4.4.1   ASSIGNMENT OF DIRECT DETACHMENT CHANNELS

The adiabatic detachment energies (ADEs) of the $X\ ^2B_{3u} + h\nu \rightarrow X\ ^1A_g + e^-$ and $X\ ^2B_{3u} + h\nu \rightarrow\ ^3B_{2u} + e^-$ channels have been determined to high accuracy by Garand and co-workers using high-resolution slow photoelectron velocity-map imaging (SEVI) measurements and have values of 0.532(3) eV and 2.404(3) eV, respectively.[27] These values are in agreement with the onset of the DD_1 channel at 0.53 eV and the DD_2 channel at 2.40 eV. Hence, DD_1 and DD_2 are assigned as direct detachment channels to the singlet and triplet ground states of the neutral, respectively. Channel DD_3 corresponds to the excitation of the neutral to its first singlet state in the photodetachment, $X\ ^2B_{3u} + h\nu \rightarrow\ ^1B_{2u} + e^-$. This assignment is in agreement with the gas-phase absorption spectrum of neutral anthracene, which has its 0-0 transition of the $^1B_{2u} \leftarrow X\ ^1A_g$ band at 3.422 eV. Based on this, the DD_3 channel is expected to appear at $h\nu = 3.954$ eV in the present experiment, in reasonable agreement with our measurement of 4.05 eV.

The DD_1 and DD_2 channels show vibrational structure in the 1D photoelectron spectra, which corresponds to the vibrational modes of the ground electronic state of the neutral and its first triplet excited state, respectively. The vibrations of the neutral have been discussed in detail by Garand and coworkers,[27] whose experiment is of much higher resolution than ours, and so we will not discuss these further.

4.4.2   ASSIGNMENT OF RESONANCES

There are several accessible resonances in the spectral range probed here, but there are no bound excited states of $C_{14}H_{10}^-$. From the experiment, we estimate the location of the two

lowest-lying resonances to be at approximately $hv = 1.1$ eV and 1.6 eV (see Figure 4.1(b) and Table 4.1). The first of these is clearly identifiable (AD$_1$), while the second (AD$_2$) requires a little consideration.

Shida and Iwata have measured an absorption spectrum of $C_{14}H_{10}^-$ in a methyl-tetrahydrofuran matrix at 77 K,[23] which is reproduced here in Figure 4.5. This shows a weak transition around $hv \sim 1.3$ eV with a series of vibrational peaks separated by ~150 meV. A second, brighter excited state was observed at $hv = 1.67$ eV. Beyond this, there are a series of vibrational peaks and possibly a third absorption band, but the absorption spectrum is too congested to be certain of this. Unfortunately, as the absorption spectrum was only collected for $hv > 1.25$ eV, the 0-0 transition of this band may be at lower energy, which would be consistent with the onset of AD$_1$ channel at ~1.1 eV. The second brighter transition at 1.67 eV is not very clear in the 2D PE spectrum, but there is evidence that changes in the resonance dynamics are occurring. Firstly, there is some evidence that new autodetachment signal is appearing starting from around $hv = 1.6$ eV. As this signal remains constant in kinetic energy, it is clear that the relative contribution of the direct channel (DD$_1$) is becoming less pronounced beyond $hv \sim 2$ eV. Secondly, a new indirect channel at very low energy switches on for photon energies above $hv = 1.6$ eV, suggesting a new resonance is contributing. The observed low energy electrons are indicative of thermionic emission and are labelled as TE in Figure 4.1b. The expectation of two resonances is also in agreement with the electron transmission spectra from Burrow et al. and with their calculations as well as ours.[28]
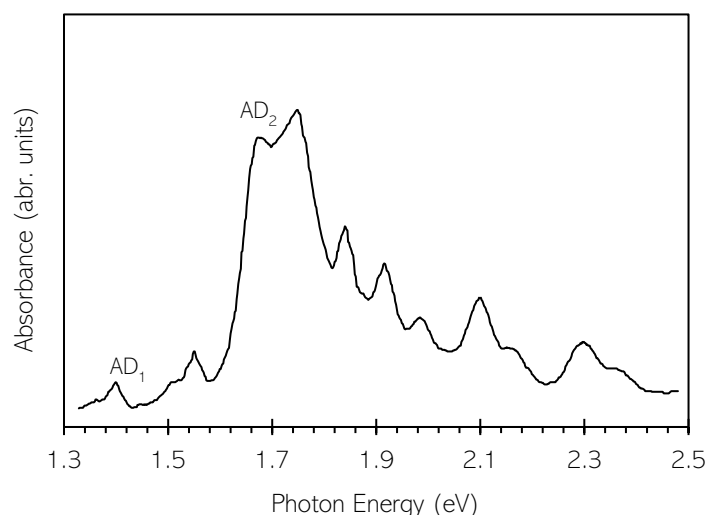

Figure 4.5: Absorption spectrum of $C_{14}H_{10}^-$ in a methyl-tetrahydrofuran matrix at 77 K, which has been reproduced from Ref [23]. Absorption bands have been labelled with respect to the autodetachment (AD) features identified in the 2D PE spectrum, where AD$_1$ and AD$_2$ correspond to transitions to the 1^2A_u and 1^2B_{2g} states of the anion, respectively.

The overall picture from both the absorption spectrum and our 2D PE spectrum appears to be supported qualitatively by our calculations. The lowest resonance is calculated at $hv = 1.62$ eV with no oscillator strength followed by a bright resonance at $hv = 2.06$ eV and a third resonance at $hv = 2.29$ eV. The energy gaps from the 2D PE spectrum and the relative absorbances from the absorption spectra (weak, low energy peak followed by bright, higher energy band) suggest that the order of the calculated resonances is correct. The TDDFT calculations are overestimating the transition energies by some way (about 0.5 eV), which is not wholly surprising given the level of our calculations. Based on the qualitative agreement and previous experimental and theoretical work, the first resonance leading to AD_1 can be assigned as the $1^2A_u \leftarrow X\,^2B_{3u}$ transition while the second that can be correlated with AD_2 can be assigned to $1^2B_{2g} \leftarrow X\,^2B_{3u}$ transition. Both these resonances are of shape character and may be expected to lead to efficient and very fast autodetachment. The discrepancy between the observed and computed oscillator strength of 0 for the $1^2B_{2g} \leftarrow X\,^2B_{3u}$ transition could arise from Herzberg-Teller coupling that has not been accounted for in the calculation.[53] Herzberg-Teller coupling describes the intensity borrowing observed for vibronic transitions that occur with some intensity when they should be forbidden based on symmetry arguments. Under the Franck-Condon approximation, the transition dipole moment associated with an electronic transition (which determines the oscillator strength) is assumed to be independent of the vibrational nuclear co-ordinate. Herzberg-Teller coupling takes into account this nuclear dependence by considering structural changes upon excitation, which alters the transition dipole moment and ultimately shifts the oscillator strength to higher values.[53–55]

A third resonance was calculated at $hv = 2.29$ eV corresponds to a $1^2B_{1g} \leftarrow X\,^2B_{3u}$ transition. This resonance remains unlabelled with the AD nomenclature in Figure 4.3 as evidence of this state was not observed in the 2D PE spectrum. The third resonance is of Feshbach character with respect to the $X\,^1A_g$ neutral ground state. Hence, the lifetime of this resonance with respect to electron loss may be expected to be longer. Limited support for the third resonance can be found in the absorption spectra of Shida and Iwata, where a possible third absorption band can be distinguished at $hv \sim 2.1$ eV (Figure 4.5).

The two higher lying resonances identified in Figure 4.3(a) correspond to the $2^2B_{3u} \leftarrow X\,^2B_{3u}$ and $2^2A_u \leftarrow X\,^2B_{3u}$ transitions. The 2^2B_{3u} is a shape resonance while the 2^2A_u is of Feshbach character. However, loss of an electron from the b_{2g} orbital from the 2^2A_u resonance forms the neutral triplet $^3B_{2u}$ state. Based on this observation and a strong correlation between the computed and experimental excitation energies (see Table 4.1), the 2^2B_{3u} and 2^2A_u states

are assigned to autodetachment pathways of the ground neutral state (AD_3) and the lowest neutral triplet neutral state (AD_4), respectively.

4.4.3 COMPETITION BETWEEN DIRECT DETACHMENT AND RESONANCE EXCITATION

Figure 4.2 shows a modulation of the ratio of PE signal in the AD_1 vs DD_1 channels. Because the 2D PE spectral intensity has been normalised relative to the integrated intensity of each spectrum, the modulation seen in Figure 4.2 is a relative rather than an absolute measure. The absorption spectrum of $C_{14}H_{10}^-$ measured by Shida and Iwata (Figure 4.5) shows the absorption band of the weak $1^2A_u \leftarrow X\,^2B_{3u}$ transition. While the origin (0-0 transition) of the band was probably not measured, a vibrational progression with a spacing of ~150 meV was observed. The oscillation in Figure 4.2(b) has a similar spacing (approximately 175 meV) suggesting that the same vibrational progression in the 1^2A_u resonance is responsible for the observed oscillation. The observed oscillation can then be explained by an increase in cross section for excitation of the 1^2A_u state when it is resonant with specific vibrations, *i.e.* it follows the absorption spectrum (see Figure 4.6). This leads to enhancement in AD_1 on top of a constant (or at least smoothly varying) background associated with the DD_1 channel. Oscillations in the AD:DD ratio are also seen for the higher lying resonances (AD_3 and AD_4) but these have been less well resolved but are likely arising from a similar process.
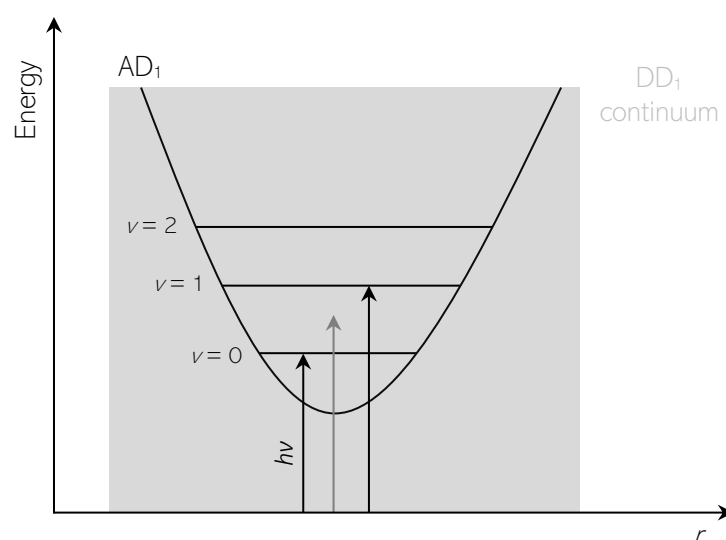

Figure 4.6: Particular values of $h\nu$ are resonant with the vibrational levels of the 1^2A_u resonance labelled AD_1. However, direct detachment to the neutral continuum (DD_1 continuum) remains an available decay pathway and is accessible for non-resonant excitations (represented by the grey arrow).

4.4.4 SPECTRAL SHAPE OF AUTODETACHMENT SPECTRA

A particularly striking feature of AD_1 is its rather narrow spectral shape, *i.e.* it is of a similar spectral width to DD_1. This point is highlighted in Figure 4.2(a) and is further evidenced quantitatively by comparison of the AD_1 and DD_1 spectral widths which have been determined from a Gaussian fit of the PE spectrum at $hv = 2.3$ eV, where the full-width half-maximum (FWHM) = 0.35 and 0.43 eV, respectively. The feature AD_1 is associated with autodetachment from the 1^2A_u resonance and it is apparent as soon as this channel becomes accessible. As the 1^2A_u resonance is of shape character, autodetachment may be expected to be very fast – typically on the order of a few femtoseconds, which is consistent with the estimated lifetime obtained (2.19 fs) from the Gaussian fit of the spectral features at $hv = 2.3$ eV. As such, the nuclear dynamics on the 1^2A_u surface may be limited and one might intuitively expect that the emission is predominantly dictated by the vertical Franck-Condon factors of the $1^2A_u \rightarrow X\,^1A_g$ + e^- channel. A similar argument has been made by Bochenkova *et al.* in the analysis of the autodetachment from resonances in the green fluorescent protein chromophore anion.[56] The relatively narrow distribution then suggests that the 1^2A_u potential energy surface is quite similar to that of the $X\,^1A_g$ final state of the neutral. By inspection of the MOs involved (Figure 4.4), AD_1 corresponds to loss of an electron from the LUMO, which is antibonding only along the short axis of the molecule and non-bonding along the long axis. Hence, it is not unreasonable to suggest that the geometric difference between 1^2A_u and $X\,^1A_g$ could be relatively small. High-level calculations on the excited state surface could verify this, but this is beyond the scope of the present study. The fact that the AD_1 feature does not change much with hv suggests that the additional energy imparted in the 1^2A_u resonance upon excitation is conserved in the $X\,^1A_g$ final state, leading to a constant eKE of the AD_1 channel.

It is quite striking though that the AD_1 channel persists even when the brighter 1^2B_{2g} resonance is excited at $hv > 1.6$ eV. While there is additional AD signal, as exemplified by region AD_2 in Figure 4.1(b), the predominant signal remains in AD_1. Note that the 1^2B_{2g} and 1^2A_u resonances are close in energy and there may be population transfer between them, despite the fast autodetachment, which is further discussed below.

Not all the AD features are narrow. For example, AD_3 which we assigned to the 2^2B_{3u} resonance is very broad. This could reflect very fast autodetachment from an excited state that has a very different geometry leading to a broad range of Franck-Condon factors, or slower dynamics in which nuclear dynamics can take place on the excited state and autodetachment

can occur over a range of different geometries. Because this resonance is at high energy, the final orbital to which the SOMO electron is excited is of greater antibonding character so the difference in geometry between this resonance and the $X\,^1A_g$ ground state will likely be greater, which is consistent with the broader spectral width of AD_3. Alternatively, the spectral shape of AD_3 could be attributed to lifetime broadening given the shape character of this resonance and its consequentially short lifetime. Based on the PE spectra at $hv = 3.5$ eV, the spectral width (FWHM) was measured as 0.68 eV, which corresponds to an approximate lifetime of 6.09 fs. However, this estimation assumes that the spectral width is controlled solely by lifetime broadening, which it is not as the Franck-Condon envelope will also play a deterministic role. However, it is not possible to deconvolute these two factors.

The above arguments are predominantly based on experimental arguments that are supported qualitatively by the calculations. We have specifically refrained from performing higher-level calculations to demonstrate the synergy between the experiment and TDDFT and the insight these offer without needing to resort to such methods.

4.4.5 RESONANCE DYNAMICS

In the preceding section, we discussed that AD_1 arises from the $1\,^2A_u$ shape resonance that leads to a narrow autodetachment peak. However, according to the absorption spectrum of Shida and Iwata, the $1\,^2A_u$ resonance has a significantly lower transition probability than the $1\,^2B_{2g}$ resonance. Nevertheless, the dominant PE signal appears in the AD_1 channel as shown in Figure 4.1. Specifically, while the feature AD_2 clearly shows that some autodetachment is arising from higher lying resonances, the yield of electrons is significantly lower than AD_1. There are two possible explanations that would be consistent with these observations. Firstly, the $1\,^2B_{2g}$ (and perhaps $1\,^2B_{1g}$) resonance undergoes a non-adiabatic transition to form the $1\,^2A_u$ state. Such ultrafast internal conversion processes have previously been observed in anion resonances and are likely to be especially efficient when the potential energy surfaces involved are energetically close at the excitation Franck-Condon geometry so that only small nuclear displacements are required to lead to a conical intersection. In such a case, even though $1\,^2B_{2g}$ is initially excited, $1\,^2A_u$ is formed with some excess vibrational energy but given that the potential energy surfaces of $1\,^2A_u$ and $X\,^1A_g$ are similar, the AD_1 feature will remain narrow. A second scenario to explain why the AD_1 yield is higher than AD_2 could be that AD_2 can internally convert to the ground electronic state of the anion ($X\,^2B_{3u}$). In this case, no

autodetachment would be seen from AD_2. Instead, the $X\ ^2B_{3u}$ state is formed with a large amount of internal energy and the excess electron can subsequently be emitted statistically by thermionic emission (TE). The signature of TE is PE signal at very low kinetic energy (peaking at 0 eV) and with an exponentially decaying spectral profile. Indeed, inspection of Figure 4.1 shows a small TE feature that turns on at ~ 1.6 eV, which is consistent with the resonance energy of 1^2B_{2g} determined by extrapolation of the AD_2 feature. Hence, the TE peak does indeed appear to correlate with the production of 1^2B_{2g} indicating that at least a fraction of the population can reform the $X\ ^2B_{3u}$ ground state of the anion.

To determine the exact dynamics would require time-resolved PE spectroscopic studies. We have attempted such studies for the current system at a range of different pump and probe photon energies, but these have been unsuccessful. Apparently, the cross sections for photodetachment from the resonances are very low.

4.5 SUMMARY AND CONCLUSION

In summary, the 2D photoelectron spectrum of the radical ion, $C_{14}H_{10}^-$ has been presented between $hv = 0.8$ and 4.2 eV. A number of prominent spectral features give an insight into the possible decay pathways of the anion and thus, permits the characterisation of the anion's detachment properties. ADE values of the neutral species in its singlet and triplet spin states were determined through measurement of the lowest lying direct detachment channels. Indirect detachment features reveal the presence of a number of resonances, which have been characterised with the aid of computational methods. Basis set stabilisation calculations identified the two lowest lying resonances which are of shape character and correspond to experimental autodetachment features at ~ 1.1 and 1.6 eV. Using this method, higher lying resonances have been also been characterised, however their assignments are tentative due to a higher density of continuum states. In contrast to the literature and calculated values, the measured intensity of autodetachment from the 1^2A_u resonance was markedly higher than that of the 1^2B_{2g} resonance. This observation could be attributed to internal conversion from 1^2B_{2g} to form the vibrationally hot 1^2A_u state, from which autodetachment can occur and/or internal conversion of the 1^2B_{2g} resonance to form the ground electronic state. Hence, while there is some evidence for the reformation of $C_{14}H_{10}^-$ from electron impact resonances, this is quite small compared to fast autodetachment and suggests that anthracene is not very efficient at capturing slow electrons in the interstellar medium as an isolated molecule.

4.6 REFERENCES

(1)   Rescifina, A.; Chiacchio, M. A.; Corsaro, A.; De Clercq, E.; Iannazzo, D.; Mastino, A.; Piperno, A.; Romeo, G.; Romeo, R.; Valveri, V. Synthesis and Biological Activity of Isoxazolidinyl Polycyclic Aromatic Hydrocarbons: Potential DNA Intercalators. *J. Med. Chem.* **2006**, *49* (2), 709–715.

(2)   Becker, F. F.; Banik, B. K. Polycyclic Aromatic Compounds as Anticancer Agents: Synthesis and Biological Evaluation of Methoxy Dibenzofluorene Derivatives. *Front. Chem.* **2014**, *2*.

(3)   Finlayson-Pitts, B. J.; Pitts, J. N. Tropospheric Air Pollution: Ozone, Airborne Toxics, Polycyclic Aromatic Hydrocarbons, and Particles. *Science* **1997**, *276* (5315), 1045–1051.

(4)   Huang, J.; Su, J.-H.; Tian, H. The Development of Anthracene Derivatives for Organic Light-Emitting Diodes. *J. Mater. Chem.* **2012**, *22* (22), 10977–10989.

(5)   Kitamura, M.; Imada, T.; Arakawa, Y. Organic Light-Emitting Diodes Driven by Pentacene-Based Thin-Film Transistors. *Appl. Phys. Lett.* **2003**, *83* (16), 3410–3412.

(6)   Casanova, D. Electronic Structure Study of Singlet Fission in Tetracene Derivatives. *J. Chem. Theory Comput.* **2014**, *10* (1), 324–334.

(7)   Zeng, T.; Hoffmann, R.; Ananth, N. The Low-Lying Electronic States of Pentacene and Their Roles in Singlet Fission. *J. Am. Chem. Soc.* **2014**, *136* (15), 5755–5764.

(8)   Zirzlmeier, J.; Lehnherr, D.; Coto, P. B.; Chernick, E. T.; Casillas, R.; Basel, B. S.; Thoss, M.; Tykwinski, R. R.; Guldi, D. M. Singlet Fission in Pentacene Dimers. *Proc. Natl. Acad. Sci.* **2015**, *112* (17), 5325–5330.

(9)   Zimmerman, P. M.; Bell, F.; Casanova, D.; Head-Gordon, M. Mechanism for Singlet Fission in Pentacene and Tetracene: From Single Exciton to Two Triplets. *J. Am. Chem. Soc.* **2011**, *133* (49), 19944–19952.

(10)   Tielens, A. G. G. M. Interstellar Polycyclic Aromatic Hydrocarbon Molecules. *Annu. Rev. Astron. Astrophys.* **2008**, *46* (1), 289–337.

(11)   Verstraete, L. The Role of PAHs in the Physics of the Interstellar Medium. *EAS PublSer* **2011**, *46*, 415–426.

(12)   Salama, F.; Bakes, E. L. O.; Allamandola, L. J.; Tielens, A. G. G. M. Assessment of the Polycyclic Aromatic Hydrocarbon-Diffuse Interstellar Band Proposal. *Astrophys. J.* **1996**, *458* (2 PART I), 621–636.

(13)   Geballe, T. R. The Diffuse Interstellar Bands - a Brief Review. *J. Phys. Conf. Ser.* **2016**, *728*, 062005.

(14)   van der Zwet, G. P.; Allamandola, L. J. Polycyclic Aromatic Hydrocarbons and the Diffuse Interstellar Bands. In *Light on Dark Matter*; Israel, F. P., Ed.; Astrophysics and Space Science Library; Springer Netherlands, **1986**; pp 233–236.

(15)   Omont, A.; Bettinger, H. F.; Tönshoff, C. Polyacenes and Diffuse Interstellar Bands. *Astron. Astrophys.* **2019**, *625*, A41.

(16)   Steglich, M.; Bouwman, J.; Huisken, F.; Henning, T. Can Neutral and Ionized Polycyclic Aromatic Hydrocarbons Be Carriers of the Ultraviolet Extinction Bump and the Diffuse Interstellar Bands? *Astrophys. J.* **2011**, *742* (1), 2.

(17)   Snow, T. P.; Le Page, V.; Keheyan, Y.; Bierbaum, V. M. The Interstellar Chemistry of PAH Cations. *Nature* **1998**, *391* (6664), 259–260.

(18)   Campbell, E. K.; Holz, M.; Gerlich, D.; Maier, J. P. Laboratory Confirmation of C_{60}^+ as the Carrier of Two Diffuse Interstellar Bands. *Nature* **2015**, *523* (7560), 322–323.

(19)   Gudipati, M. S.; Yang, R. In-Situ Probing of Radiation-Induced Processing of Organics in Astrophysical Ice Analogs - Novel Laser Desorption Laser Ionization Time-of-Flight Mass Spectroscopic Studies. *Astrophys. J.* **2012**, *756* (1), L24.

(20)   Lepp, S.; Dalgarno, A. Heating of Interstellar Gas by Large Molecules or Small Grains. *Astrophys. J.* **1988**, *335*, 769–773.

(21)   Carelli, F.; Gianturco, F. A. Polycyclic Aromatic Hydrocarbon Negative Ions in Interstellar Clouds: A Quantum Study on Coronene Metastable Anions. *Mon. Not. R. Astron. Soc.* **2012**, *422* (4), 3643–3648.

(22)   Rienstra-Kiracofe, J. C.; Barden, C. J.; Brown, S. T.; Schaefer, H. F. Electron Affinities of Polycyclic Aromatic Hydrocarbons. *J. Phys. Chem. A* **2001**, *105* (3), 524–528.

(23)   Shida, T.; Iwata, S. Absorption Spectra of Dianthracene Anion Radical and Anthracene Dimer Anion. *J. Chem. Phys.* **1972**, *56* (6), 2858–2864.

(24)   Shida, T.; Iwata, S. Electronic-Spectra of Ion Radicals and Their Molecular-Orbital Interpretation .3. Aromatic-Hydrocarbons. *J. Am. Chem. Soc.* **1973**, *95* (11), 3473–3483.

(25)   Schiedt, J.; Weinkauf, R. Photodetachment Photoelectron Spectroscopy of Mass Selected Anions: Anthracene and the Anthracene-H_2O Cluster. *Chem. Phys. Lett.* **1997**, *266* (1), 201–205.

(26) Song, J. K.; Lee, N. K.; Kim, J. H.; Han, S. Y.; Kim, S. K. Anion Clusters of Anthracene, An$_n^-$ (n=1–16). *J. Chem. Phys.* **2003**, *119* (6), 3071–3077.

(27) Kregel, S. J.; Thurston, G. K.; Garand, E. Photoelectron Spectroscopy of Anthracene and Fluoranthene Radical Anions. *J. Chem. Phys.* **2018**, *148* (23), 234306.

(28) Jordan, K. D.; Burrow, P. D. Temporary Anion States of Polyatomic Hydrocarbons. *Chem. Rev.* **1987**, *87* (3), 557–588.

(29) West, C. W.; Bull, J. N.; Antonkov, E.; Verlet, J. R. R. Anion Resonances of Para-Benzoquinone Probed by Frequency-Resolved Photoelectron Imaging. *J. Phys. Chem. A* **2014**, *118* (48), 11346–11354.

(30) Reddish, T.; Currell, F.; Comer, J. Studies of the 2 eV Shape Resonance in N$_2$ using a Two-Dimensional Scanning Technique. *J. Phys. [E]* **1988**, *21* (2), 203–207.

(31) Regeta, K.; Allan, M. Autodetachment Dynamics of Acrylonitrile Anion Revealed by Two-Dimensional Electron Impact Spectra. *Phys. Rev. Lett.* **2013**, *110* (20), 203201.

(32) Carelli, F.; Gianturco, F. A.; Satta, M.; Sebastianelli, F. Attaching Electrons to a 3-Ring Acene: Structures and Dynamics of Anions in Gas-Phase Anthracene. *Int. J. Mass Spectrom.* **2014**, *365–366*, 377–383.

(33) Sanz, A. G.; Fuss, M. C.; Blanco, F.; Carelli, F.; Sebastianelli, F.; Gianturco, F. A.; García, G. Electron Scattering Cross Sections from Anthracene over a Broad Energy Range (0.00001–10,000 eV). *Appl. Radiat. Isot.* **2014**, *83*, 68–76.

(34) Man, K. F.; Trajmar, S.; McConkey, J. W.; Ratliff, J. M.; Khakoo, M. Excitation of Anthracene (C$_{14}$H$_{10}$) by Electron Impact. *J. Phys. B At. Mol. Opt. Phys.* **1992**, *25* (23), 5245–5256.

(35) Tobita, S.; Meinke, M.; Illenberger, E.; Christophorou, L. G.; Baumgärtel, H.; Leach, S. Polycyclic Aromatic Hydrocarbons: Negative Ion Formation Following Low Energy (0–15 eV) Electron Impact. *Chem. Phys.* **1992**, *161* (3), 501–508.

(36) Gallup, G. A. Stable Negative Ions and Shape Resonances in a Series of Organic Molecules. *J. Chem. Phys.* **2013**, *139* (10), 104308.

(37) Khatymov, R. V.; Muftakhov, M. V.; Shchukin, P. V. Negative Ions, Molecular Electron Affinity and Orbital Structure of Cata-Condensed Polycyclic Aromatic Hydrocarbons. *Rapid Commun. Mass Spectrom.* **2017**, *31* (20), 1729–1741.

(38) Khatymov, R. V.; Tuktarov, R. F.; Muftakhov, M. V. Lifetime of Negative Molecular Ions of Tetracene and Pentacene with Respect to the Autodetachment of an Electron. *JETP Lett.* **2011**, *93* (8), 437–441.

(39)   Dessent, C. E. H. A Density Functional Theory Study of the Anthracene Anion. *Chem. Phys. Lett.* **2000**, *330* (1), 180–187.

(40)   Malloci, G.; Mulas, G.; Cappellini, G.; Fiorentini, V.; Porceddu, I. Theoretical Electron Affinities of PAHs and Electronic Absorption Spectra of Their Mono-Anions. *Astron. Astrophys.* **2005**, *432* (2), 585–594.

(41)   Malloci, G.; Mulas, G.; Cappellini, G.; Joblin, C. Time-Dependent Density Functional Study of the Electronic Spectra of Oligoacenes in the Charge States-1, 0,+1, and +2. *Chem. Phys.* **2007**, *340* (1–3), 43–58.

(42)   Kim, M.-C.; Sim, E.; Burke, K. Communication: Avoiding Unbound Anions in Density Functional Calculations. *J. Chem. Phys.* **2011**, *134* (17), 171103.

(43)   Rogers, J. P.; Anstöter, C. S.; Bull, J. N.; Curchod, B. F. E.; Verlet, J. R. R. Photoelectron Spectroscopy of the Hexafluorobenzene Cluster Anions: $(C_6F_6)_n^-$ (n = 1–5) and $I^-(C_6F_6)$. *J. Phys. Chem. A* **2019**, *123* (8), 1602–1612.

(44)   Even, U.; Jortner, J.; Noy, D.; Lavie, N.; Cossart-Magos, C. Cooling of Large Molecules below 1 K and He Clusters Formation. *J. Chem. Phys.* **2000**, *112* (18), 8068–8071.

(45)   Becke, A. D. Density-functional Thermochemistry. III. The Role of Exact Exchange. *J. Chem. Phys.* **1993**, *98* (7), 5648–5652.

(46)   McLean, A. D.; Chandler, G. S. Contracted Gaussian Basis Sets for Molecular Calculations. I. Second Row Atoms, Z=11–18. *J. Chem. Phys.* **1980**, *72* (10), 5639–5648.

(47)   Krishnan, R.; Binkley, J. S.; Seeger, R.; Pople, J. A. Self-consistent Molecular Orbital Methods. XX. A Basis Set for Correlated Wave Functions. *J. Chem. Phys.* **1980**, *72* (1), 650–654.

(48)   Frisch, M.; Trucks, G.; Schlegel, H.; Scuseria, G.; Robb, M.; Cheeseman, J.; Scalmani, G.; Barone, V.; Mennucci, B.; Petersson, G.; Nakatsuji, H.; Caricato, M.; Li, X.; Hratchian, H.; Izmaylov, A.; Bloino, J.; Zheng, G.; Sonnenberg, J.; Hada, M.; Ehara, M.; Toyota, K.; Fukuda, R.; Hasegawa, J.; Ishida, M.; Nakajima, T.; Honda, Y.; Kitao, O.; Nakai, H.; Vreven, T.; Montgomery, J.; Peralta, J.; Ogliaro, F.; Bearpark, M.; Heyd, J.; Brothers, E.; Kudin, K.; Staroverov, V.; Kobayashi, R.; Normand, J.; Raghavachari, K.; Rendell, A.; Burant, J.; Iyengar, S.; Tomasi, J.; Cossi, M.; Rega, N.; Millam, J.; Klene, M.; Knox, J.; Cross, J.; Bakken, V.; Adamo, C.; Jaramillo, J.; Gomperts, R.; Stratmann, R.; Yazyev, O.; Austin, A.; Cammi, R.; Pomelli, C.; Ochterski, J.; Martin, R.; Morokuma, K.; Zakrzewski, V.; Voth, G.; Salvador, P.; Dannenberg, J.; Dapprich, S.; Daniels, A.; Farkas; Foresman, J.; Ortiz, J.; Cioslowski, J.; Fox, D. Gaussian 09. *Gaussian 09 Gaussian Inc Wallingford CT* **2009**.

(49)   Hirata, S.; Head-Gordon, M.; Szczepanski, J.; Vala, M. Time-Dependent Density Functional Study of the Electronic Excited States of Polycyclic Aromatic Hydrocarbon Radical Ions. *J. Phys. Chem. A* **2003**, *107* (24), 4940–4951.

(50)   Treitel, N.; Shenhar, R.; Aprahamian, I.; Sheradsky, T.; Rabinovitz, M. Calculations of PAH Anions: When Are Diffuse Functions Necessary? *Phys. Chem. Chem. Phys.* **2004**, *6* (6), 1113–1121.

(51)   Bauschlicher, C. W. Time-Dependent Density Functional Theory for Polycyclic Aromatic Hydrocarbon Anions: What Is the Best Approach. *Chem. Phys. Lett.* **2005**, *409* (4–6), 235–239.

(52)   *MATLAB 2018a*; The MathWorks, Inc.: Natick, Massachusetts, United States.

(53)   Herzberg, G.; Teller, E. Schwingungsstruktur Der Elektronenübergänge Bei Mehratomigen Molekülen. *Z. Für Phys. Chem.* **1933**, *21B* (1), 410–446.

(54)   Orlandi, G.; Siebrand, W. Theory of Vibronic Intensity Borrowing. Comparison of Herzberg-Teller and Born-Oppenheimer Coupling. *J. Chem. Phys.* **1973**, *58* (10), 4513–4523.

(55)   Lin, S. H.; Eyring, H. Study of the Franck-Condon and Herzberg-Teller Approximations. *Proc. Natl. Acad. Sci. U. S. A.* **1974**, *71* (10), 3802–3804.

(56)   Bochenkova, A. V.; Mooney, C. R. S.; Parkes, M. A.; Woodhouse, J. L.; Zhang, L.; Lewin, R.; Ward, J. M.; Hailes, H. C.; Andersen, L. H.; Fielding, H. H. Mechanism of Resonant Electron Emission from the Deprotonated GFP Chromophore and Its Biomimetics. *Chem. Sci.* **2017**, *8* (4), 3154–3163.

CHAPTER 5

NON-COVALENT INTERACTIONS OF *PARA*-BENZOQUINONE

Photoelectron spectroscopy has long been used as powerful tool in the study of many biological molecules. In this chapter, we apply photoelectron imaging to the study of one such system, *para*-Benzoquinone (*p*BQ). While there have been many investigations focused on the photophysics of the isolated anion, far fewer studies have addressed the electronic properties of its oligomer anion clusters. In Chapter 5.1, we present PE spectra of $(p\text{BQ})_n^-$, $n = 2 - 4$, alongside theory to support our findings. While this study highlights the applicability of PE spectroscopy to larger systems, it also serves to demonstrate the limitations of DFT in relation to this area. In the latter section, 5.2, we extend the use of PE spectroscopy to $(p\text{BQ})^-\cdot H_2O$, to probe the effect of micro-hydration on *p*BQ. This chapter is based on the following publications:

Mensa-Bonsu, G., Wilson, M. R., Tozer, D. J., & Verlet, J. R. R.
Photoelectron spectroscopy of *para*-benzoquinone cluster anions.
J. Chem. Phys., 2019, **151**, 204302.

Mensa-Bonsu, G., Lietard, A., & Verlet, J. R. R.
Enhancement of electron accepting ability of *para*-benzoquinone by a single water molecule.
Phys. Chem. Chem. Phys., 2019, **21**, 21689.[1]

---

[1] Please note that the experimental results presented in Section 5.2 differs from that published due to a data processing error in which the signal intensity scale of the PE spectra was not divided through by *r,* the radial axis in pixels. As such, the 2D PE spectra previously published had dimensions of velocity space instead of electron kinetic energy. Mensa-Bonsu *et al.*, *Phys. Chem. Chem. Phys.*, 2020, **22**, 6013-6014.

5.1   PHOTOELECTRON SPECTROSCOPY OF *PARA*-BENZOQUINONE CLUSTER ANIONS

5.1.1   INTRODUCTION

Quinones are a class of cyclic diketone compounds which have significant biological relevance due to their ubiquitous role as an electron acceptor in nature. Of the various processes involving quinones, the function of ubiquinone and plastoquinone within the electron transport chains of respiration and photosynthesis, respectively, is particularly prominent.[1,2] Quinones have also been explored in replicating natural photosynthetic processes for the purpose of energy generation.[3,4] The central moiety common to all quinone derivatives[5] that is responsible for their electron accepting properties is benzoquinone,[6] with the *para*-benzoquinone structural isomer being the most common.[5] Owing to its simple structure (depicted in Figure 5.1.1(a)) and its abundance in nature, *p*BQ can be viewed as an "electrophore" - a chemical moiety with an efficient electron acceptor ability.[7] This ability is closely related to the dynamics of the resonances of the *p*BQ anion, *p*BQ$^-$.[8,9] Consequently, much work has been carried out towards understanding the resonances of *p*BQ$^-$.[6–31] However, in nature and in many synthetic systems, quinones are often found as dimers[32,33] and this leads to the natural question: how do the resonance dynamics change in *p*BQ oligomer anions, $(p\mathrm{BQ})_n^-$? From a materials perspective, oligomer dynamics are of key importance in understanding bulk properties. Much less is known about the photophysics of such clusters. Here, we explore how the oligomerisation of the singly charged *p*BQ anion affects the photoelectron spectroscopy.
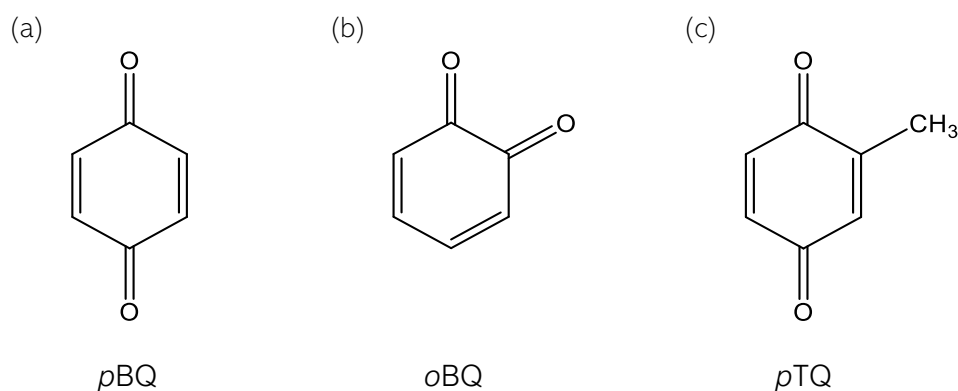

Figure 5.1.1: Structures of **(a)** *para*-benzoquinone **(b)** *ortho*-benzoquinone and **(c)** *para*-toluquinone.

*p*BQ has a large positive electron affinity (1.860 ± 0.005 eV) and is therefore capable of forming stable anions.[8] As the anion formation process is mediated by temporary excited

states of the anion (resonances), there have been many studies aimed at characterising the spectroscopy and resonances of pBQ⁻ and, moreover, to elucidate the photophysical processes involved in stable anion formation.[6,10,12–16,25,34] Schiedt and Weinkauf measured the photodetachment cross section of the jet-cooled radical anion within the 2.0 – 2.5 eV photon energy range and identified several resonances above threshold.[8] At photon energies resonant with resonances, the dominant detachment pathway was an indirect autodetachment channel (as opposed to the direct detachment pathway). 2D photoelectron spectroscopy of the anion resonances of pBQ⁻ have confirmed the presence of the previously reported ^2A_u shape resonance and the $^2B_{3u}$ Feshbach resonance, both at ~ 2.5 eV.[9,22] Time-resolved photoelectron spectroscopy and *ab initio* calculations were able to probe the decay mechanism of the resonances, which showed that internal conversion on a ~20 fs timescale was able to compete with autodetachment from the initially populated $^2B_{3u}$ resonance. This extremely fast decay provided an explanation of the efficiency of pBQ as an electron acceptor.[35] Prior to these works, Brauman *et al.* focused on finding evidence for a specific type of metastable doorway state in the electron attachment processes of radical benzoquinone: a dipole-bound state.[25] Although *para-* and *ortho*-benzoquinone have similar electronic structures (see Figure 5.1.1), the dipole moments of the isomers differ significantly, and as such, only oBQ is capable of sustaining a dipole bound state. This difference was reflected in the photodetachment action spectra of the benzoquinones for which oBQ⁻ showed resonances associate with the dipole-bound state, while pBQ⁻ did not.[25]

In addition to experiments using the anion as a starting point, the resonances of pBQ⁻ have been the subject of many electron scattering experiments.[10–21] In general, the photoelectron and photodetachment spectroscopy are in agreement with the electron scattering studies, although positions of resonances differ because of the differing initial geometries (*i.e.* anion and neutral geometries, respectively). Finally, pBQ⁻ resonances have also been the subject of several theoretical studies including scattering calculations and high-level electronic structure calculations.[7,26–31,33,36] Again, a generally consistent picture has emerged about the photophysics of the resonances of pBQ⁻ that is in overall agreement with the experimental work using many different methodologies.

In contrast to the wealth of information regarding the spectroscopy and dynamics of pBQ⁻, only a few studies have considered the clusters of related molecules. In electron scattering experiments, studying clusters is more challenging, as mass-selection of the initial neutral target is not possible. Experiments starting from anionic clusters do not suffer from this

restriction. The group of Brauman studied the photodetachment spectroscopy of *para*-toluquinone dimer $(pTQ)_2^-$.[24] In this, they found that a bound charge-transfer state (called a charge-resonance state, but we avoid this nomenclature for clarity here) that was excited at hv ~ 1.9 eV resulted in the dissociation of the cluster: $(pTQ)_2^- + hv \rightarrow pTQ + pTQ^-$. Our group has also studied clusters of *para*-toluquinone $(pTQ)_n^-$ ($n \leq 3$) by 2D photoelectron spectroscopy.[37] This showed some indirect evidence that the dimer dissociated above threshold, while the trimer revealed interesting valence to non-valence internal conversion dynamics near threshold, in which the non-valence state observed presented the first example of a predominantly correlation-bound state.[38] While pTQ can be viewed as a good approximation to pBQ (see Figure 5.1.1), we were previously not able to produce pBQ cluster anions in the electrospray source.[9] Here, we have generated $(pBQ)_n^-$ ($n \leq 4$) using a molecular beam source and we present its photoelectron spectroscopy at $hv = 4.00$ eV (310 nm). This shows the dimer does not undergo fragmentation following excitation (at this photon energy), while the trimer and tetramer dissociate to give anionic and neutral fragments.

5.1.2 EXPERIMENTAL & COMPUTATIONAL DETAILS

The experimental setup detailed in Chapter 2 has been employed in all experimental studies discussed throughout this chapter, therefore only an outline is given here. Solid pBQ was heated to 113°C in a pulsed valve, prior to the molecular vapour being expanded into vacuum using Ar as backing gas (3 bar). After spraying the resulting molecular beam with electrons, ion packets containing $(pBQ)_n^-$ ($n \leq 4$) were mass-selected and irradiated using nanosecond laser pulses. The subsequent photoelectrons were imaged by a velocity map imaging spectrometer.

Computational methods were employed to elucidate the structure of the radical $(pBQ)_n^-$ clusters produced and probed in the experiment. Given the size of the systems under consideration and their associated degrees of freedom, DFT becomes an unsuitable method to sample the configurational space of these clusters. Instead, molecular mechanics (MM) represents a computationally cheaper alternative for this purpose.[39,40]

MM uses classical potential energy functions to approximate the quantum mechanical Born-Oppenheimer surface.[41,42] However, unlike in electronic structure methods where electrons are considered explicitly, the energy of the molecular system in MM is evaluated at an atomistic level, where atoms are represented by single-point particles with empirically

derived properties such as radius and net charge. The bonds between atoms are treated as springs, capable of stretching, bending and rotating, with a predefined equilibrium length as determined by experiment or theory. Interactions between non-bonded atoms, such as van der Waals and electrostatic forces are also considered in this model.[39,42,43] The total energy of a conformational system can be expressed as the sum of these covalent and non-covalent interactions

$$E_{\text{total}} = E_{\text{stretching}} + E_{\text{bending}} + E_{torsional} + E_{\text{vdW}} + E_{\text{electrostatic}} \qquad (5.1)$$

Each of these interaction terms can be further defined using potential energy functions and a number of parameters.[41] This set of potential functions and their parameters are collectively known as a force field, which is used to compute the total energy of the system at a given nuclear configuration. The exact form of the force field varies and may include additional terms to describe interactions such as hydrogen bonding.[39,42]

As in this study, MM is often used to compute the minimum energy structures of a molecule. Underpinning MM is the notion that for every system, there is an optimum (equilibrium) geometry from which the molecule has become distorted through a series of non-bonding interactions. As such, in practical calculations, the energy of the system is routinely recomputed as the atomic positions within the molecule undergo optimisation, to reach a local energetic minimum.[41] In this study, the configurational space of $(p\text{BQ})_n^-$ was explored for $n = 2 - 4$ through a sequence of energy minimisation calculations using the SANDER functionality within the AMBER18 molecular dynamics package.[44] Although not a comprehensive analysis of configurational space, these calculations provided an indication of the dominant interactions, which govern the structure of the oligomer anion.

Starting with the dimer, restrained electrostatic potential (RESP) charges (HF/6-31G*) were assigned to one pBQ monomer (net –1 charge) and the other pBQ monomer remained neutral (zero net charge). For these two species, the minimisation calculations commenced from a series of 5000 random starting positions and orientations, in which the neutral monomer was positioned around the anionic monomer, distributed on spheres of radii between 3 and 15 nm. Minimisation calculations evolved from each of these starting positions using the generalised AMBER force field and RESP charges.[45] From this, a number of possible local minima were identified, which served as initial starting structures for DFT calculations. DFT optimisation calculations were performed at the ωB97XD/6-31+G* level of theory.[46,47] This functional was specifically designed with an emphasis on non-bonded interactions. A double

zeta basis set was employed to reduce the computational expense associated with the calculation of the larger oligomer clusters. For $(pBQ)_3^-$ and $(pBQ)_4^-$, the minimisation procedure was extended to allow random starting configurations for three and four species, by placing two and three randomly oriented monomers around a central anionic pBQ. For comparative purposes, the optimised geometry of the radical monomer anion was also computed using DFT at the same level of theory.

5.1.3   RESULTS & ANALYSIS

A.   EXPERIMENTAL

Photoelectron spectra were obtained for $(pBQ)_n^-$ ($n = 2 - 4$) at $hv = 4.00$ eV and were compared to that of pBQ^-, which had been measured at $hv = 4.20$ eV. Note that the spectrum of pBQ^- at 4.20 eV is almost identical as that at 4.00 eV (in terms of binding energy) and was taken at this photon energy to capture the triplet state of the neutral which served as an internal calibration.[23] The area-normalised spectra are displayed in Figure 5.1.2, where they have been plotted in terms of electron binding energy (eBE = hv – eKE).
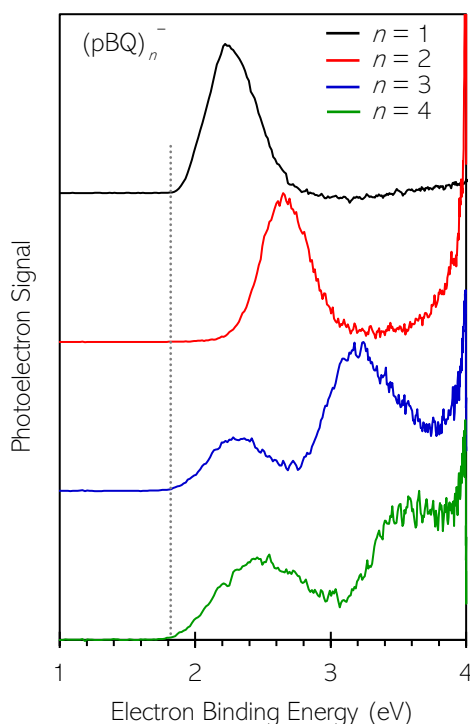
Figure 5.1.2: Photoelectron spectra of $(pBQ)_n^-$ ($n = 1 - 4$); $n = 2$ to 4 were taken at $hv = 4.00$ eV and $n = 1$ at $hv = 4.20$ eV. Each spectrum has been area normalised and offset vertically for clarity. The vertical dashed line indicates the adiabatic binding energy for pBQ^-.

The photoelectron spectrum of pBQ$^-$ shows a broad Gaussian-like feature centred around eBE ~ 2.2 eV. This band represents the direct detachment process in which an electron is instantaneously photoejected from the electronic ground state of the monomer anion, reforming neutral pBQ in its electronic ground state. The large spectral width of the peak arises from the significant difference in geometry between the anion and neutral. By measuring the eBE at which the onset and maximum of the direct detachment band occurs, the adiabatic and vertical detachment energies (ADE and VDE), respectively, can be determined (see Section 2.3.3). For pBQ$^-$, this yields ADE = 1.85 ± 0.02 eV and VDE = 2.24 ± 0.02 eV. These values are in agreement with previous experimentally determined detachment energies of pBQ$^-$.[8] The ADE is indicated in Figure 5.1.2 as the vertical dashed line.
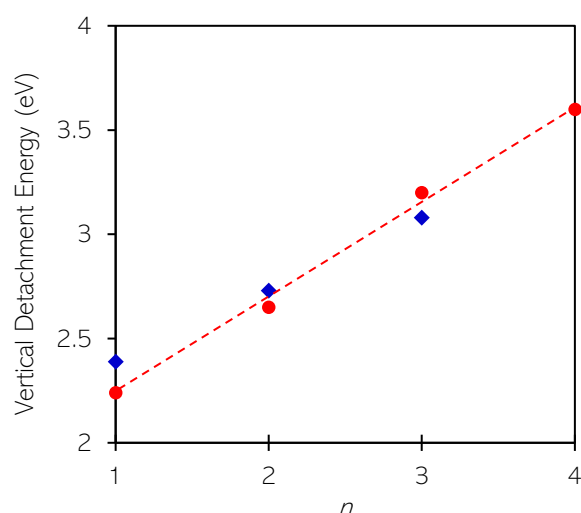
Figure 5.1.3: The trend in vertical detachment energies (VDE) of $(p$BQ$)_n^-$ with cluster size, determined from experiment (red circles) and theory (blue diamonds). The dashed lined is a guide to the eye for the experimental trend in VDE.

Figure 5.1.2 also shows the photoelectron spectra of the clusters, $(p$BQ$)_n^-$ ($n = 2 - 4$). The photoelectron spectrum of the dimer has a very similar appearance as that of the monomer, but blue-shifted by ~ 0.4 eV. The trimer and tetramer show similar bands with similar successive increases in binding energy. These peaks can be assigned to direct detachment into the continuum. The VDE can be extracted from these spectra as done for the monomer and the incremental shift in the VDEs of $(p$BQ$)_n^-$ are plotted in Figure 5.1.3. Lower photoelectron signals for the larger clusters ($n = 2 - 4$) complicate the accurate determination of their VDEs, resulting in a larger error associated with these values (±0.1 eV). The error in the VDEs of the

larger clusters has been determined by visual inspection of the corresponding spectra and reflects a range in which we are confident that the true VDE lies. By inspection of Figure 5.1.2, assigning the ADE is only possible for the monomer and dimer as photoelectron signal obscures the direct detachment peak onset for $n = 3$ and 4.

In addition to the blue-shifting direct detachment band, a feature peaking at zero kinetic energy (eBE = $h\nu$ = 4.00 eV) is present in the spectra for all values of $n > 1$. Moreover, the spectral profile of these narrow peaks is featureless and has an exponential spectral profile. Near-zero kinetic energy peaks that have a Boltzmann-like energy distribution are typically signatures of thermionic (statistical) electron emission.[48–50] To observe such features requires the formation of a hot electronic ground state (with internal energy in excess of the electron binding energy) following the interaction with a photon. Hence, the observation of thermionic emission suggests that at $h\nu$ = 4.00 eV, a resonance is excited in the clusters that ultimately leads to some ground state products, which emit electrons on a longer (typically μs) timescale.

Perhaps the most striking features in Figure 5.1.2 are the photoelectron peaks in $(pBQ)_3^-$ and $(pBQ)_4^-$ at lower binding energy than the direct detachment peak for these clusters. Clearly visible are broad features at eBE $\approx$ 2.37 and 2.50 eV in $(pBQ)_3^-$ and $(pBQ)_4^-$, respectively. By inspection of Figure 5.1.2, the energies of the red-shifted peaks are similar to the direct detachment peaks present in the spectrum of the monomer. This is most clearly the case for $n = 3$ although the lower binding energy peak appears slightly blue-shifted and broadened compared to the monomer. For $n = 4$, the peak is significantly broader and blue shifted and appears to encompass both the monomer and dimer photoelectron spectra.
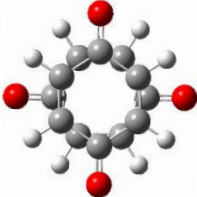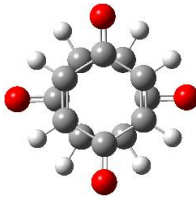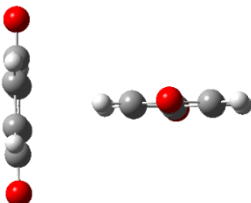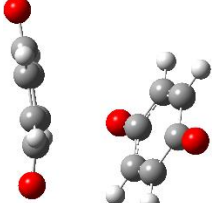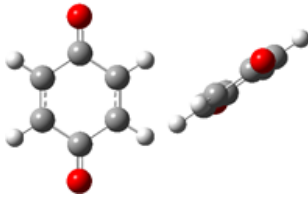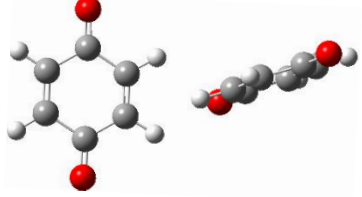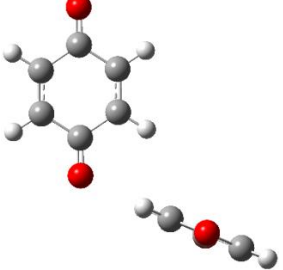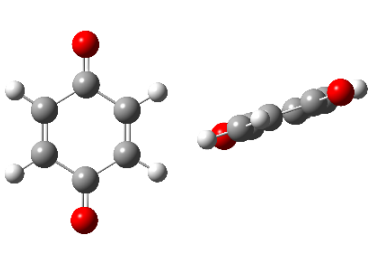

B.   COMPUTATIONAL
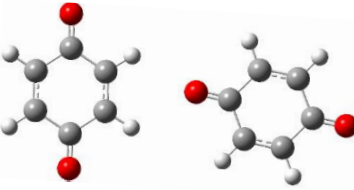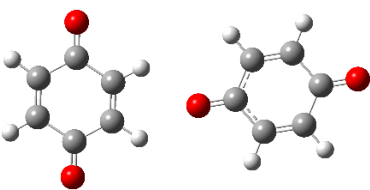
The DFT optimised ground state geometry of pBQ^- corresponds to a planar structure with D_{2h} symmetry. The VDE of pBQ^- was computed to be 2.39 eV. This value is in agreement with the DFT computed energy previously reported by Stockett and Nielsen and lies within ~0.2 eV of the experimental value determined here.[6]

The conjugated nature of pBQ gives rise to a π-electron cloud capable of engaging in π-stacking. Additionally, pBQ can also partake in hydrogen bonding through its *para*-oxygen atoms. The balance between these non-covalent interactions can lead to structural ambiguity regarding its anionic oligomers. In order to address this, AMBER minimisation calculations were performed on $(pBQ)_2^-$ and five possible configurations of the dimer were identified (Table

5.1.1). Of the five structures identified, two configurations (**I** and **II**) are assembled in π-stacked arrangements (sandwich and T-shaped respectively). This is in contrast to **III**, **IV** and **V** in which the two molecules of the dimer are associated predominantly through hydrogen bonding interactions. Configurations **IV** and **V** appeared to be structurally identical, only differentiable by a small rotation of a single ring and the resulting minor difference in the AMBER minimisation energy (0.3 meV).

DFT calculations commencing from the five AMBER configurations indicated that the π-stacked structures, **I** and **II**, were the most stable (relative energies are given in Table 5.1.1). Geometric changes in the overall structures of **I** and **II** were observed following the DFT optimisation. The most notable of these was the translation and rotation of a single fragment in **II**, which led to the configuration adopting an arrangement closer to sandwich π stacked geometry. Finer geometrical changes in the case of **I** and **II** include a buckling of the two oxygen atoms out of the plane of the pBQ ring. In Figure 5.1.4, the DFT optimised structure of the lowest energy configuration is presented for the dimer and clearly shows this out-of-plane distortion. Optimisation calculations employing configurations **IV** and **V** converged to single structure, which was deemed the most energetically unfavourable structure of all the five structures considered here. For all DFT configurations, the net charge is predominately localised on a single monomer with the other neutral monomer effectively solvating the charge. The computed VDE of the dimer is 2.73 eV and is included in Figure 5.1.3.

Table 5.1.1: AMBER energy minimised configurations of (pBQ)$_2^-$ labelled as I – V are depicted alongside their corresponding DFT optimised structures. Corresponding relative optimisation energies and vertical detachment energies are also shown.

	AMBER Minimised	DFT Optimised	Opt. Energy (meV)	VDE (eV)
I			0	2.73
II			80	2.82
III			126	2.77
IV			129	2.76
V			129	2.76
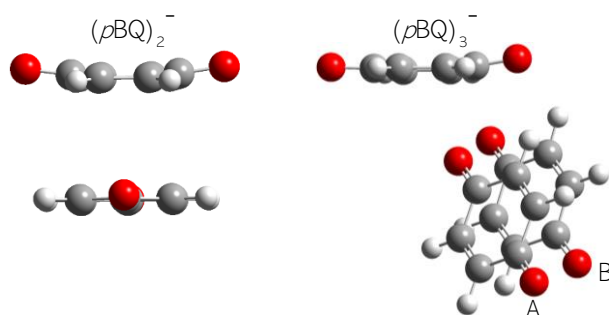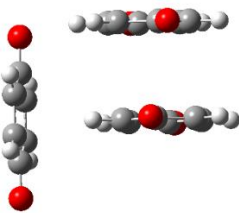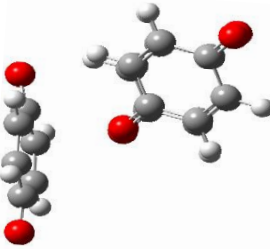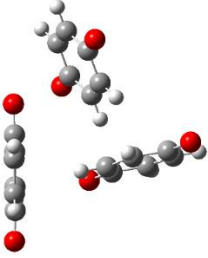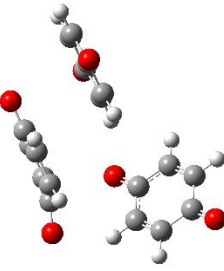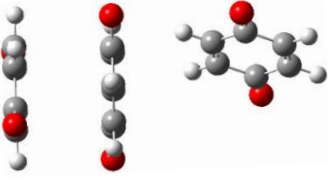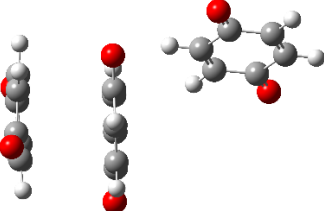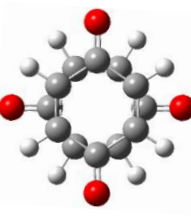
Figure 5.1.4: The minimum energy structures of $(p\mathrm{BQ})_2^-$ and $(p\mathrm{BQ})_3^-$. For the dimer, the excess charge is localised on the planar, unbuckled fragment. For the trimer, the net charge is predominantly localised on the stacked fragment labelled A.

Repeating the AMBER computational process for the trimer anion yielded 14 possible minimum energy structures. Broad similarities can be identified between a number of configurations, allowing these 14 structures to be separated into 5 overall structural classes. Geometries within each class are differentiable through fragment rotations and do not lead to significant changes in energies. In fact, DFT energy minimisations of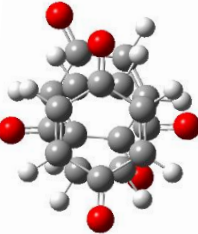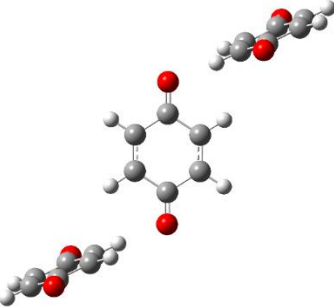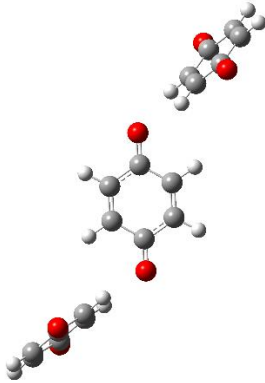 different structures within a given class often led to a single structure. A representative geometry from each structural class for $(p\mathrm{BQ})_3^-$ is shown in Table 5.1.2.

DFT calculations identified class **I** structures as the most stable and the lowest energy structure for the trimer following the optimisation of class **I** is shown in Figure 5.1.4. Class **I** configurations consist of two π-stacked fragments in a parallel-displaced arrangement, with a third fragment held in place by a combination of quadrupole-quadrupole and hydrogen bonding interactions. Similar to the dimer, the charge in the class **I** structure is largely localised on one of the π-stacked monomers. DFT geometry optimisations of the class **I** configuration resulted in significant structural changes, including a translational shift of the unstacked fragment and a significant rotation of the π-stacked fragments, although their parallel-displaced arrangement was retained (*cf.* Figure 5.1.4 and Table 5.1.2). Much like the dimer, the hydrogen-bonded monomer buckles out of the plane of the quinone ring, as also previously noted in the $(p\mathrm{TQ})_3^-$ study.[37] The calculated VDE of the trimer is 3.08 eV and has been included in Figure 5.1.3.

Table 5.1.2: Classes of AMBER energy minimised configurations of $(p\mathrm{BQ})_3^-$ are depicted alongside their corresponding DFT optimised structures. Averaged relative optimisation energies and vertical detachment energies are also shown.

	AMBER Minimised	DFT Optimised	Opt. Energy (meV)	VDE (eV)
I			0	3.07
II			80	3.10
III			140	3.07
IV			170	2.87
V			270	3.09

The number of local minima produced by molecular mechanic simulations typically scale with an increasing number of variables. Due to computational expense associated with DFT optimisations and the additional ambiguity in assigning structures, the lowest energy structure of $(p\mathrm{BQ})_4^-$ has not been computed. The 4 lowest energy configurations produced by AMBER minimisation simulations have been depicted in Figure 5.1.5.
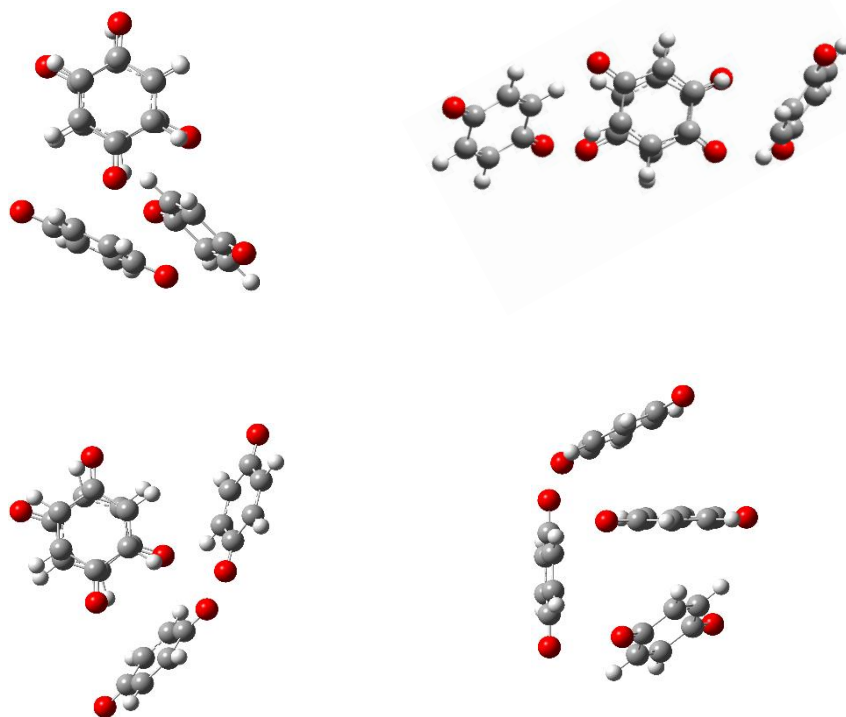
Figure 5.1.5: The four lowest energy structures of $(p\mathrm{BQ})_4^-$ computed by AMBER minimisation.

5.1.4 DISCUSSION

A. VERTICAL DETACHMENT ENERGIES AND CLUSTER STRUCTURES

Figure 5.1.2 shows that the peak assigned to direct detachment in $(p\mathrm{BQ})_n^-$ has a similar spectral profile to that of $p\mathrm{BQ}^-$. As the clusters become larger, the binding energy increases. The spectral widths do not change appreciably between $n = 1$ and 2 but appear to become larger for $n = 3$ and 4, although these are also affected by the indirect features on either side of the direct detachment peak. The fact that the direct photoelectron spectra retain a similar shape suggests that the charge remains predominantly localised on one $p\mathrm{BQ}$ monomer, which is solvated by a neutral $p\mathrm{BQ}$. This is consistent with the DFT calculations that show that the charge is predominantly localised on one monomer. In the case of the dimer, the ωB97XD

computed Mulliken charges show that 93% of the net charge is localised on the non-buckled monomer. The computed charges of the trimer also show localisation but to a lesser extent, with 34% and 66% of the charge residing on the upper and lower π-stacked monomers labelled in Figure 5.1.4(b) as A and B, respectively. The wider charge distribution observed for the trimer could be attributed to the well-known delocalisation error in approximate DFT functionals,[51,52] where the charge is artificially delocalised in order to lower the energy of the system. It is well known that this error is highly sensitive to the amount of exact exchange. For comparative purposes, Mulliken charges of the trimer were also computed using Hartree Fock (HF) and BLYP, which represent the extreme cases of 100% and 0% exact exchange, respectively. HF/6-31+G* calculations showed enhanced localisation (94% of the excess charge on A), while BLYP led to essentially equal amounts on the dimer (55% on A), illustrating the sensitivity to the amount of exchange. As such, it is difficult to quantify the charge distribution, but from these results a degree of localisation can be inferred. It should be noted that Mulliken charges are also highly basis set dependent. To this end, the use of another method such as the Merz-Kollman scheme would be desirable. However, Mulliken population analysis is a considerably cheaper method which makes its use preferable for the sizable systems studied in this chapter.[53]

The increase in VDE with each successive n can be explained in terms of the strength of the intermolecular binding present in the oligomer complexes. As the size of the anion clusters increase, so too does the number of intermolecular electrostatic (hydrogen bonding) interactions, resulting in stronger binding for larger n. The increase in VDE can be explained pictorially with reference to the potential energy surfaces shown in Figure 5.1.6. The interactions in the anions are generally stronger than in the neutral because of the charge-induced electrostatic interactions. Hence, the cohesion energy in the anions is higher than in the neutral such that an incremental increase in VDE is observed with n. The computed VDEs are in good agreement with the experimentally determined energies, lying < 0.2 eV of the experimental values in all cases. Moreover, as shown in Figure 5.1.3, the overall trend is well captured qualitatively. However, the quantitative gradient of VDE(n) appears to be slightly underestimated.

A further inaccuracy in the computed VDEs may arise from the basis set superposition error which has not been accounted for in our DFT calculations. When using a finite basis set to describe a system of interacting molecules, the basis functions of each molecule overlap at shorter intermolecular distances. This allows a monomer fragment to "borrow" the basis

functions of other fragments within the system to describe its own electron distribution, artificially lowering the energy of the system. The basis set superposition error arises from the inconsistent treatment of the system with varying intermolecular distance. At long range, the utilisation of extra basis functions is not possible due to the distance between the molecules. This leads to the use of an effectively smaller basis set to describe the electron distribution of each monomer and thus, to a poorer characterisation of the system's properties.[54] In the absence of a complete basis set, methods such the counterpoise correction and the chemical Hamiltonian approach can be implemented to eliminate the basis set superposition error,[54–57] neither of which have been used here.
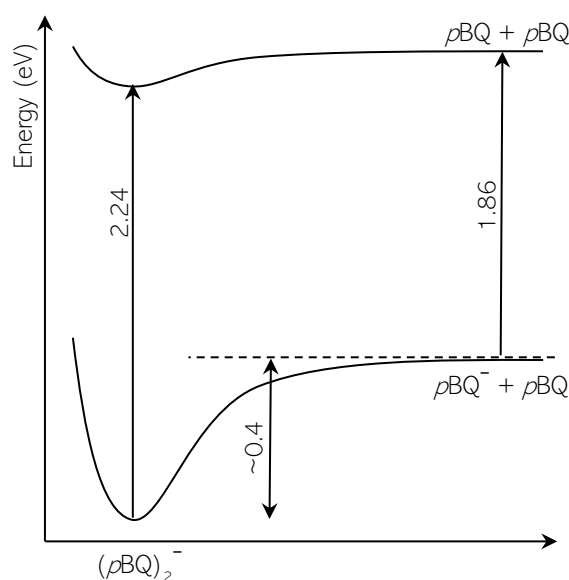
Figure 5.1.6: Schematic of the anion and neutral potential energy curves (shown as a function of the distance between the centres of mass), in which the difference in well depth accounts for the difference observed in vertical detachment energy.

Overall, the cluster structures determined by the calculations appear reasonable. Our only experimental probe for the structure is the photoelectron spectra and the VDE that can be extracted from these. Comparison of the computed and measured VDEs shows that they are in reasonable agreement. However, we note that the calculation of VDEs for different cluster structures and even in different cluster structure classes for the trimer leads to broadly similar VDEs (Tables 5.1.1 and 5.1.2). This is not wholly surprising given the fact that the charge is mostly localised in all clusters. Hence, there is some ambiguity about which structures are actually present in the ion packet under experimental conditions. In particular, because there

are several structures that are relatively close in energy and lead to similar VDEs, a number of structures may be contributing to the ion packet for $n = 3$ and 4. This may in turn explain the broadening observed in the direct detachment peak for these two clusters. Nevertheless, we do expect relatively cold clusters as the electron attachment occurs at the throat of the expansion and most of the supersonic cooling occurs beyond this point. Note that we also see evidence of Ar clusters in the mass-spectrum indicating efficient overall cooling.

B.　DYNAMICS OF RESONANCES

Present in the photoelectron spectra of $n = 3$ and 4 are additional features at eBE = ~2.37 and 2.50 eV, respectively. These bands could arise from different cluster geometries. However, as all reasonable structures generally give broadly similar VDEs, this seems very unlikely. Instead, for all clusters studied here, $hv = 4.00$ eV appears to excite a resonance in the systems as evidenced by the slow (thermionic) electrons being emitted. The photodetachment cross section measured by Brauman and co-workers shows that a broad resonance is present for pBQ$^-$ at 4 eV,[24] which can be assigned to a higher-lying $^2B_{3u}$ state. However, for the monomer, this resonance does not lead to an observable change in the photoelectron spectrum and the 2D photoelectron spectrum showed no evidence for ground state reformation following excitation to this resonance.[9] Given the evidence that the charge remains localised predominantly on a single pBQ within the clusters, it is reasonable to suggest that this same resonance is excited in the clusters. The lower binding energy features seen in the $n = 3$ and 4 photoelectron spectra are likely due to dynamics of this resonance in the cluster. By inspection of Figure 5.1.2, the indirect photoelectron features appear to be at similar energies as that for the monomer, pBQ$^-$. Specifically, if the ADE is traced down from pBQ$^-$ to $(p$BQ$)_3^-$ and $(p$BQ$)_4^-$, as shown by the dashed line in Figure 5.1.2, then it is clear that this lines up well with the ADEs of the indirect features. Hence, we propose that these features arise from electron photodetachment from the monomer following excitation of the cluster. This would of course require a dissociative process upon excitation to the resonance. The appearance of the monomer would then require two photons.

$$(p\text{BQ})_3^- \xrightarrow{hv} [(p\text{BQ})_3^-]^* \longrightarrow (p\text{BQ})^- + (p\text{BQ})_2$$
$$\downarrow hv \qquad\qquad (1)$$
$$p\text{BQ} + e^-$$
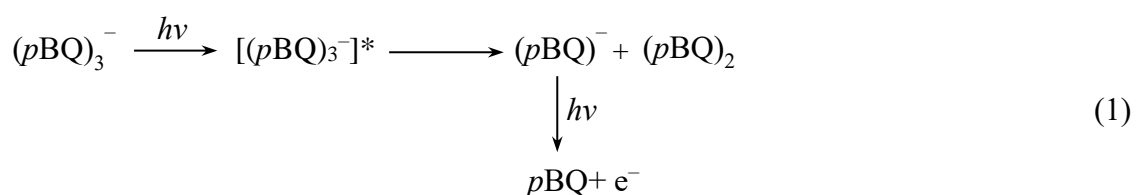
Using $(pBQ)_3^-$ as an example, the proposed mechanism is given in Scheme 1. Absorption of the first photon by the cluster anion leads to excitation to a resonance after which, photodissociation ensues, forming the charged monomer and neutral dimer species (or complete dissociation into 3 monomers with one carrying the excess negative charge). The absorption of a second photon by pBQ^- then generates the neutral monomer that is observed in the photoelectron spectrum of $(pBQ)_3^-$.

For both photons to be absorbed, the dynamics leading to dissociation must be on a timescale less than the laser pulse duration, which is ~ 5 ns. Excited state dissociation would unquestionably be faster. However, internal conversion of the resonance to form the ground state could also lead to dissociation because the 4 eV total energy imparted into the cluster is well above its binding energy. We note that the presence of thermionic emission evidences ground state reformation, so this is a possible mechanism. However, we cannot say whether thermionic emission is from the ground state of the cluster anion or from the monomer anion as there would be sufficient energy for either to lead to thermionic emission. From the spectral width in Figure 5.1.2, the direct detachment from the pBQ^- fragment following $(pBQ)_3^-$ dissociation is significantly broadened with respect to the photoelectron spectrum of pBQ^-. This highlights that the pBQ^- fragment produced has a large amount of internal energy. The spectral blue-shift of the binding energy then suggests a differing Franck-Condon profile at higher internal energies and we do observe also that the ADE is slightly shifted to lower energies, presumably because of hot band contributions to the photoelectron spectrum. Ultimately, it is not possible to ascertain with certainty whether photodissociation of the anion cluster occurs on the resonance or following internal conversion to the ground state of the anion. This could potentially be probed by time-resolved photoelectron spectroscopy, but these experiments are beyond the scope of this work.

For $(pBQ)_4^-$, there is a further increase of spectral width as well as an increase in binding energy associated with the detachment band from the fragment. The increased width is not likely to be due to an increase in the internal energy of the pBQ^- fragment as there are now more modes and the tetramer has a broadly similar binding energy as for $(pBQ)_3^-$. Instead, the much-increased width suggests that there may be other products of the photodissociation. Specifically, Figure 5.1.2 shows a significant broadening of the indirect peak indicating that two components are required to reproduce the spectral shape and suggest that both the anionic monomer and dimer are produced in the dissociation process. As with the dissociation of the trimer, the width suggests that the fragments are produced with a large amount of internal

energy. Nevertheless, the $(p\text{BQ})_2^-$ fragment appears to survive the dissociation on the timescale of ~5 ns. Our experiments cannot determine which fragment is dominant because of the unknown timescales involved in the process and the fixed laser pulse duration. Finally, we comment that a power dependence of the indirect versus direct detachment signals would have been useful as a further confirmation of the above assignment, but our signal levels were too low to convincingly do this.

The experimental and computational results reveal similarities between $(p\text{BQ})_n^-$ and its methylated analogue, $(p\text{TQ})_n^-$.[37] The calculated minimum energy configurations of $(p\text{BQ})_n^-$ bear strong resemblance to those predicted for $(p\text{TQ})_n^-$, $n = 2$ and 3. In both cases, the anion clusters adopt predominantly π-stacked arrangements, with both molecules exhibiting out-of-plane buckling of one monomer and charge localisation. For $n = 3$, both molecules adopt a parallel-displaced stacked arrangement with a third, hydrogen bonded monomer assembled in a distorted T shape. Similarly, the cohesion energy between the two clusters is broadly similar suggesting that the methyl group has a minor impact. In contrast, the anionic dimer of coenzyme Q_0, $(CQ_0)_2^-$, which has two additional methoxy groups on the ring side opposite to the methyl in $p\text{TQ}$, has a cohesion energy of ~1.0 eV for the dimer.[58] This increased binding can be correlated to the ability of $(CQ_0)_2^-$ to form additional hydrogen bonds.

Some of the commonalities between $(p\text{BQ})_n^-$ and $(p\text{TQ})_n^-$ also extend to their spectroscopic properties. Dissociation was also observed in $(p\text{TQ})_2^-$. Comita and Brauman identified a bound state at 1.9 eV, which dissociated to form the monomer anion that was observed in the experiment.[24] Dissociation was also inferred from photoelectron spectra following excitation of resonances at $h\nu \sim 3$ eV.[37] However, poor signal-to-noise meant that we could not explore the photoelectron spectroscopy of the $(p\text{TQ})_2^-$ at $h\nu = 4.00$ eV as probed here. In contrast, $(p\text{TQ})_3^-$ did not show evidence of dissociation, including at $h\nu \sim 4$ eV. Instead, for $2.5 < h\nu < 3.4$ eV, internal conversion to form a non-valence state was observed.[38] The same mechanism was also observed in $(CQ_0)_2^-$ around the detachment threshold,[58] which also did not show dissociation at $h\nu \sim 4$ eV.

Unfortunately, we could only conduct the present experiments at a single photon energy. It would be interesting to perform 2D photoelectron spectroscopy to probe the photon energy dependence of the dissociation, similar to the dissociation we previously observed in p-dinitrobenzene,[59] but this would require higher signal levels than are currently attainable.

5.2 PROBING THE ELECTRON ACCEPTING ABILITY OF *PARA*-BENZOQUINONE UPON HYDRATION

5.2.1 INTRODUCTION

As demonstrated in the previous section, probing the possible decay pathways of anion resonances in the gas phase using photoelectron spectroscopy can provide a route to determining the intrinsic photophysics of the molecule, undisturbed by the complex environment.[60–63] However, when considering molecules of biological relevance, which predominantly occur in the condensed phase,[64] the ability of the immediate environment to affect the photophysical properties of the molecule must also be taken into account. Using the experimental setup described in Chapter 2, it is not possible to study pBQ$^-$ in the condensed phase or at the surface. However, the effect of the microenvironment on the properties of the molecule can be studied through the addition of water molecules to the isolated anion. This is particularly relevant for quinones which can exist within proteins in a microhydrated form, surrounded by a small number of water molecules amongst other species. As such, we have extended the PE study of pBQ$^-$ to its hydrated complexes, pBQ$^- \cdot$(H$_2$O)$_n$ in order to probe how a micro-environment alters the spectral properties of pBQ$^-$ and to investigate the effectiveness of water molecules to affect ground-state anion formation.

5.2.2 EXPERIMENTAL & COMPUTATIONAL DETAILS

The methodology detailed in Section 5.1.2 was employed to measure the frequency-resolved 2D PE spectrum of pBQ$^- \cdot$(H$_2$O)$_n$. Using the same experimental conditions as that stated in Section 5.1.2 and Ar as a backing gas, pBQ$^- \cdot$(H$_2$O)$_n$ clusters were generated when solid pBQ was heated to 120°C prior to their expansion into vacuum, where the resulting molecular beam was crossed with an electron beam. Additionally, a drop of water was added to the Ar backing line which provides a sufficient vapour pressure (1.98 bar at 120 °C) to enable the production of pBQ$^- \cdot$(H$_2$O)$_n$. Clusters were mass selected and irradiated using nanosecond laser pulses. Subsequent photodetached electrons were then imaged using velocity map imaging.

To support our experimental findings, the minimum energy structure of pBQ$^- \cdot$H$_2$O has been reproduced using the method stated in Ref. 6, which involves the computation of the structure at the B3LYP/6-311G(2d,p) level of theory.[6,65,66]

5.2.3 RESULTS & DISCUSSION

A series of PE spectra were obtained for pBQ$^-$ and pBQ$^-\cdot$H$_2$O over a photon energy range of 2.3 - 4.0 eV in 50 meV intervals. The resulting spectra were compiled in 2D intensity maps of PE signal as a function of the incoming hv and outgoing electron kinetic energy (eKE), using the bilinear interpolation function featured in MATLAB to smooth the data. The 2D PE spectra of pBQ$^-$ and pBQ$^-\cdot$H$_2$O are presented in Figure 5.2.1.
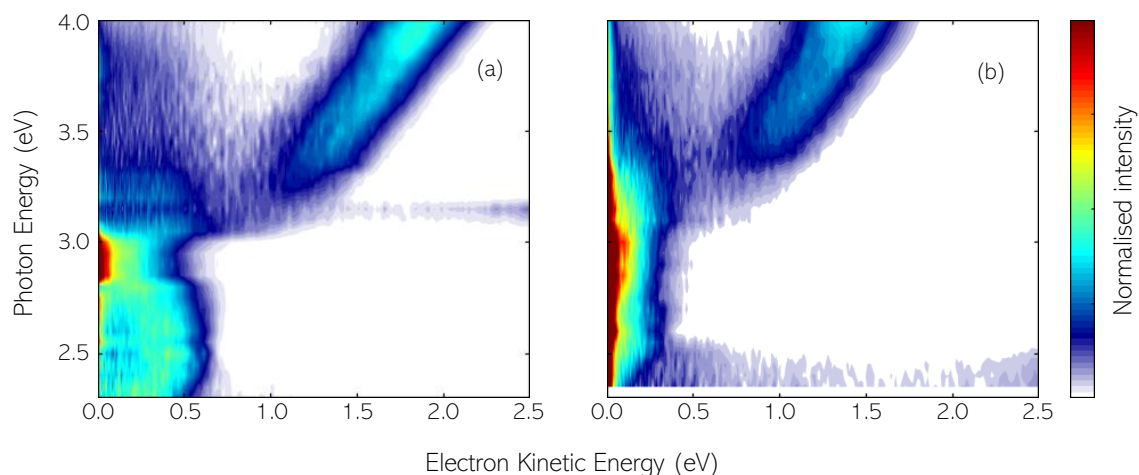

Figure 5.2.1: Frequency-resolved (2D) photoelectron (PE) spectra of jet-cooled **(a)** pBQ$^-$ and **(b)** pBQ$^-\cdot$H$_2$O recorded in the range 2.3 $\leq hv \leq$ 4.0 eV. Each PE spectrum has been normalised to its total signal intensity.

As has previously been discussed in Section 1.6, plotting PE spectra as a 2D map allows one to infer decay dynamics from patterns within the spectra. Direct detachment features appear as diagonal lines. Off-diagonal, red-shifted (towards lower eKE) signals indicate indirect detachment channels that are associated with dynamics of resonances. The 2D spectra of pBQ$^-$ (Figure 5.2.1(a)) shows that for hv > 3.4 eV direct detachment appears to be the dominant channel. Present at hv ~ 2.8 eV are signatures of resonances as evidenced by strong off-diagonal features. Using time-resolved PE spectroscopy, we have shown that the red-shifted peak in the PE spectrum comes about from autodetachment from the ^{2}A$_u$ shape resonance that is produced following internal conversion through a conical intersection following excitation of the ^{2}B$_{3u}$ Feshbach resonance (note that pBQ$^-$ has D_{2h} symmetry in the anion and neutral geometries).[35] Below photon energies of 3.1 eV, an additional spectral feature can be observed near eKE = 0 eV. Very low-energy peaks with a characteristic Boltzmann distribution are commonly seen in PE spectroscopy of anions.[9,34] These arise from a statistical

electron emission process from the electronic anion ground state,[49,67] which thus points to the regeneration of the anion.

Figure 5.2.1(b) shows the 2D PE spectrum of jet-cooled pBQ$^-$·H$_2$O which is directly comparable to the bare anion in Figure 5.2.1(a). The overall PE spectrum of the monohydrated species appears very similar to the bare anion, with indirect decay features present at $hv < 3.1$ eV. At higher photon energies ($hv > 3.4$ eV) direct detachment is the dominant decay pathway. Given the similar spectral signatures, particularly with reference to the indirect detachment channels, one can infer that complexation with a water molecule does not affect the resonance positions of pBQ$^-$.

These findings are in agreement with that of Stockett and Nielsen,[6] who probed the effect of the resonance locations upon the addition of a water molecule to pBQ$^-$ using experimental and computational methods. The authors presented photodepletion spectra of bare pBQ$^-$ between 200 - 700 nm, from which they identified two spectral bands corresponding to the ^{2}A$_u$ and ^{2}B$_{3u}$ resonances. Comparison between the photodepletion spectra of isolated pBQ$^-$ and pBQ$^-$·H$_2$O revealed striking commonalities, including in the energetic position of the ^{2}B$_{3u}$ resonance, which remained unchanged. Other resonances were identified at lower energies of $hv \sim 2.3$ and 2.4 eV in the H$_2$O loss depletion spectra, which were in energetic agreement with Feshbach resonances (to the ^{2}B$_{2u}$ and ^{2}B$_{3g}$ states) observed in the photodetachment spectra of pBQ$^-$ by Schiedt and Weinkauf.[8] The numerous similarities in the spectra of bare pBQ$^-$ and its microhydrated form, suggest that the addition of water does very little to affect the energetic positions of the resonances.

These results are somewhat surprising because of the strong interaction between the anion and the water molecule; because the water molecule breaks the symmetry of the system, which one might intuitively expect to lead to a localisation of the negative charge near the oxygen that bonds to the water molecule; and because studies of excited states in other micro-solvated species have been predicted to shift in energy.[68,69] In principle, the addition of a water molecule can also lead to new reaction pathways. Specifically, proton transfer to form OH$^-$ and the benzo-semiquinone, C$_6$H$_5$O$_2$, are possible reaction products. However, electron photodetachment from OH$^-$ was not observed in the PE spectra, which should be clearly visible if the reaction occurred on a timescale of a few nanosecond as the electron affinity of OH$^-$ is 1.83 eV.[59,70] This conclusion agrees with the study by Stockett and Nielsen that also did not

observe OH$^-$ following photodissociation and they additionally calculated that water loss was energetically favoured by ~ 4 eV.[6]

Although the location of resonances appears to be unchanged with the presence of a water molecule, the PE spectra of pBQ$^-$·H$_2$O show clear differences to pBQ$^-$ between $2.5 < h\nu < 3.0$ eV (Figure 5.2.1). In this range, the feature peaking at eKE = 0 eV attributed to thermionic emission is of significantly greater intensity in pBQ$^-$·H$_2$O. Thermionic emission is a decay pathway characterised by photodetachment of an electron from the anion to the neutral ground states. However, as this process is of a statistical nature, anion ground state reformation may occur instead of photodetachment. The observed increase in thermionic emission for pBQ$^-$·H$_2$O suggests that the anion ground state is reformed with greater efficiency when pBQ$^-$ is in its hydrated form. Relating this observation to a biological function of the molecule, pBQ is expected to form a stable anion when acting as an electron acceptor in biological systems and thermionic emission represents a decay pathway by which to achieve this. Therefore, increased thermionic emission is indicative of the enhanced performance of pBQ·H$_2$O as an electron acceptor.

Another notable distinction between pBQ$^-$ and pBQ$^-$·H$_2$O is that the direct detachment into the continuum is red-shifted with the addition of a water molecule. This is most noticeable for $h\nu > 3.5$ eV in Figure 5.2.1. The adiabatic detachment energy (ADE) was determined from the onset of the PE signal to be ADE = 1.85 ± 0.02 eV and 2.22 ± 0.02 eV for pBQ$^-$ and pBQ$^-$·H$_2$O, respectively. The former is in good agreement with previous measurements from Schiedt and Weinkauf (1.860 ± 0.005 eV).[8] The consequence of the increased ADE is that no meaningful PE signal is observed for $h\nu < 2.5$ eV for pBQ$^-$·H$_2$O in Figure 5.2.1(b). The increase in ADE by 0.37 eV predominantly reflects the binding energy of pBQ$^-$ to H$_2$O.

As part of their study, Stockett & Nielsen computed the structure of pBQ$^-$·H$_2$O.[6] DFT calculations at the B3LYP/6-311G(2d,p) level gave the minimum energy structure of the cluster as one in which the water is bound to a single oxygen atom on pBQ$^-$. We have reproduced the same calculation and the structure is shown in Figure 5.2.2. Charges computed at the same level of theory for the complex show that the net –1 charge is localised on the pBQ molecule. These results are supported by the 2D PE spectra (Figure 5.2.1), in which the overall shape of the direct detachment band remains essentially the same upon mono-hydration, verifying that the overall electronic structure of pBQ$^-$ has not changed despite the strong binding interaction with H$_2$O.
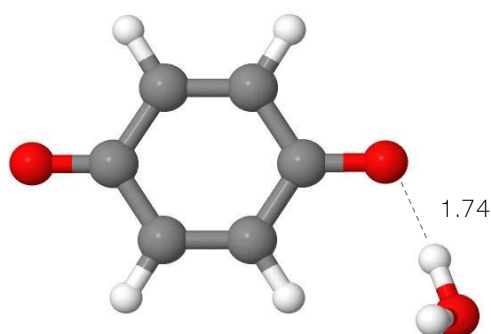
Figure 5.2.2: Calculated minimum energy structure of the *para*-benzoquinone anion solvated by a single water molecule, pBQ$^-$·H_2O. The calculated hydrogen bond length is stated in Å.

The enhanced electron accepting ability of pBQ upon solvation by a single water molecule is surprising considering the insensitivity of the resonances to mono-hydration. Even though the neutral state is now ~0.37 eV higher in energy relative to the anionic states, it is clear that, at least in the anion geometry, the bright excited states (^2A_u and $^2B_{3u}$ resonances in bare pBQ$^-$) are still resonances. For pBQ$^-$, the internal conversion dynamics were measured to be on a ~20 fs timescale (*i.e.* a single vibration),[35] and so it is not clear how this can be faster with a water molecule present. The main ultrafast electron loss channel in pBQ$^-$ is the autodetachment from the ^2A_u resonance (see Figure 5.2.1(a)) and so, it would appear that this channel has now been inhibited. This can perhaps be rationalised by the increased energy of the neutral so that this intermediate state may become bound along the nuclear displacement coordinates involved in the decay dynamics.[71] Another possible explanation is that small changes in the resonance energies have caused the observed dynamical changes. Specifically, close inspection of the rising edge of the action (absorption spectra) by Stockett and Nielsen does show a small blue-shift (~50 meV) of the ^2A_u resonance upon complexation. Additionally, the optically dark nπ* resonances of pBQ$^-$ may be much more sensitive to a water molecule and could participate very differently to the internal conversion through the excited state manifold. Such a case has been observed in microsolvated sunscreen molecules for example.[72] A further important difference upon addition of a water molecule is the long-range forces that the outgoing (scattering) electron experiences and their asymmetry. Specifically, isolated pBQ$^-$ has no dipole, but pBQ·H_2O in the anion geometry does, with a calculated magnitude of $\mu =$ 3.0 D, which predominantly arises from the H_2O dipole and is sufficient to support a dipole-bound state,[73–75] which may influence the electron-molecule reaction dynamics.
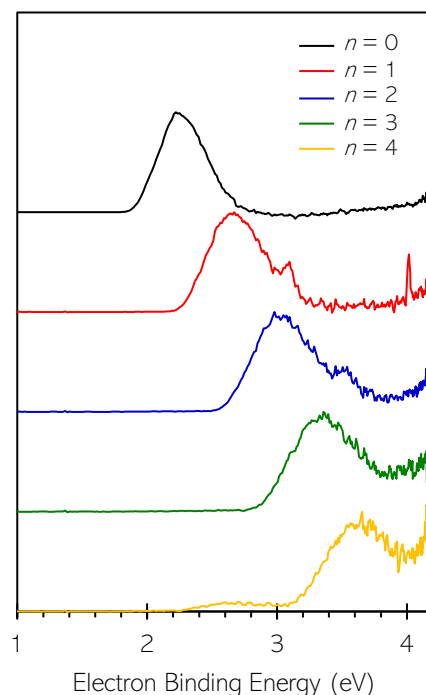
Figure 5.2.3: Photoelectron spectra of pBQ$^-$·(H$_2$O)$_n$, n = 0-4, which have been measured at hv = 4.20 eV. Each PE spectrum has been normalised to its total signal intensity.

It could be argued that the effect of microhydration on the resonances of pBQ$^-$ may not be fully captured through the addition of a single water molecule. Therefore, PE spectra were also obtained for pBQ$^-$·(H$_2$O)$_n$, n = 0-4. The spectra, which are presented in Figure 5.2.3, were measured at a single photon energy of 4.20 eV and are plotted as a function of electron binding energy (eBE = hv – eKE).

For n = 0, the photoelectron spectrum contains a Gaussian-like feature centred on eBE = 2.2 eV, which corresponds to a direct detachment channel. Also featured in the spectrum is a high energy peak at eBE = 4.2 eV. This peak comes about from the formation of the triplet state of neutral pBQ (it is *not* a thermionic detachment feature as it is in n > 0). At first glance, the spectral signatures produced by complexation of pBQ$^-$ with successive water molecules appear very similar to the n = 0 case, containing both the indirect and direct detachment features mentioned. However, a noticeable difference between the spectra is the successive shift in energy of the direct detachment band as the size of the complex increases. Given the relationship been eBE and eKE, the consecutive shift to higher binding energy corresponds to a red shift in terms of eKE, such as that observed between n = 0 and 1 at the lower photon energy probed in Figure 5.2.3. The adiabatic and vertical detachment energies can be

96

ascertained from the onset and peak maximum and are therefore reflective of the shift to higher binding energy (Figure 5.2.4). The detachment energies extracted for isolated pBQ$^-$ have an error of ± 0.02 eV and have been determined using the methods outlined in Section 2.3.3. The error associated with the adiabatic and vertical detachment energies of the hydrated clusters is ± 0.1 eV and has been determined by visual inspection in a similar fashion to that of the larger $(p$BQ$)_n^-$ clusters in Chapter 5.1.
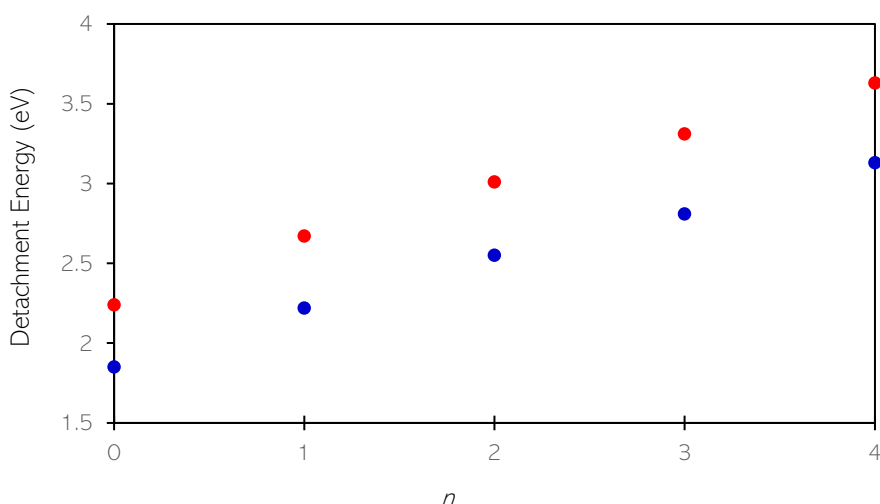

Figure 5.2.4: The trend in adiabatic (blue) and vertical (red) detachment energies of pBQ$^-\cdot$(H$_2$O)$_n$ with increasing number of waters, n.

Appearing in the spectrum of $n = 1$ are additional peaks present at eKE = 3.1 and 4.0 eV. The width of these peaks is significantly narrower than the direct detachment band, suggesting that they arise due to photodetachment from an atomic species. The peaks can be attributed to iodide impurities present in the instrument (used for calibration purposes). Given the small difference in the masses of atomic iodide, I$^-$ and pBQ$^-\cdot$H$_2$O (0.8 g mol^{-1}), mass selection of the desired complex can also result in the unintended irradiation of the iodide species. In this case, photoejection of an electron from I$^-$ results in the reformation of the neutral spin orbit states of iodine, ^{2}P$_{3/2}$ and ^{2}P$_{1/2}$ via direct detachment, giving rise to the respective peaks at eKE = 3.1 and 4.0 eV.

A similar situation arises in the $n = 2$ spectrum, in which an additional peak can be identified at 3.5 eV, on the rising edge of the direct detachment band of pBQ$^-\cdot$(H$_2$O)$_2$. The presence of iodide in the experiment allows for the complexation of I$^-$ with H$_2$O, *i.e.* I$^-\cdot$H$_2$O. Once again, the similar masses of the two hydrated species (pBQ$^-\cdot$(H$_2$O)$_2$ and I$^-\cdot$H$_2$O) can lead to the mass selection and irradiation of both complexes. At 4.2 eV, photodetachment from

I⁻·H₂O proceeds by direct detachment to the neutral, producing the corresponding peak at 3.5 eV. The $n = 3$ and 4 spectra appear to be unaffected by iodide impurities. For pBQ⁻·(H₂O)₄, a broad feature of relatively low intensity is present at ~2.6 eV, which we attribute to photodetachment from an impurity other than pBQ⁻·(H₂O)₄, although the specific chemical identify of the species is unknown.

5.3 GENERAL CONCLUSIONS

In summary, we have presented the photoelectron spectroscopy of p-benzoquinone cluster anions, $(p\text{BQ})_n^-$, with $n = 1 - 4$ at $hv \approx 4.00$ eV together with calculations aimed at identifying possible structures. The spectra reveal that the vertical detachment energy of the clusters increase incrementally by ~ 0.4 eV, which can be explained in terms of the cohesion energy of the cluster. Electronic structure calculations identify the most probable structure for $(p\text{BQ})_2^-$, while for $(p\text{BQ})_3^-$, a number of structures are possible and will likely contribute to the spectrum. The predicted structures are consistent with those calculated for related quinone clusters. For all clusters, thermionic emission is observed suggesting that resonances are excited at $hv = 4.00$ eV, leading to the formation of ground state anions with large amounts of excess energy. For $n = 3$ and 4, fragmentation is additionally observed in the spectra with signatures of photodetachment from the monomer anion for $n = 3$ and the monomer and dimer anions for $n = 4$. Our results show the complex dynamics occurring in these relatively simple clusters, despite the accessed excited states lying energetically in the detachment continuum.

Furthermore, the frequency-resolved 2D photoelectron spectrum of isolated anionic p-benzoquinone has been presented alongside that of its monohydrated complex, pBQ⁻·H₂O at $2.3 \leq hv \leq 4.0$ eV. Comparison of the spectra show few differences, including in the energetic location of the ^2A_u and $^2B_{3u}$ resonances, which are relatively unperturbed by microhydration. A notable area of difference is found in the dynamics of pBQ⁻·H₂O. While the spectral properties of both complexes are suggestive of thermionic emission, the increased intensity of this indirect detachment process and subsequent ground state recovery indicates the enhanced performance of pBQ as an electron acceptor when hydrated. PE spectra were also measured for pBQ⁻·(H₂O)$_n$, $n = 0$-4 at 4.2 eV and display strikingly similar spectral profiles, with direct detachment and thermionic emission observed for all clusters. The successive shift in ADE is reflective of the increased binding present between water molecules and pBQ⁻.

5.4 REFERENCES

(1)   Nohl, H.; Jordan, W.; Youngman, R. J. Quinones in Biology: Functions in Electron Transfer and Oxygen Activation. *Adv. Free Radic. Biol. Med.* **1986**, *2* (1), 211–279.

(2)   El-Najjar, N.; Gali-Muhtasib, H.; Ketola, R. A.; Vuorela, P.; Urtti, A.; Vuorela, H. The Chemical and Biological Activities of Quinones: Overview and Implications in Analytical Detection. *Phytochem. Rev.* **2011**, *10* (3), 353.

(3)   Fukuzumi, S. Bioinspired Electron-Transfer Systems and Applications. *Bull. Chem. Soc. Jpn.* **2006**, *79* (2), 177–195.

(4)   Minteer, S. D.; Giroud, F.; Milton, R. D.; Tan, B. Quinone Electrochemistry: From the Electron Transport Chain to Electron Mediators and Orientational Moieites. *Meet. Abstr.* **2015**, *MA2015-01* (45), 2307–2307.

(5)   Abraham, I.; Joshi, R.; Pardasani, P.; Pardasani, R. T. Recent Advances in 1,4-Benzoquinone Chemistry. *J. Braz. Chem. Soc.* **2011**, *22*, 385–421.

(6)   Stockett, M. H.; Nielsen, S. B. Transition Energies of Benzoquinone Anions Are Immune to Symmetry Breaking by a Single Water Molecule. *Phys. Chem. Chem. Phys.* **2016**, *18* (10), 6996–7000.

(7)   Honda, Y.; Hada, M.; Ehara, M.; Nakatsuji, H. Excited and Ionized States of *p*-Benzoquinone and Its Anion Radical: SAC-CI Theoretical Study. *J. Phys. Chem. A* **2002**, *106* (15), 3838–3849.

(8)   Schiedt, J.; Weinkauf, R. Resonant Photodetachment via Shape and Feshbach Resonances: *p*-Benzoquinone Anions as a Model System. *J. Chem. Phys.* **1998**, *110* (1), 304–314.

(9)   West, C. W.; Bull, J. N.; Antonkov, E.; Verlet, J. R. R. Anion Resonances of *para*-Benzoquinone Probed by Frequency-Resolved Photoelectron Imaging. *J. Phys. Chem. A* **2014**, *118* (48), 11346–11354.

(10)   Allan, M. Time-Resolved Electron-Energy-Loss Spectroscopy Study of the Long-Lifetime *p*-Benzoquinone Negative Ion. *Chem. Phys.* **1983**, *81* (1), 235–241.

(11)   Allan, M. Vibrational and Electronic Excitation in *p*-Benzoquinone by Electron Impact. *Chem. Phys.* **1984**, *84* (2), 311–319.

(12)   Cooper, C. D.; Naff, W. T.; Compton, R. N. Negative Ion Properties of *p*-Benzoquinone: Electron Affinity and Compound States. *J. Chem. Phys.* **1975**, *63* (6), 2752–2757.

(13) Christophorou, L. G.; Carter, J. G.; Christodoulides, A. A. Long-Lived Parent Negative Ions in *p*-Benzoquinone Formed by Electron Capture in the Field of the Ground and Excited States. *Chem. Phys. Lett.* **1969**, *3* (4), 237–240.

(14) Collins, P. M.; Christophorou, L. G.; Chaney, E. L.; Carter, J. G. Energy Dependence of the Electron Attachment Cross Section and the Transient Negative Ion Lifetime for *p*-Benzoquinone and 1,4-Naphthoquinone. *Chem. Phys. Lett.* **1970**, *4* (10), 646–650.

(15) Strode, K. S.; Grimsrud, E. P. Photon-Induced Electron Attachment and Electron Detachment Chemistry of *p*-Benzoquinone and Its Methylated Derivatives. *Chem. Phys. Lett.* **1994**, *229* (4), 551–558.

(16) Modelli, A.; Burrow, P. D. Electron Transmission Study of the Negative Ion States of *p*-Benzoquinone, Benzaldehyde, and Related Molecules. *J. Phys. Chem.* **1984**, *88* (16), 3550–3554.

(17) Gordon, R. L.; Sieglaff, D. R.; Rutherford, G. H.; Stricklett, K. L. Optically Enhanced Electron Attachment by *p*-Benzoquinone. *Int. J. Mass Spectrom. Ion Process.* **1997**, *164* (3), 177–191.

(18) Pshenichnyuk, S. A.; Lomakin, G. S.; Fokin, A. I.; Pshenichnyuk, I. A.; Asfandiarov, N. L. Temperature Dependence of the Mean Autodetachment Lifetime of the *p*-Benzoquinone Molecular Radical Anion. *Rapid Commun. Mass Spectrom. RCM* **2006**, *20* (3), 383–386.

(19) Asfandiarov, N. L.; Pshenichnyuk, S. A.; Fokin, A. I.; Nafikova, E. P. Temperature Dependence of Mean Autodetachment Lifetime of Molecular Negative Ion of *p*-Benzoquinone Molecule. *Chem. Phys.* **2004**, *298*, 263–266.

(20) El Ghazaly, M. O. A.; Svendsen, A.; Bluhme, H.; Nielsen, S. B.; Andersen, L. H. Electron Scattering on *p*-Benzoquinone Anions. *Chem. Phys. Lett.* **2005**, *405* (4), 278–281.

(21) Lozano, A. I.; Oller, J. C.; Jones, D. B.; Costa, R. F. da; Varella, M. T. D. N.; Bettega, M. H. F.; Silva, F. F. da; Limão-Vieira, P.; Lima, M. A. P.; White, R. D.; Brunger, M. J.; Blanco, F.; Muñoz, A.; García, G. Total Electron Scattering Cross Sections from p*ara*-Benzoquinone in the Energy Range 1–200 eV. *Phys. Chem. Chem. Phys.* **2018**, *20* (34), 22368–22378.

(22) Mensa-Bonsu, G.; Lietard, A.; Verlet, J. R. R. Enhancement of Electron Accepting Ability of *para*-Benzoquinone by a Single Water Molecule. *Phys. Chem. Chem. Phys.* **2019**, *21*, 21689–21692.

(23) Fu, Q.; Yang, J.; Wang, X.-B. On the Electronic Structures and Electron Affinities of the M-Benzoquinone (BQ) Diradical and the *o-*, *p*-BQ Molecules: A Synergetic Photoelectron Spectroscopic and Theoretical Study. *J. Phys. Chem. A* **2011**, *115* (15), 3201–3207.

(24) Comita, P. B.; Brauman, J. I. Photodissociation Spectroscopy of the Negative Ion Dimer of Toluquinone. *J. Am. Chem. Soc.* **1987**, *109* (25), 7591–7597.

(25) Marks, J.; Comita, P. B.; Brauman, J. I. Threshold Resonances in Electron Photodetachment Spectra. Structural Evidence for Dipole-Supported States. *J. Am. Chem. Soc.* **1985**, *107* (12), 3718–3719.

(26) Weber, J.; Malsch, K.; Hohlneicher, G. Excited Electronic States of *p*-Benzoquinone. *Chem. Phys.* **2001**, *264* (3), 275–318.

(27) Pou-Amérigo, R.; Serrano-Andrés, L.; Merchán, M.; Ortí, E.; Forsberg, N. A Theoretical Determination of the Low-Lying Electronic States of the *p*-Benzosemiquinone Radical Anion. *J. Am. Chem. Soc.* **2000**, *122* (25), 6067–6077.

(28) Kunitsa, A. A.; Bravaya, K. B. First-Principles Calculations of the Energy and Width of the ^2A_u Shape Resonance in *p*-Benzoquinone: A Gateway State for Electron Transfer. *J. Phys. Chem. Lett.* **2015**, *6* (6), 1053–1058.

(29) Loupas, A.; Gorfinkiel, J. D. Resonances in Low-Energy Electron Scattering from *para*-Benzoquinone. *Phys. Chem. Chem. Phys.* **2017**, *19* (28), 18252–18261.

(30) Kunitsa, A. A.; Bravaya, K. B. Electronic Structure of the *para*-Benzoquinone Radical Anion Revisited. *Phys. Chem. Chem. Phys.* **2016**, *18* (5), 3454–3462.

(31) da Costa, R. F.; Ruivo, J. C.; Kossoski, F.; Varella, M. T. D. N.; Bettega, M. H. F.; Jones, D. B.; Brunger, M. J.; Lima, M. A. P. An *Ab Initio* Investigation for Elastic and Electronically Inelastic Electron Scattering from *para*-Benzoquinone. *J. Chem. Phys.* **2018**, *149* (17), 174308.

(32) Hayashi, N.; Yoshikawa, T.; Ohnuma, T.; Higuchi, H.; Sako, K.; Uekusa, H. Synthesis, Structure, and Properties of Benzoquinone Dimer and Trimers Bearing *t*-Bu Substituents. *Org. Lett.* **2007**, *9* (26), 5417–5420.

(33) O'Malley, P. J. A Density Functional Study of the Effect of Reduction on the Geometry and Electron Affinity of Hydrogen Bonded 1,4-Benzoquinone. Implications for Quinone Reduction and Protonation in Photosynthetic Reaction Centres. *Chem. Phys. Lett.* **1997**, *274* (1), 251–254.

(34) Anstöter, C. S.; Bull, J. N.; Verlet, J. R. R. Ultrafast Dynamics of Temporary Anions Probed through the Prism of Photodetachment. *Int. Rev. Phys. Chem.* **2016**, *35* (4), 509–538.

(35) Horke, D. A.; Li, Q.; Blancafort, L.; Verlet, J. R. R. Ultrafast Above-Threshold Dynamics of the Radical Anion of a Prototypical Quinone Electron-Acceptor. *Nat. Chem.* **2013**, *5*, 711.

(36) Cheng, H.-Y.; Huang, Y.-S. Temporary Anion States of *p*-Benzoquinone: Shape and Core-Excited Resonances. *Phys. Chem. Chem. Phys.* **2014**, *16* (47), 26306–26313.

(37) Bull, J. N.; Verlet, J. R. R. Dynamics of π*-Resonances in Anionic Clusters of *para*-Toluquinone. *Phys. Chem. Chem. Phys.* **2017**, *19* (39), 26589–26595.

(38) Bull, J. N.; Verlet, J. R. R. Observation and Ultrafast Dynamics of a Nonvalence Correlation-Bound State of an Anion. *Sci. Adv.* **2017**, *3* (5), e1603106.

(39) Young, D. *Computational Chemistry: A Practical Guide for Applying Techniques to Real World Problems*; John Wiley & Sons: New York, **2002**.

(40) Vanommeslaeghe, K.; Guvench, O. Molecular Mechanics. *Curr. Pharm. Des.* **2014**, *20* (20), 3281–3292.

(41) Gund, T. 3 - Molecular Modeling of Small Molecules. In *Guidebook on Molecular Modeling in Drug Design*; Cohen, N. C., Ed.; Academic Press: San Diego, **1996**; pp 55–92.

(42) Molecular Mechanics. In *Computational Chemistry: Introduction to the Theory and Applications of Molecular and Quantum Mechanics*; Lewars, E., Ed.; Springer US: Boston, MA, **2003**; pp 43–79.

(43) Kostal, J. Chapter Four - Computational Chemistry in Predictive Toxicology: Status Quo et Quo Vadis? In *Advances in Molecular Toxicology*; Fishbein, J. C., Heilman, J. M., Eds.; Elsevier, **2016**; Vol. 10, pp 139–186.

(44) Case, D. A.; Cheatham, T. E.; Darden, T.; Gohlke, H.; Luo, R.; Merz, K. M.; Onufriev, A.; Simmerling, C.; Wang, B.; Woods, R. J. The Amber Biomolecular Simulation Programs. *J. Comput. Chem.* **2005**, *26* (16), 1668–1688.

(45) Wang, J.; Wolf, R. M.; Caldwell, J. W.; Kollman, P. A.; Case, D. A. Development and Testing of a General Amber Force Field. *J. Comput. Chem.* **2004**, *25* (9), 1157–1174.

(46) Chai, J.-D.; Head-Gordon, M. Long-Range Corrected Hybrid Density Functionals with Damped Atom-Atom Dispersion Corrections. *Phys. Chem. Chem. Phys.* **2008**, *10* (44), 6615–6620.

(47) Ditchfield, R.; Hehre, W. J.; Pople, J. A. Self-Consistent Molecular-Orbital Methods. IX. An Extended Gaussian-Type Basis for Molecular-Orbital Studies of Organic Molecules. *J. Chem. Phys.* **1971**, *54* (2), 724–728.

(48) Campbell, E. E. B.; Ulmer, G.; Hertel, I. V. Delayed Ionization of C_{60} and C_{70}. *Phys. Rev. Lett.* **1991**, *67* (15), 1986–1988.

(49) Amrein, A.; Simpson, R.; Hackett, P. Delayed Ionization Following Photoexcitation of Small Clusters of Refractory Elements: Nanofilaments. *J. Chem. Phys.* **1991**, *94* (6), 4663–4664.

(50) Richardson, O. W. *On the Negative Radiation from Hot Platinum*; Proceedings of the Cambridge Philosophical Society, **1901**; Vol. 11.

(51) Cohen, A. J.; Mori-Sánchez, P.; Yang, W. Insights into Current Limitations of Density Functional Theory. *Science* **2008**, *321* (5890), 792–794.

(52) Hait, D.; Head-Gordon, M. Delocalization Errors in Density Functional Theory Are Essentially Quadratic in Fractional Occupation Number. *J. Phys. Chem. Lett.* **2018**, *9* (21), 6280–6288.

(53) Sigfridsson, E.; Ryde, U. Comparison of methods for deriving atomic charges from the electrostatic potential and moments. *J. Comput. Chem.* **1998**, *19* (4), 377–395.

(54) Cramer, C. J. *Essentials of Computational Chemistry: Theories and Models*; John Wiley & Sons, **2013**.

(55) Boys, S. F.; Bernardi, F. The Calculation of Small Molecular Interactions by the Differences of Separate Total Energies. Some Procedures with Reduced Errors. *Mol. Phys.* **1970**, *19* (4), 553–566.

(56) Mayer, I. Towards a "Chemical" Hamiltonian. *Int. J. Quantum Chem.* **1983**, *23* (2), 341–363.

(57) Kieninger, M.; Suhai, S.; Mayer, I. The Chemical Hamiltonian Approach in Density Functional Theory. *Chem. Phys. Lett.* **1994**, *230* (6), 485–490.

(58) Bull, J. N.; West, C. W.; Verlet, J. R. R. Ultrafast Dynamics of Formation and Autodetachment of a Dipole-Bound State in an Open-Shell π-Stacked Dimer Anion. *Chem. Sci.* **2016**, *7* (8), 5352–5361.

(59) Anstöter, C. S.; Gartmann, T. E.; Stanley, L. H.; Bochenkova, A. V.; Verlet, J. R. R. Electronic Structure of the Para-Dinitrobenzene Radical Anion: A Combined 2D Photoelectron Imaging and Computational Study. *Phys. Chem. Chem. Phys.* **2018**, *20* (37), 24019–24026.

(60) Schulz, G. J. Resonances in Electron Impact on Diatomic Molecules. *Rev. Mod. Phys.* **1973**, *45* (3), 423–486.

(61) Hotop, H.; Ruf, M.-W.; Allan, M.; Fabrikant, I. I. Resonance and Threshold Phenomena in Low-Energy Electron Collisions with Molecules and Clusters. In *Advances In Atomic, Molecular, and Optical Physics*; Bederson, B., Walther, H., Eds.; Academic Press, **2003**; Vol. 49, pp 85–216.

(62) Jordan, K. D.; Burrow, P. D. Temporary Anion States of Polyatomic Hydrocarbons. *Chem. Rev.* **1987**, *87* (3), 557–588.

(63) Fabrikant, I. I.; Eden, S.; Mason, N. J.; Fedor, J. Chapter Nine - Recent Progress in Dissociative Electron Attachment: From Diatomics to Biomolecules. In *Advances In Atomic, Molecular, and Optical Physics*; Arimondo, E., Lin, C. C., Yelin, S. F., Eds.; Academic Press, **2017**; Vol. 66, pp 545–657.

(64) Chaplin, M. Do We Underestimate the Importance of Water in Cell Biology? *Nat. Rev. Mol. Cell Biol.* **2006**, *7* (11), 861–866.

(65) Becke, A. D. Density-functional Thermochemistry. III. The Role of Exact Exchange. *J. Chem. Phys.* **1993**, *98* (7), 5648–5652.

(66) Krishnan, R.; Binkley, J. S.; Seeger, R.; Pople, J. A. Self-consistent Molecular Orbital Methods. XX. A Basis Set for Correlated Wave Functions. *J. Chem. Phys.* **1980**, *72* (1), 650–654.

(67) Campbell, E. E. B.; Levine, R. D. Delayed Ionization and Fragmentation En Route to Thermionic Emission: Statistics and Dynamics. *Annu. Rev. Phys. Chem.* **2000**, *51* (1), 65–98.

(68) Sieradzka, A.; Gorfinkiel, J. D. Theoretical Study of Resonance Formation in Microhydrated Molecules. I. Pyridine-$(H_2O)_n$, n = 1,2,3,5. *J. Chem. Phys.* **2017**, *147* (3), 034302.

(69) Sieradzka, A.; Gorfinkiel, J. D. Theoretical Study of Resonance Formation in Microhydrated Molecules. II. Thymine-$(H_2O)_n$, n = 1,2,3,5. *J. Chem. Phys.* **2017**, *147* (3), 034303.

(70) West, C. W.; Bull, J. N.; Verlet, J. R. R. Charged Particle Imaging of the Deprotonated Octatrienoic Acid Anion: Evidence for a Photoinduced Cyclization Reaction. *J. Phys. Chem. Lett.* **2016**, *7* (22), 4635–4640.

(71) Bull, J. N.; West, C. W.; Verlet, J. R. R. On the Formation of Anions: Frequency-, Angle- , and Time-Resolved Photoelectron Imaging of the Menadione Radical Anion. *Chem. Sci.* **2015**, *6* (2), 1578–1589.

(72) Tan, E. M. M.; Hilbers, M.; Buma, W. J. Excited-State Dynamics of Isolated and Microsolvated Cinnamate-Based UV-B Sunscreens. *J. Phys. Chem. Lett.* **2014**, *5* (14), 2464–2468.

(73)   Jordan, K. D.; Wang, F. Theory of Dipole-Bound Anions. *Annu. Rev. Phys. Chem.* **2003**, *54* (1), 367–396.

(74)   Fermi, E.; Teller, E. The Capture of Negative Mesotrons in Matter. *Phys. Rev.* **1947**, *72* (5), 399–408.

(75)   Simons, J. Molecular Anions. *J. Phys. Chem. A* **2008**, *112* (29), 6401–6511.

CHAPTER 6

PHOTOELECTRON SPECTROSCOPIC STUDY OF $I^- \cdot ICF_3$: A FRONTSIDE ATTACK S_N2 PRE-REACTION COMPLEX

2D photoelectron imaging has been applied to a reactive organic system, $I^- \cdot ICF_3$ to characterise its photophysical spectroscopic properties. Photoelectron and photodetachment spectra are presented alongside electronic structure calculations. These show that I^- is located at the iodine side of CF_3I. The spectroscopy and electronic structure of $I^- \cdot CF_3I$ has been compared to the well-studied S_N2 pre-reaction complex $I^- \cdot CH_3I$ and display striking similarities despite a reversal in the stereodynamics (*i.e.* inversion of the CX_3 between $X = H$ and F) of the S_N2 reaction. This chapter is based on the following publication:

6.1 INTRODUCTION

Bimolecular nucleophilic substitution (S_N2) reactions represent a cornerstone of reactivity in organic chemistry.[1] In its simplest form, the reaction $X^- + CH_3Y \rightarrow XCH_3 + Y^-$ involves the text-book $[X \cdots CH_3 \cdots Y]^-$ activated complex, where X^- attacks CH_3Y from the backside (see Section 1.1.1). The stereodynamics of the reaction are expected from the long-range charge—dipole-moment interaction between X^- and CH_3Y. While, in the solution phase, this long-range interaction is screened, the isolated view of the reaction remains mostly valid.[2–4] As a result, there have been many studies of S_N2 reaction dynamics in the gas-phase, which have provided exquisite insight into the reaction mechanisms over many years.[5–8] While the indirect, backside attack mechanism has been researched in-depth, contemporary experimental and computational studies have explored alternative mechanistic pathways of the S_N2 reaction.[9–12] For example, recent crossed molecular beam studies and atomistic molecular dynamics simulations have shown how the dynamics of the reaction are sensitive to the leaving group, with differing mechanisms contributing when Y is changed.[9] Additionally, photoelectron (PE) spectroscopy of the pre-reaction complex, $X^- \cdots CH_3Y$, can provide much insight into the entrance channel of the reaction, which often plays a deterministic role in the reaction.[13,14] However, in PE spectroscopy experiments, it has not been possible to control the stereodynamics of the pre-reaction complex. Hence, only the backside attack (direct rebound) mechanism has been probed. In the present study, we make a chemical substitution of the methyl H-atoms to F-atoms. As the H atoms are mostly indirectly involved in the S_N2 reaction, the main reaction coordinate along the X–C–Y bond is preserved.[1] However, this chemical substitution reverses the stereodynamics of the reactions and allows us to perform PE spectroscopy of the pre-reaction complex for the frontside attack (along the X–Y–C coordinate).

The gas-phase S_N2 reaction has been studied extensively by the groups of Wester and Hase;[8,10,15–17] they have recently observed that the replacement of the leaving group, Y, from Cl to I in the S_N2 reaction, $F^- + CH_3Y$, has dramatic effects on the reaction dynamics.[9] Specifically, for Y = Cl, the dominant reaction mechanism is the classic direct rebound mechanism (at energies >0.6 eV).[9,18–20] In contrast, a significant fraction of reactions for the Y = I reaction could be attributed to a direct stripping mechanism, especially at high impact parameters, where F^- attacks the methyl group and leads to the product ion leaving along the initial direction of the CH_3Y reactant.[9] Given that the permanent dipole moments of CH_3Cl and CH_3I are not that different ($\mu = 1.90$ D and $\mu = 1.64$ D, respectively),[21] the change in dynamical

107

orientation of CH_3I was assigned to a stronger interaction between the two halogen atoms in the Y = I reaction (the $F^-\cdots ICH_3$ complex is bound by 0.97 eV, while $F^-\cdots ClCH_3$ is bound by only 0.14 eV).[9] This stronger interaction changes the orientation at short range leading to differing reaction dynamics.

The most studied pre-reaction S_N2 complex using PE spectroscopy has been $I^-\cdots CH_3I$.[13,22–30] Cyr *et al.* employed PE, photodetachment and photofragment spectroscopy to characterise the electronic excited states of $I^-\cdots CH_3I$, which provided evidence of an intra-cluster charge transfer state with I and CH_3I as the respective donor and acceptor species.[22,23,25] Although their studies did not indicate that the S_N2 reaction could be photoinitiated, the knowledge gained of the $I^-\cdots CH_3I$ complex establishes this system as an ideal test-case to make the H to F substitution and to provide insight into the abovementioned molecular beam and molecular dynamics simulation studies. We show that, despite the reversed stereochemistry, similarly strong photoabsorption at threshold is observed for $I^-\cdots CH_3I$ and $I^-\cdots ICF_3$ and many of the spectral features are common to both systems.

It is also noteworthy that $I^-\cdots ICF_3$ is potentially an important species in plasma chemistry. Industrially, plasma etching is widely used to fabricate the fine structural components of microelectronic devices.[31,32] While cations are primarily considered in plasmas, anions are also present and contribute to the chemical cocktail.[33] The most common process gases for plasma etching include CF_4 and CF_3H.[32,34] However, these are long-lived global-warming gases necessitating a reduction in their usage.[35] Alternatives such as CF_3I, which has a relatively low global-warming potential,[36–39] have been shown to have similar etching rates to standard mixtures.[36,40] However, much less is known about the composition of these plasmas.[41] Dissociative electron attachment to CF_3I forms I^- in high yield,[42] which may go on to complex to the abundant CF_3I process gas to form species such as $I^-\cdots ICF_3$. Hence, these species may be common chemical species in the plasma mix. However, they have yet to be studied. The present work shows that $I^-\cdots ICF_3$ has a large electron affinity and is strongly bound. This suggests that such species may indeed play a role in plasma chemistry.

6.2 EXPERIMENTAL & COMPUTATIONAL METHODS

As the experimental setup has been described in detail in Chapter 2, only a brief overview is given here. To generate $I^-\cdots ICF_3$, a CF_3I/Ar mix was expanded through a pulsed valve into vacuum.[43] The supersonic expansion was intersected by an electron beam near the

throat of the expansion, generating an electron rich plasma in the high molecular density region. The subsequent expansion and associated cooling provide a snapshot of the species formed in the plasma.[44] Time-of-flight spectrometry showed that the dominant species formed were I^- (which is to be expected from the dissociative electron attachment to CF_3I) together with $I^-\cdots ICF_3$, formed presumably by the condensation of a CF_3I molecule onto I^- because of the long-range charge–dipole interaction. We also observed larger clusters with the chemical formula $I^-(CF_3I)_n$. The mass-selected $I^-\cdots ICF_3$ ions were crossed by nanosecond laser pulses and the resulting photoelectrons were imaged using a velocity map imaging spectrometer.

Density functional theory (DFT) and time-dependent DFT (TDDFT) calculations were performed to provide a qualitative interpretation of the experimental results and a basic understanding of the electronic structure of $I^-\cdots ICF_3$.[45,46] For comparative purposes, calculations were also performed on $I^-\cdots CH_3I$. As discussed in Chapter 3.6, many approximate exchange–correlation functionals suffer from formal problems for anions (namely positive highest occupied molecular orbital energies), but this can be unproblematic in practical calculations if a long-range corrected functional is used.[47–49] In the present study, all reported theoretical results were determined using the CAM-B3LYP range-separated exchange-correlation functional.[47] This functional also contains the relevant physics for describing long-range and charge-transfer excitations, which are relevant to the systems considered.[50] In comparison to the previous computational studies detailed in this thesis, a significantly larger Pople basis set has been employed here – 6-311++G**. The use of this basis set is appropriate given the relatively small size of the systems under study. The inclusion of diffuse and polarisation functions is necessary to describe the bonding interactions and anionic nature of the molecules under study. The 6-311++G** basis set was used on C, F, and H atoms but has not been parameterised for use on heavier atoms.[51–53] As such an alternative basis set, LANL2DZdp was employed in calculations for the I atoms.[54–56] In this basis set, functions describing core electrons are replaced by an effective core potential (LANL2), which reduces the computational cost associated with the calculation of larger systems. Valence electrons, (*i.e.* 5s and 5p electrons in the case of iodine) are treated using the D95 basis set to which polarisation and diffuse functions have been added.

The calculated ground state optimised geometries were verified to be minima by vibrational analysis and TDDFT calculations were performed at the optimised geometries. We note that our calculations do not include spin-orbit interactions. For iodine, this is of course a major omission – the iodine spin-orbit splitting in the two ^2P_J states of iodine is 0.94 eV – and

this is not quantitatively reflected in the present calculations. Nevertheless, the calculations provide a useful qualitative basis to assist the interpretation of the experimental results.

6.3   RESULTS & ANALYSIS

To determine the ground state geometries, optimisations were performed commencing from frontside and backside (regular S_N2) conformations. The lowest energy structure of $I^-\cdots ICF_3$ has C_{3v} symmetry, with I–I and I–C bond lengths of 3.33 and 2.18 Å, respectively (see Figure 6.1). In contrast to $I^-\cdots CH_3I$, the perfluorinated $I^-\cdots ICF_3$ molecule has the I^- atom residing on the side of iodine, *i.e.* frontside attack. We have verified that this frontside structure is also obtained when a D3 dispersion correction is introduced or when MP2 is used.[57,58] The change in orientation of CX_3I between X = H and F correlates with the reversal in permanent dipole moment between CH_3I and CF_3I.
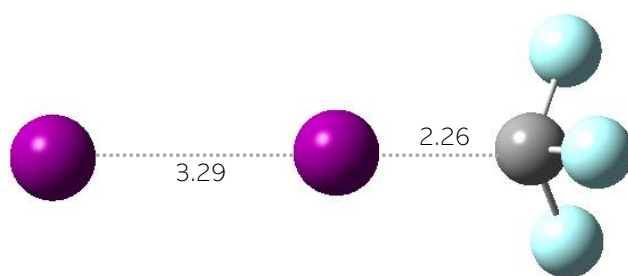

Figure 6.1: Calculated ground state structure of $I^-\cdots ICF_3$. Bond distances are shown in Ångstroms.

The electropositive H atoms lead to a dipole moment $\mu = 1.78$ D in the direction of the I–C bond,[59] while the strongly electronegative F atoms lead to a dipole moment $\mu = 1.28$ D in the antiparallel direction.[60] The dipole moment vector reversal has the interesting consequence that one can still view $I^-\cdots ICF_3$ as a reaction precomplex, but with different stereochemistry, and hence, the spectroscopic signatures may be expected to be different between X = H and F. Figure 6.2 shows the frequency-resolved (2D) PE spectra collected over the $3.50 \leq h\nu \leq 5.50$ eV range with 0.1 eV intervals. 2D PE spectroscopy is a powerful probe of the location and dynamics of anionic resonances,[61] which we have recently applied to radical anions,[62,63] biomolecules[64] and clusters.[65–68] Individual PE spectra are plotted in terms of electron binding energy (eBE = $h\nu$ – eKE) and have been normalised to their maximum intensity. At $h\nu = 3.50$

eV, a narrow peak is visible at eBE = 3.06 eV. The profile and position of this peak indicates that it arises from direct photodetachment from atomic I^- to the neutral iodine $^2P_{3/2}$ ground state. This peak can be clearly identified in the $3.5 \leq hv \leq 3.9$ eV range, although it is also present at higher photon energies (with much reduced intensity). The appearance of the I^- PE spectrum following the excitation of $I^-\cdots ICF_3$ implies that two sequential photons were absorbed during the laser pulse (~ 5 ns).
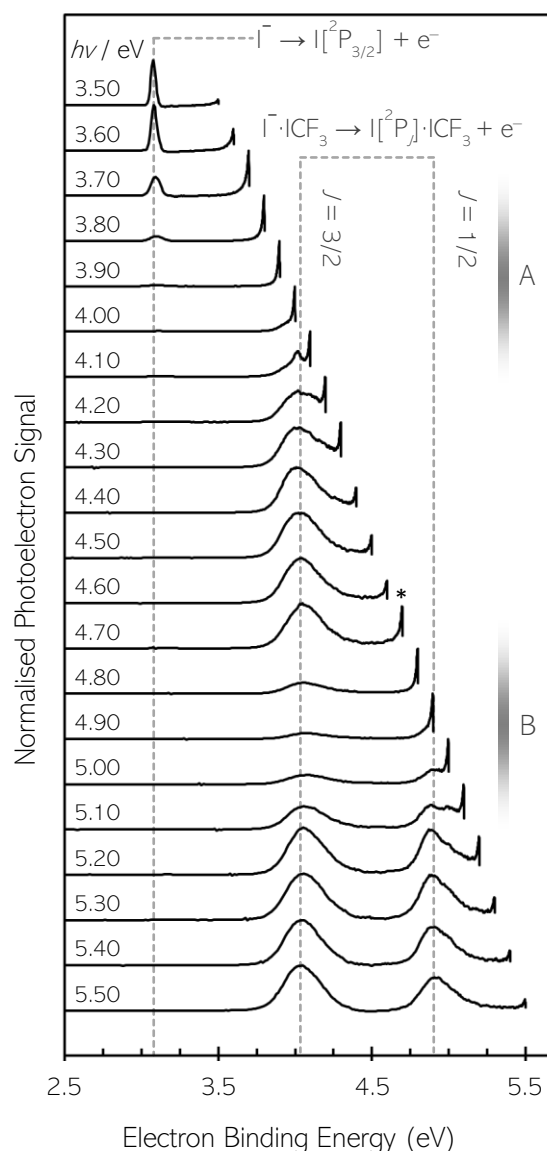

Figure 6.2: 2D photoelectron spectra of $I^-\cdots ICF_3$ in the $3.50 \leq hv \leq 5.50$ eV range with hv indicated on the left of each offset spectrum. The spectra have been normalised to their maximum intensity. Bands are labelled according to their detachment process (see text for details). Bands A and B indicate regions where indirect processes dominate, which are evident from the peak at near zero kinetic energy, which has, for example, been marked with an asterisk in the spectrum at $hv = 4.70$ eV.

At $hv \geq 5.2$ eV, two broad direct detachment features dominate the PE spectrum. The peaks centred around eBE = 4.0 and 4.9 eV have similar spectral shapes and widths. The energy gap between the two features is 0.88 eV, which is close to the spin-orbit splitting in the neutral iodine atom (0.94 eV). We assign these two peaks to the direct detachment from $I^-\cdots ICF_3$, leaving the neutral as $I[^2P_{1/2}]\cdots ICF_3$ and $I[^2P_{3/2}]\cdots ICF_3$ for the high and low eBE peaks, respectively. The vertical detachment energy (VDE) of $I^-\cdots ICF_3$ corresponds to the maximum of the $[^2P_{3/2}]\cdots ICF_3$ peak; VDE = 4.03 ± 0.05 eV (calculated at 4.29 eV). The large spectral width of the peaks (~0.3 eV) and their unresolved vibrational structure could preclude the observation of the $0 \leftarrow 0$ transition between the vibrational levels of the anion and neutral ground states and, thus, also the direct measurement of the adiabatic detachment energy, ADE. Nevertheless, taking the lowest eBE where PE signal becomes visually apparent from the direct detachment of the PE spectra provides a measure of ADE = 3.8 ± 0.1 eV. This is a blue-shift of >0.7 eV compared to unclustered I^-, and much larger than the blue-shift observed in $I^-\cdots CH_3I$ (0.38 eV).[25]

The PE spectra corresponding to the direct detachment from $I^-\cdots ICF_3$ are on the whole unstructured. However, there is evidence of vibrational structure around $hv \sim 4.1$ and 5.1 eV. The $hv = 5.10$ eV PE spectrum, reproduced in Figure 6.3, shows two unresolved peaks superimposed on the broader background peak. The spacing between these two peaks is approximately 100 meV (800 cm^{-1}).
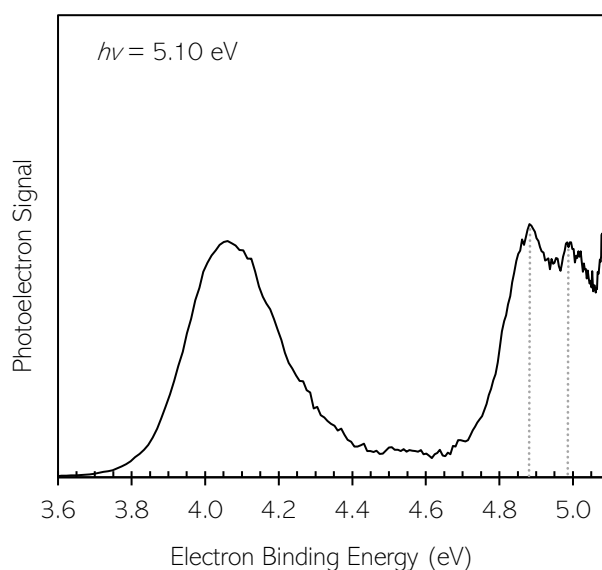

Figure 6.3: Photoelectron spectrum of $I^-\cdots ICF_3$ taken at $hv = 5.10$ eV. The vertical dashed lines indicate the vibrational structure observed.

Additionally, present in virtually all PE spectra is a narrow detachment feature peaking at eBE = hv. As an example, this peak is labelled with an asterisk in the hv = 4.70 eV PE spectrum in Figure 6.2; it is also clearly visible in Figure 6.3. The peak corresponds to the production of PEs with near zero kinetic energy, which is normally associated with an indirect detachment process. Through comparison of the relative intensities of bands present in the PE spectra, the dominant electron loss processes can be identified at each photon energy. With reference to Figure 6.2, regions labelled as A and B contain PE spectra in which the indirect detachment is the dominant electron loss process occurring. Specifically, at $hv \sim 4.0$ eV and 4.9 eV, the fraction of electrons produced *via* the direct detachment channels appears at a minimum.

Region A (and B) led to a noticeable increase in total electron signal as a function of hv. To explore this further, in Figure 6.4, a photodetachment (total electron yield) spectrum is presented in the $3.75 \leq hv \leq 4.15$ eV range. Two main peaks can be identified: a broad feature centred at hv = 3.97 eV, and a second, less prominent feature centred at hv = 4.07 eV. These peaks appear very close to the VDE of the cluster at 4.03 eV (and above the measured ADE = 3.8 eV). For a direct detachment process, a rise in the PE yield is expected when the photon energy passes through threshold, but this is expected to resemble a smooth step function.[69] Here, the observations of peaks in the photodetachment spectrum and the appearance of an indirect process for electron loss (Figure 6.2, spectral regions A and B), point to a photoexcitation of excited states of the cluster close to the detachment threshold.[69] A similar situation appears to be present at the onset of the second detachment threshold corresponding to the $I[^2P_{1/2}]\cdots ICF_3 + e^-$ channel.
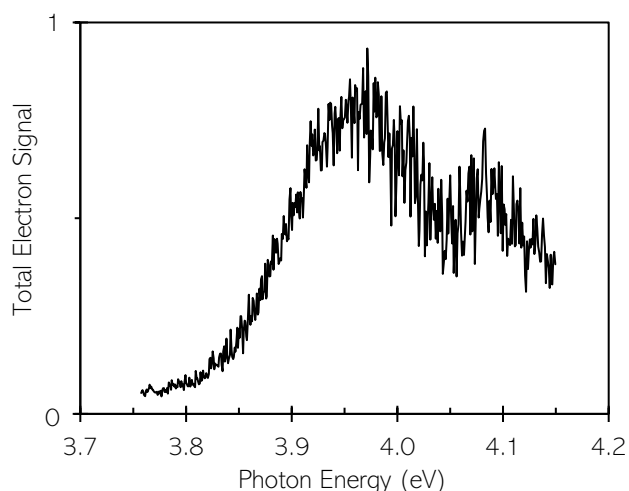

Figure 6.4: Photodetachment spectrum of $I^-\cdots ICF_3$ taken around the onset of the direct detachment from the cluster.

Similar to the dominant indirect detachment processes occurring in regions A and B in the 2D PE spectra (Figure 6.2), the two-photon detachment process at eBE = 3.06 eV is mediated by an electronic excited state. To probe the character of the excited states, DFT and TDDFT calculations were performed.

The relevant molecular orbitals (MOs) of $I^-\cdots ICF_3$ are shown in Figure 6.5. The highest occupied MO (HOMO) corresponds primarily to the non-bonding atomic p-orbital localised on I^- and is doubly-degenerate (*i.e.* the p_x and p_y orbitals – only one of these is shown in Figure 6.5). The next lowest occupied MO, HOMO-2 corresponds to the p_z orbital on I which interacts with CF_3I. As a comparison, the analogous MOs for $I^-\cdots CH_3I$ are also included in Figure 6.5. The overall MO structure of $I^-\cdots CH_3I$ is very similar to that of $I^-\cdots ICF_3$, despite the reversed stereochemistry. However, it is also clear from the occupied MOs that the charge in $I^-\cdots ICF_3$ is more delocalised onto the CF_3I moiety and that $I^-\cdots ICF_3$ has more covalent bonding character than in $I^-\cdots CH_3I$, where the charge is mostly localised on I^-. The lowest unoccupied MO (LUMO) in $I^-\cdots ICF_3$ and $I^-\cdots CH_3I$ are also shown in Figure 6.5.

Electronic excitation energies and their character were computed using TDDFT and the dominant orbital transitions are included in Figure 6.5. For $I^-\cdots ICF_3$, the lowest energy transitions were calculated at 4.04 eV and correspond to the LUMO ← HOMO/HOMO-1. These transitions have a low oscillator strength (0.009). Additionally, a very bright transition corresponding to the transition from LUMO ← HOMO-2, with an oscillator strength of 0.91, was identified in the relevant energy range. This bright state has been calculated at 4.82 eV above the anion ground state.

The excited states of $I^-\cdots CH_3I$ bear close similarities to those of $I^-\cdots ICF_3$. The lowest energy transitions of $I^-\cdots CH_3I$ also corresponds to the degenerate LUMO ← HOMO/HOMO-1 excitation. This transition has a similarly low oscillator strength but is red-shifted by 0.27 eV compared to the analogous transition in $I^-\cdots ICF_3$. The analogous LUMO ← HOMO-2 bright electronic transition is calculated to lie at 3.88 eV (*cf.* 4.82 eV for $I^-\cdots ICF_3$) and has an oscillator strength of 0.33.
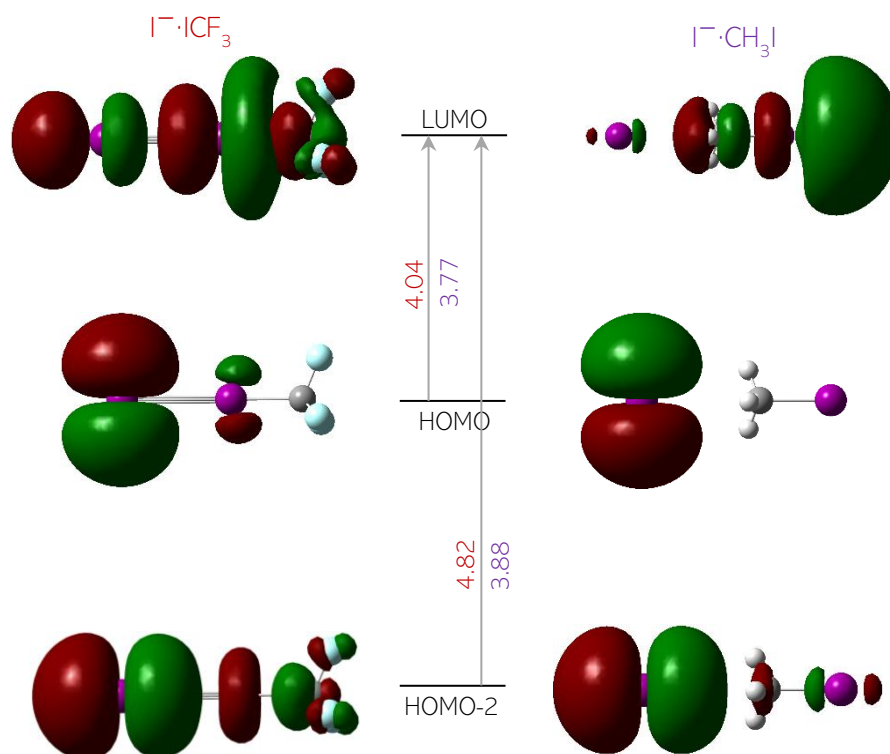
Figure 6.5: A comparison of the LUMO ← HOMO and LUMO ← HOMO-2 transitions of I⁻···ICF₃ and I⁻···CH₃I, respectively. Vertical excitation energies stated are in eV, where the values in red and purple correspond to I⁻···ICF₃ and I⁻···CH₃I, respectively.

6.4 DISCUSSION

The experimental VDE of I⁻···ICF₃ is 4.03 eV, which can be compared to that of the related I⁻···CH₃I anion at 3.42 eV,[23,28] while that of bare I⁻ is 3.06 eV.[70] The 0.36 eV increase in VDE upon clustering I⁻ to CH₃I has previously been attributed to the attractive interaction between the negative charge and the permanent dipole-moment of CH₃I (ignoring any interaction between neutral iodine and CH₃I).[28] This shift increases to 0.97 eV in I⁻···ICF₃ suggesting a significant degree of covalent bonding between I⁻ and ICF₃. This covalent bonding is apparent from the MOs shown in Figure 6.5 and the molecular structure in Figure 6.1 that indicate some I_2^-···CF₃ character to the cluster. The calculated I–I distance in the complex is very similar to that of I_2^- (3.33 Å compared to 3.32 Å calculated at the same level of theory) and also show that the C–I bond in the complex (2.18 Å) is slightly elongated in comparison to CF₃I (2.14 Å). Hence, these observations suggest there is some I_2^- character and a weakening of the bonding interaction across the C–I bond. The covalent nature is also consistent with the increased spectral width of the PE peaks (~300 meV) compared to those

observed in $I^-\cdots CH_3I$, which are on the order of 25 meV. The fact that the spectral shape for direct detachment is mostly Gaussian suggests that the final neutral state has a very different geometry to that of the anion.

Despite the apparent covalent character of the bonding in $I^-\cdots ICF_3$, it also retains much non-covalent character and has many similarities to $I^-\cdots CH_3I$. The degenerate lowest energy transitions are from the relatively non-bonding $p_{x,y}$ orbitals localised on I^-. While this transition carries a very small oscillator strength, its presence is consistent with the PE spectra at hv < 3.9 eV in Figure 6.2. Specifically, photodetachment from I^- can be seen by the narrow PE peak at eBE = 3.06 eV, which presumably comes about from excitation of $I^-\cdots ICF_3$ *via* the bound low-energy excited states that leads to dissociation of the cluster forming I^-. This atomic fragment can subsequently be photodetached in the presence of the laser field which remains present for ~5 ns (FWHM). The PE signal in this range was very small, consistent with the low oscillator strengths of the LUMO ← HOMO/HOMO-1 transition and with the 2 sequential photon process.

For $hv \geq 3.80$ eV, the total PE signal increases sharply. The total PE signal shown in Figure 6.4 has a peak at 3.97 eV. Concomitant to the increase in total PE yield is a change in the appearance of the PE spectrum: the detachment from I^- becomes a very minor channel while most signal appears at very low kinetic energy. This indirect detachment channel indicates that an intermediate excited state is accessed. Given the large increase in PE yield (Figure 6.4), we assign this to the calculated bright electronic transition (LUMO ← HOMO-2). As our calculations do not include spin-orbit coupling, the calculated transition energy is some way off. We do, of course, expect a spin-orbit component and this is clearly seen in Figure 6.2 as a second indirect channel opens up at $hv \sim 4.9$ eV (B in Fig. 6.2).

At $hv = 4.00$ eV, there is a direct detachment peak from $I^-\cdots ICF_3$ and this peak remains present for $hv \geq 4.00$ eV. We conclude that the bright state is very close to threshold. It is approximately 60 meV below the VDE. This also suggests that the total PE yield shown in Figure 6.4 is a convolution of the electron loss *via* the indirect channel and the direct detachment channel. Despite this complication, the second maximum observed at 4.07 eV does not correlate with this onset and appears to be an additional peak in the excitation cross section – *e.g.* a vibrational level of the excited state. The spacing of ~100 meV is very similar to that observed in the PE spectra (see Figure 6.3).

The observation of an excited state near threshold (for both spin-orbit channels) with vibrational structure is similar to observations in $I^-\cdots CH_3I$. In that case, vibrational progressions at 68 meV were observed in both the PE spectra and the photofragment action spectra monitoring I^- loss or electron loss. This vibrational progression was assigned to the v_3 mode (based on the 66 meV frequency for the IR active v_3 mode in CH_3I) and predominantly involves the C–I stretch. In their assessment of the $I^-\cdots CH_3I$ spectroscopy, Johnson and co-workers conclude that the vibrational structure in the PE spectra comes about from non-Franck-Condon effects, *i.e.* non-adiabatic effects such as vibronic coupling where the vibrational modes have altered intensities due to coupling to electronic modes.[28] The non-Franck-Condon behaviour was further supported by the fact that the vibrational activity seen in their PE spectra showed a dependence on the eKE of the outgoing electrons.[28]

Vibrational structure is also observed here in $I^-\cdots ICF_3$ and the vibrations appear more resolved at $hv = 4.2$ and 5.1 eV (see Figures 6.2 and 6.3), where the two spin-orbit thresholds open. In the case of CF_3I, the IR spectrum is dominated by the v_1 and v_2 mode (92 and 134 meV, respectively) of a_1 symmetry, which correspond to the symmetric CF_3 stretch and a C–I stretch (that also involves the CF_3 umbrella mode; this mode is similar to the v_3 mode in CH_3I), respectively. Both these modes are close to the observed ~100 meV spacing in the PE spectrum (Figure 6.3) and the electron yield spectrum (Figure 6.4).

Cyr *et al.* probed the spectroscopy of $I^-\cdots CH_3I$ using electron yield as well as fragmentation action spectra with the two products being I^- and I_2^-. However, the main product is electron loss. In their PE spectra, no slow electrons were observed.[23] This may be because of the low collection efficiency at low eKE in their experiment. Here, we clearly show for $I^-\cdots ICF_3$ that the electrons are lost with a very low eKE. The mechanism ascribed by Johnson and co-workers for the dynamics is one in which the fragmentation can be viewed as an electron-molecule scattering process, leading to dissociation that is mediated by the σ* orbital along the C–I bond. This conclusion is consistent with the excited state calculated in Figure 6.5, where such σ* character is clearly present. In the present case of $I^-\cdots ICF_3$, many analogies can be drawn. By inspection of the MO diagram in Figure 6.5, a similar σ* orbital is excited and an analogous vibrational progression involving the C–I stretch is seen in the PE spectra and photodetachment spectra of $I^-\cdots ICF_3$. Here, we have not been able to monitor atomic or molecular fragments directly and have only observed the electron loss channel. Nevertheless, it would appear that a similar overall mechanism can be ascribed here for $I^-\cdots ICF_3$. The fact that the indirect electrons appear at very low eKE, regardless of the photon energy, may arise

because the electrons are lost along the dissociative coordinate. A similar process was thought to occur in the case of $(pTQ)_2^-$,[66] where the low eKE features present in the 2D PE spectra were attributed to a process initiated by photoexcitation to a dissociative resonance state. As the dissociative state decays along the intermolecular coordinate, a reduced amount of energy is available for autodetachment, which consequently generates a broad distribution of electrons that peaks at low kinetic energy. It would clearly be of interest to perform fragment (probing I^- and I_2^-) action spectra, but these experiments are not possible in our current arrangement.

While the electronic structure of the S_N2 pre-reaction complexes appears little affected, clearly the stereochemistry has inverted. Therefore, $I^-\cdots ICF_3$ effectively serves as a probe for a frontside attack entrance channel complex. As described in the introduction, recent crossed molecular beam experiments and simulations have shown that for the reactions $F^- + CH_3Y$, a change of Y = Cl to I led to an enhanced frontside attack, even though the long-range interactions are similar. Hence, it was suggested that a stronger interaction between F^- and I compared to F^- and Cl was responsible. In the present study, we have effectively trapped a frontside attack pre-reaction complex (with I^- as a reactant) and indeed, a significant covalent bonding character is observed. The binding energy can be roughly estimated from the increase in the VDE of the cluster relative to that of bare iodide. In $I^-\cdots CH_3I$, this is 0.36 eV compared to 0.97 eV for $I^-\cdots ICF_3$. The former is a purely electron-dipole-moment interaction and, assuming that the magnitude of the permanent dipole of CH_3I and CF_3I are similar, then the covalent contribution to the binding is approximately the difference in binding energy of $I^-\cdots CH_3I$ and $I^-\cdots ICF_3$ or ~0.6 eV. Although this is a very rough estimate, it does suggest that the covalent character is stronger than the overall repulsive charge-dipole-moment interaction in $I^-\cdots ICH_3$ (0.36 eV). It would be of interest to study the $F^-\cdots CH_3I$ complex as a more direct comparison to the reaction dynamics studies, where a well depth of 0.97 eV was calculated for $F^-\cdots ICH_3$.[71–73] Overall, given the growing evidence of the existence and contributions of mechanisms other than the traditional backside attack for S_N2 reactions,[10–12] the development of new experimental probes for complexes along such reaction coordinates should prove to be useful in determining energetics and structures of intermediates.

6.5   CONCLUSIONS

A photoelectron (PE) and photodetachment spectroscopic study of the $I^-\cdots ICF_3$ complex is presented, supported by DFT and TDDFT calculations. The binding in the cluster

can be viewed as a combination between a non-covalent charge-dipole interaction and a covalent contribution along the I–I–C bond. The PE spectra show direct detachment channels, leaving the neutral in either spin-orbit states of the anion. The lowest vertical detachment energy is 4.03 eV and the adiabatic energy is approximately 3.8 eV. Near both thresholds, there is clear evidence of excitation to an excited state, which is corroborated by the PE yield spectrum around the first threshold. Electronic structure calculations show that this excited state can be assigned to a transition with charge-transfer character from the iodide to the ICF_3 moiety.

The spectroscopy is compared to the much-studied $I^-\cdots CH_3I$ cluster, which is the pre-reaction complex of the corresponding S_N2 reaction. The electronic structure of $I^-\cdots ICF_3$ shows many parallels, even though the geometric structure is very different because of the reversal of the dipole moment between CH_3I and CF_3I (*i.e.* the pre-reaction complex stereodynamics have been reversed). Specifically, both possess an excited state very close to threshold and show evidence of vibrational structure in the PE and photodetachment spectra. We assign the spectroscopy and excited state dynamics along parallel lines to that of $I^-\cdots CH_3I$: the excited state near threshold can be viewed as an electron scattering state that is strongly coupled to the σ^* orbital on the I–C bond, leading to photoemission and dissociation (which was not measured here). We conclude that the overall electronic excited state structure is insensitive to the stereodynamics of the S_N2 pre-reaction complex.

Chemical dynamics simulations and crossed-beam imaging studies have recently shown that, for the $F^- + CH_3I$ reaction, the reaction is influenced by short-range attraction and often attacks as $F^- + ICH_3$,[9] implying that the covalent interaction of the pre-reaction complex is larger than the long-range electron-dipole interaction. The relatively strong covalent bonding observed between the two iodine atoms here may also be sufficient to overcome the repulsive electron-dipole moment interaction, leading to an attractive well in the frontside attack of the $I^- + CH_3I$ S_N2 reaction. However, this well is weaker than the normal backside orientation as shown by the PE spectroscopy of Johnson and co-workers. In general, the replacement of H atoms with F atoms may serve as a useful general tool to invert the stereodynamics of S_N2 pre-reaction complexes, probe their interactions, and serve as a method for investigating non-traditional S_N2 reaction mechanisms.

6.6   REFERENCES

(1)   Vollhardt, K. P. C.; Schore, N. E. *Organic Chemistry: Structure and Function*, 5th edition.; W. H. Freeman: New York, **2005**.

(2)   Elles, C. G.; Crim, F. F. Connecting Chemical Dynamics in Gases and Liquids. *Annu. Rev. Phys. Chem.* **2006**, *57* (1), 273–302.

(3)   Garver, J. M.; Fang, Y.; Eyet, N.; Villano, S. M.; Bierbaum, V. M.; Westaway, K. C. A Direct Comparison of Reactivity and Mechanism in the Gas Phase and in Solution. *J. Am. Chem. Soc.* **2010**, *132* (11), 3808–3814.

(4)   Orr-Ewing, A. J. Perspective: Bimolecular Chemical Reaction Dynamics in Liquids. *J. Chem. Phys.* **2014**, *140* (9), 090901.

(5)   Hase, W. L. Simulations of Gas-Phase Chemical Reactions: Applications to S_N2 Nucleophilic Substitution. *Science* **1994**, *266* (5187), 998–1002.

(6)   Chabinyc, M. L.; Craig, S. L.; Regan, C. K.; Brauman, J. I. Gas-Phase Ionic Reactions: Dynamics and Mechanism of Nucleophilic Displacements. *Science* **1998**, *279* (5358), 1882–1886.

(7)   Laerdahl, J. K.; Uggerud, E. Gas Phase Nucleophilic Substitution. *Int. J. Mass Spectrom.* **2002**, *214* (3), 277–314.

(8)   Mikosch, J.; Trippel, S.; Eichhorn, C.; Otto, R.; Lourderaj, U.; Zhang, J. X.; Hase, W. L.; Weidemüller, M.; Wester, R. Imaging Nucleophilic Substitution Dynamics. *Science* **2008**, *319* (5860), 183–186.

(9)   Stei, M.; Carrascosa, E.; Kainz, M. A.; Kelkar, A. H.; Meyer, J.; Szabó, I.; Czakó, G.; Wester, R. Influence of the Leaving Group on the Dynamics of a Gas-Phase S_N2 Reaction. *Nat. Chem.* **2016**, *8* (2), 151–156.

(10)   Xie, J.; Otto, R.; Mikosch, J.; Zhang, J.; Wester, R.; Hase, W. L. Identification of Atomic-Level Mechanisms for Gas-Phase $X^- + CH_3Y$ S_N2 Reactions by Combined Experiments and Simulations. *Acc. Chem. Res.* **2014**, *47* (10), 2960–2969.

(11)   Szabó, I.; Czakó, G. Revealing a Double-Inversion Mechanism for the $F^- + CH_3Cl$ S_N2 Reaction. *Nat. Commun.* **2015**, *6*, 5972.

(12)   Xie, J.; Hase, W. L. Organic Chemistry. Rethinking the S_N2 Reaction. *Science* **2016**, *352* (6281), 32–33.

(13)   Dessent, C. E. H.; Johnson, M. A. Photoinitiation of Gas-Phase S_N2 Reactions through the Evans−Polanyi Excited State Surface. *J. Am. Chem. Soc.* **1997**, *119* (21), 5067–5068.

(14)   Dessent, C. E. H.; Kim, J.; Johnson, M. A. Photochemistry of Halide Ion−Molecule Clusters: Dipole-Bound Excited States and the Case for Asymmetric Solvation. *Acc. Chem. Res.* **1998**, *31* (9), 527–534.

(15)   Wester, R.; Bragg, A. E.; Davis, A. V.; Neumark, D. M. Time-Resolved Study of the Symmetric S_N2-Reaction $I^- + CH_3I$. *J. Chem. Phys.* **2003**, *119* (19), 10032–10039.

(16)   Zhang, J.; Mikosch, J.; Trippel, S.; Otto, R.; Weidemüller, M.; Wester, R.; Hase, W. L. $F^- + CH_3I \rightarrow FCH_3 + I^-$ Reaction Dynamics. Nontraditional Atomistic Mechanisms and Formation of a Hydrogen-Bonded Complex. *J. Phys. Chem. Lett.* **2010**, *1* (18), 2747–2752.

(17)   Mikosch, J.; Zhang, J.; Trippel, S.; Eichhorn, C.; Otto, R.; Sun, R.; de Jong, W. A.; Weidemüller, M.; Hase, W. L.; Wester, R. Indirect Dynamics in a Highly Exoergic Substitution Reaction. *J. Am. Chem. Soc.* **2013**, *135* (11), 4250–4259.

(18)   Angel, L. A.; Ervin, K. M. Dynamics of the Gas-Phase Reactions of Fluoride Ions with Chloromethane. *J. Phys. Chem. A* **2001**, *105* (16), 4042–4051.

(19)   Vanorden, S. L.; Pope, R. M.; Buckner, S. W. Energy Disposal in Gas-Phase Nucleophilic Displacement Reactions. *Org. Mass Spectrom.* **1991**, *26* (11), 1003–1007.

(20)   Su, T.; Wang, H.; Hase, W. L. Trajectory Studies of S_N2 Nucleophilic Substitution. 7. $F^- + CH_3Cl \rightarrow FCH_3 + Cl^-$. *J. Phys. Chem. A* **1998**, *102* (48), 9819–9828.

(21)   Lide D. R. *Handbook of Chemistry and Physics*, 84th ed.; CRC Press: Florida, **2003**.

(22)   Cyr, D. M.; Bishea, G. A.; Scarton, M. G.; Johnson, M. A. Observation of Charge-transfer Excited States in the $I^- \cdot CH_3I$, $I^- \cdot CH_3Br$, and $I^- \cdot CH_2Br_2$ S_N2 Reaction Intermediates Using Photofragmentation and Photoelectron Spectroscopies. *J. Chem. Phys.* **1992**, *97* (8), 5911–5914.

(23)   Cyr, D. M.; Bailey, C. G.; Serxner, D.; Scarton, M. G.; Johnson, M. A. The Charge Transfer Excited State of the $I^- \cdot CH_3I$ S_N2 Reaction Intermediate: Photoinduced Intracluster Dissociative Attachment. *J. Chem. Phys.* **1994**, *101* (12), 10507–10520.

(24)   Shaik, S. S.; Pross, A. S_N2 Reactivity of CH_3X Derivatives. A Valence Bond Approach. *J. Am. Chem. Soc.* **1982**, *104* (10), 2708–2719.

(25)   Cyr, D. M.; Scarton, M. G.; Johnson, M. A. Photoelectron Spectroscopy of the Gas-phase S_N2 Reaction Intermediates $I^- \cdot CH_3I$ and $I^- \cdot CD_3I$: Distortion of the CH_3I at the "'Ion-Dipole'" Complex. *J. Chem. Phys.* **1993**, *99* (6), 4869–4872.

(26) Deng, L.; Branchadell, V.; Ziegler, T. Potential Energy Surfaces of the Gas-Phase S_N2 Reactions $X^- + CH_3X = XCH_3 + X^-$ (X = F, Cl, Br, I): A Comparative Study by Density Functional Theory and Ab Initio Methods. *J. Am. Chem. Soc.* **1994**, *116* (23), 10645–10656.

(27) Arnold, C. C.; Neumark, D. M.; Cyr, D. M.; Johnson, M. A. Negative Ion Zero Electron Kinetic Energy Spectroscopy of $I^-\cdot CH_3I$. *J. Phys. Chem.* **1995**, *99* (6), 1633–1636.

(28) Dessent, C. E. H.; Bailey, C. G.; Johnson, M. A. On the Vibrational Fine Structure in the Near-threshold Photofragmentation Spectrum of the $I^-\cdot CH_3I$ Complex: Spectroscopic Observation of Nonadiabatic Effects in Electron-molecule Scattering. *J. Chem. Phys.* **1996**, *105* (23), 10416–10423.

(29) Mabbs, R.; Surber, E.; Sanov, A. Photoelectron Anisotropy and Channel Branching Ratios in the Detachment of Solvated Iodide Cluster Anions. *J. Chem. Phys.* **2005**, *122* (5), 054308.

(30) Van Duzor, M.; Wei, J.; Mbaiwa, F.; Mabbs, R. $I^-\cdot CH_3X$ (X=Cl, Br, I) Photodetachment: The Effect of Electron-Molecule Interactions in Cluster Anion Photodetachment Spectra and Angular Distributions. *J. Chem. Phys.* **2010**, *133* (14), 144303.

(31) Barnola, S.; Posseme, N.; Landis, S.; Darnon, M. 3 - Patterning Challenges in Microelectronics. In *Plasma Etching Processes for CMOS Devices Realization*; Elsevier, **2017**; pp 59–94.

(32) Poulsen, R. G. Plasma Etching in Integrated Circuit Manufacture - A Review. *J. Vac. Sci. Technol.* **1977**, *14* (1), 266–274.

(33) Coburn, J. W.; Winters, H. F. Plasma Etching - A Discussion of Mechanisms. *J. Vac. Sci. Technol.* **1979**, *16* (2), 391–403.

(34) Sarangan, A. 5 - Nanofabrication. In *Fundamentals and Applications of Nanophotonics*; Haus, J. W., Ed.; Woodhead Publishing, **2016**; pp 149–184.

(35) Reif, R.; Chatterjee, R.; Karecki, S.; Pruette, L. Plasma Etching Processes for the Reduction of Global Warming Emissions. In *Digest of Papers Microprocesses and Nanotechnology 2000. 2000 International Microprocesses and Nanotechnology Conference (IEEE Cat. No.00EX387)*; **2000**; pp 266-.

(36) Misra, A.; Sees, J.; Hall, L.; Levy, R. A.; Zaitsev, V. B.; Aryusook, K.; Ravindranath, C.; Sigal, V.; Kesari, S.; Rufin, D. Plasma Etching of Dielectric Films Using the Non-Global-Warming Gas CF_3I. *Mater. Lett.* **1998**, *34* (3), 415–419.

(37) Samukawa, S.; Ichihashi, Y.; Ohtake, H.; Soda, E.; Saito, S. Environmentally Harmonized CF_3I Plasma for Low-Damage and Highly Selective Low-*k* Etching. *J. Appl. Phys.* **2008**, *103* (5), 053310.

(38) Soda, E.; Kondo, S.; Saito, S.; Ichihashi, Y.; Sato, A.; Ohtake, H.; Samukawa, S. Low-Damage Low-*k* Etching with an Environmentally Friendly CF$_3$I Plasma. *J. Vac. Sci. Technol. A* **2008**, *26* (4), 875–880.

(39) Soda, E.; Kondo, S.; Saito, S.; Koyama, K.; Jinnai, B.; Samukawa, S. Mechanism of Reducing Line Edge Roughness in ArF Photoresist by Using CF$_3$I Plasma. *J. Vac. Sci. Technol. B Microelectron. Nanometer Struct. Process. Meas. Phenom.* **2009**, *27* (5), 2117–2123.

(40) Otell, Z. el; Šamara, V.; Zotovich, A.; Hansen, T.; Marneffe, J.-F. de; Baklanov, M. R. Vacuum Ultra-Violet Emission of CF$_4$ and CF$_3$I Containing Plasmas and Their Effect on Low-k Materials. *J. Phys. Appl. Phys.* **2015**, *48* (39), 395202.

(41) Goyette, A. N.; Wang, Y.; Olthoff, J. K. Comparison of the Identities, Fluxes, and Energies of Ions Formed in High Density Fluorocarbon Discharges. *AIP Conf. Proc.* **2001**, *550* (1), 238–242.

(42) Marienfeld, S.; Fabrikant, I. I.; Braun, M.; Ruf, M.-W.; Hotop, H. High Resolution Low-Energy Electron Attachment to CF$_3$I. *J. Phys. B At. Mol. Opt. Phys.* **2006**, *39* (1), 105.

(43) Even, U.; Jortner, J.; Noy, D.; Lavie, N.; Cossart-Magos, C. Cooling of Large Molecules below 1 K and He Clusters Formation. *J. Chem. Phys.* **2000**, *112* (18), 8068–8071.

(44) Bandyopadhyay, B.; Stein, T.; Fang, Y.; Kostko, O.; White, A.; Head-Gordon, M.; Ahmed, M. Probing Ionic Complexes of Ethylene and Acetylene with Vacuum-Ultraviolet Radiation. *J. Phys. Chem. A* **2016**, *120* (27), 5053–5064.

(45) Kohn, W.; Sham, L. J. Self-Consistent Equations Including Exchange and Correlation Effects. *Phys. Rev.* **1965**, *140* (4A), A1133–A1138.

(46) Runge, E.; Gross, E. K. U. Density-Functional Theory for Time-Dependent Systems. *Phys. Rev. Lett.* **1984**, *52* (12), 997–1000.

(47) Yanai, T.; Tew, D. P.; Handy, N. C. A New Hybrid Exchange–Correlation Functional Using the Coulomb-Attenuating Method (CAM-B3LYP). *Chem. Phys. Lett.* **2004**, *393* (1), 51–57.

(48) Peach, M. J. G.; Teale, A. M.; Helgaker, T.; Tozer, D. J. Fractional Electron Loss in Approximate DFT and Hartree–Fock Theory. *J. Chem. Theory Comput.* **2015**, *11* (11), 5262–5268.

(49) Kim, M.-C.; Sim, E.; Burke, K. Communication: Avoiding Unbound Anions in Density Functional Calculations. *J. Chem. Phys.* **2011**, *134* (17), 171103.

(50) Peach, M. J. G.; Benfield, P.; Helgaker, T.; Tozer, D. J. Excitation Energies in Density Functional Theory: An Evaluation and a Diagnostic Test. *J. Chem. Phys.* **2008**, *128* (4), 044118.

(51) Frisch, M. J.; Pople, J. A.; Binkley, J. S. Self-consistent Molecular Orbital Methods 25. Supplementary Functions for Gaussian Basis Sets. *J. Chem. Phys.* **1984**, *80* (7), 3265–3269.

(52) Krishnan, R.; Binkley, J. S.; Seeger, R.; Pople, J. A. Self-consistent Molecular Orbital Methods. XX. A Basis Set for Correlated Wave Functions. *J. Chem. Phys.* **1980**, *72* (1), 650–654.

(53) McLean, A. D.; Chandler, G. S. Contracted Gaussian Basis Sets for Molecular Calculations. I. Second Row Atoms, Z=11–18. *J. Chem. Phys.* **1980**, *72* (10), 5639–5648.

(54) Dunning, T. H.; Hay, P. J. Gaussian Basis Sets for Molecular Calculations. In *Methods of Electronic Structure Theory*; Modern Theoretical Chemistry; Springer, Boston, MA, **1977**; pp 1–27.

(55) Hay, P. J.; Wadt, W. R. Ab Initio Effective Core Potentials for Molecular Calculations. Potentials for K to Au Including the Outermost Core Orbitals. *J. Chem. Phys.* **1985**, *82* (1), 299–310.

(56) Wadt, W. R.; Hay, P. J. Ab Initio Effective Core Potentials for Molecular Calculations. Potentials for Main Group Elements Na to Bi. *J. Chem. Phys.* **1985**, *82* (1), 284–298.

(57) Grimme, S.; Antony, J.; Ehrlich, S.; Krieg, H. A Consistent and Accurate Ab Initio Parametrization of Density Functional Dispersion Correction (DFT-D) for the 94 Elements H-Pu. *J. Chem. Phys.* **2010**, *132* (15), 154104.

(58) Frisch, M. J.; Head-Gordon, M.; Pople, J. A. A Direct MP2 Gradient Method. *Chem. Phys. Lett.* **1990**, *166* (3), 275–280.

(59) Gadhi, J.; Wlodarczak, G.; Legrand, J.; Demaison, J. The Dipole Moments of Methyl Bromide and Methyl Iodide. *Chem. Phys. Lett.* **1989**, *156* (4), 401–404.

(60) Cox, A. P.; Duxbury, G.; Hardy, J. A.; Kawashima, Y. Microwave Spectra of CF_3Br and CF_3I. Structures and Dipole Moments. *J. Chem. Soc. Faraday Trans. 2 Mol. Chem. Phys.* **1980**, *76* (0), 339–350.

(61) Anstöter, C. S.; Bull, J. N.; Verlet, J. R. R. Ultrafast Dynamics of Temporary Anions Probed through the Prism of Photodetachment. *Int. Rev. Phys. Chem.* **2016**, *35* (4), 509–538.

(62)   West, C. W.; Bull, J. N.; Antonkov, E.; Verlet, J. R. R. Anion Resonances of *para*-Benzoquinone Probed by Frequency-Resolved Photoelectron Imaging. *J. Phys. Chem. A* **2014**, *118* (48), 11346–11354.

(63)   Bull, J. N.; West, C. W.; Verlet, J. R. R. On the Formation of Anions: Frequency-, Angle- , and Time-Resolved Photoelectron Imaging of the Menadione Radical Anion. *Chem. Sci.* **2015**, *6* (2), 1578–1589.

(64)   West, C. W.; Bull, J. N.; Hudson, A. S.; Cobb, S. L.; Verlet, J. R. R. Excited State Dynamics of the Isolated Green Fluorescent Protein Chromophore Anion Following UV Excitation. *J. Phys. Chem. B* **2015**, *119* (10), 3982–3987.

(65)   Anstöter, C. S.; Dean, C. R.; Verlet, J. R. R. Chromophores of Chromophores: A Bottom-up Hückel Picture of the Excited States of Photoactive Proteins. *Phys. Chem. Chem. Phys.* **2017**, *19* (44), 29772–29779.

(66)   Bull, J. N.; Verlet, J. R. R. Dynamics of π^*-Resonances in Anionic Clusters of *para*-Toluquinone. *Phys. Chem. Chem. Phys.* **2017**, *19* (39), 26589–26595.

(67)   Rogers, J. P.; Anstöter, C. S.; Verlet, J. R. R. Ultrafast Dynamics of Low-Energy Electron Attachment via a Non-Valence Correlation-Bound State. *Nat. Chem.* **2018**, *10* (3), 341–346.

(68)   Rogers, J. P.; Anstöter, C. S.; Verlet, J. R. R. Evidence of Electron Capture of an Outgoing Photoelectron Wave by a Nonvalence State in $(C_6F_6)_n^-$. *J. Phys. Chem. Lett.* **2018**, *9* (10), 2504–2509.

(69)   Serxner, D.; Dessent, C. E. H.; Johnson, M. A. Precursor of the I_{aq}^- Charge-transfer-to-solvent (CTTS) Band in $I^-\cdot(H_2O)_n$ Clusters. *J. Chem. Phys.* **1996**, *105* (16), 7231–7234.

(70)   Hanstorp, D.; Gustafsson, M. Determination of the Electron Affinity of Iodine. *J. Phys. B At. Mol. Opt. Phys.* **1992**, *25* (8), 1773.

(71)   Wenthold, P. G.; Hrovat, D. A.; Borden, W. T.; Lineberger, W. C. Transition-State Spectroscopy of Cyclooctatetraene. *Science* **1996**, *272* (5267), 1456–1459.

(72)   Neumark, D. M. Transition State Spectroscopy of Bimolecular Chemical Reactions. *Annu. Rev. Phys. Chem.* **1992**, *43* (1), 153–176.

(73)   Kim, J. B.; Weichman, M. L.; Sjolander, T. F.; Neumark, D. M.; Kłos, J.; Alexander, M. H.; Manolopoulos, D. E. Spectroscopic Observation of Resonances in the $F + H_2$ Reaction. *Science* **2015**, *349* (6247), 510–513.

CHAPTER 7 - OUTLOOK

7.1   FUTURE WORK

The experimental data presented throughout this thesis has been obtained using frequency-resolved photoelectron spectroscopy. While this method provides an invaluable insight into the electronic landscape of the molecules in question, there are several cases that have been highlighted in previous discussion sections, where the use of time-resolved spectroscopy may also be beneficial. As such, future investigations into the molecules probed throughout this thesis, should incorporate time-resolved studies to elucidate their dynamics and provide a more comprehensive picture of the molecule's photophysical processes.

In Chapter 4, we demonstrated the use of the basis set stabilisation method in conjunction with time-dependent density functional theory in the characterisation of anion resonances for the polycyclic aromatic hydrocarbon (PAH) anthracene. Though these methods were employed largely as a qualitative aid, the stabilisation method in particular is routinely used to extract quantitative information such as the lifetime of the resonance, which can be ascertained from the width of an avoided crossing.[1] Further work in this area would aim to establish a methodology by which parameters other than the excitation energy can be determined from the stabilisation data. This would prove particularly useful in frequency-resolved studies where it could substantiate proposed decay mechanisms.

The PAH probed in Chapter 4 was selected as a test molecule due its size. Anthracene is the smallest PAH to possess a positive electron affinity,[2] making it suitable for studies using photoelectron spectroscopy and density functional theory. Although PAHs of this size are of importance within optical electronics and astrochemical processes,[3–6] the role of significantly larger PAH ions in the interstellar medium is a topic of particular interest at present, given the recent discovery of C_{60}^+ in this region.[7] While there have been some experimental studies characterising the photochemical properties of larger radical PAH anions such as coronene $(C_{24}H_{12})$,[8,9] computational studies in this area at a quantum mechanical level are lacking,[10] presumably discouraged by the expense associated with calculation of large systems. It would therefore be beneficial to extend the use of the experimental and computational methods employed in Chapter 4 to larger radical PAH anions such as coronene and C_{60} in order to investigate the resonance dynamics of these systems.

However, when putting forward this proposal, one must appreciate the difficulties that may be encountered in the study of larger anions. As already mentioned, the calculation of bigger anions is computationally demanding for density functional theory and necessitates the use of additional resources. Chapter 4 highlighted the difficulty in applying the stabilisation method to the elucidation of higher energy resonances. Larger systems will have a higher number of discretised continuum states and may render the use of the stabilisation method suitable for the lowest lying resonances only.

The investigation of larger systems also presents experimental challenges. The current photoelectron spectroscopy setup detailed in Chapter 2 includes a pulsed valve which can be safely operated at temperatures below 250°C[11] and thus, permits the study of PAH anions no greater in size than tetracene. Therefore, the experimental redesign of the instrument is required if larger systems are to be investigated. In the current setup, the heating element is wrapped around the pulsed valve, allowing the analyte to be vaporised prior to expansion through the valve. Future designs may involve the use of a different type of analyte dispersal mechanism that can operate at significantly higher temperatures or one which allows for the subsequent heating of the solid analyte.

One of the aims of this thesis initially outlined in Section 1.8, was to explore how the immediate environment affects the resonances of studied anions. However, due to time limitations this was only possible for *para*-benzoquinone. Additional studies would apply photoelectron spectroscopy to anthracene-water clusters and other microhydrated PAH anions. Investigations in this area will be of particular relevance to the interstellar medium where PAHs exist in dense molecular clouds at temperatures below 30 K, and often condense on to icy dust grain mantles and thus may contribute to the chemistry occurring locally.[12–14]

An important piece of information that cannot be determined from photoelectron spectroscopy is the geometric configuration of such microhydrated complexes. Chapter 5 exemplified how molecular mechanics can be used to generate a number of minimum energy structures, which could then be refined using density functional theory. Potential experimental PAH-water studies should also incorporate the use of molecular mechanics simulations to determine the minimum energy configuration and ultimately, the charge distribution of the microhydrated clusters. It would also be interesting to extend these computational methods to the *para*-benzoquinone oligomer clusters studied in Chapter 5.1. It should be emphasised that molecular mechanics obtains low energy configurations of the system, *i.e.* local minima. For a

more comprehensive examination of the system's geometric arrangement, further computational investigations should explore the use of global optimisation methods such as Monte Carlo-based techniques or Basin-hopping.[15,16]

To better understand the decay dynamics of $I^-\cdots ICF_3$ (Chapter 6), it would be beneficial to study the photofragmentation products, principally I^- and I_2^-. However, our current experimental arrangement does not permit this as the setup only includes one mass spectrometer which must be used to detect $I^-\cdots ICF_3$. Given the different masses of I^-, I_2^- and $I^-\cdots ICF_3$, the timings at which these anions arrive at the time-of-flight detector would be different, necessitating the use of a second mass spectrometer. As such, extension of the work detailed in Chapter 6 would include modification of the experimental setup to allow for the detect of anions other than $I^-\cdots ICF_3$ and ultimately, the generation of photodissociation action spectra.

7.2 REFERENCES

(1) Simons, J. Molecular Anions. *J. Phys. Chem. A* **2008**, *112* (29), 6401–6511.

(2) Dessent, C. E. H. A Density Functional Theory Study of the Anthracene Anion. *Chem. Phys. Lett.* **2000**, *330* (1), 180–187.

(3) Almeataq, M. S.; Yi, H.; Al-Faifi, S.; Alghamdi, A. A. B.; Iraqi, A.; Scarratt, N. W.; Wang, T.; Lidzey, D. G. Anthracene-Based Donor-Acceptor Low Band Gap Polymers for Application in Solar Cells. *Chem. Commun.* **2013**, *49* (22), 2252–2254.

(4) Chan, W.-L.; Ligges, M.; Jailaubekov, A.; Kaake, L.; Miaja-Avila, L.; Zhu, X.-Y. Observing the Multiexciton State in Singlet Fission and Ensuing Ultrafast Multielectron Transfer. *Science* **2011**, *334* (6062), 1541–1545.

(5) Zimmerman, P. M.; Bell, F.; Casanova, D.; Head-Gordon, M. Mechanism for Singlet Fission in Pentacene and Tetracene: From Single Exciton to Two Triplets. *J. Am. Chem. Soc.* **2011**, *133* (49), 19944–19952.

(6) Roser, J. E.; Ricca, A.; Allamandola, L. J. Anthracene Clusters and the Interstellar Infrared Emission Features. *Astrophys. J.* **2014**, *783* (2), 97.

(7) Campbell, E. K.; Holz, M.; Gerlich, D.; Maier, J. P. Laboratory Confirmation of C_{60}^+ as the Carrier of Two Diffuse Interstellar Bands. *Nature* **2015**, *523* (7560), 322–323.

(8) Abouaf, R.; Diaz-Tendero, S. Electron Energy Loss Spectroscopy and Anion Formation in Gas Phase Coronene. *Phys. Chem. Chem. Phys.* **2009**, *11* (27), 5686–5694.

(9) Bréchignac, P.; Garcia, G. A.; Falvo, C.; Joblin, C.; Kokkin, D.; Bonnamy, A.; Parneix, P.; Pino, T.; Pirali, O.; Mulas, G.; *et al.* Photoionization of Cold Gas Phase Coronene and Its Clusters: Autoionization Resonances in Monomer, Dimer, and Trimer and Electronic Structure of Monomer Cation. *J. Chem. Phys.* **2014**, *141* (16), 164325.

(10) Carelli, F.; Gianturco, F. A. Polycyclic Aromatic Hydrocarbon Negative Ions in Interstellar Clouds: A Quantum Study on Coronene Metastable Anions. *Mon. Not. R. Astron. Soc.* **2012**, *422* (4), 3643–3648.

(11) Rogers, J. Photoelectron Spectroscopy of $(C_6F_6)_n^-$ and $(C_6F_6)I^-$ Clusters in a Novel Instrument. PhD Thesis, Durham University, **2017**.

(12) Michoulier, E.; Noble, J. A.; Simon, A.; Mascetti, J.; Toubin, C. Adsorption of PAHs on Interstellar Ice Viewed by Classical Molecular Dynamics. *Phys. Chem. Chem. Phys.* **2018**, *20* (13), 8753–8764.

(13)   Cook, A. M.; Ricca, A.; Mattioda, A. L.; Bouwman, J.; Roser, J.; Linnartz, H.; Bregman, J.; Allamandola, L. J. Photochemistry of Polycyclic Aromatic Hydrocarbons in Cosmic Water Ice: the Role of PAH Ionization and concentration. *Astrophys. J.* **2015**, *799* (1), 14.

(14)   Bouwman, J.; Cuppen, H. M.; Bakker, A.; Allamandola, L. J.; Linnartz, H. Photochemistry of the PAH Pyrene in Water Ice: The Case for Ion-Mediated Solid-State Astrochemistry. *Astron. Astrophys.* **2010**, *511*, A33.

(15)   Young, D. *Computational Chemistry: A Practical Guide for Applying Techniques to Real World Problems*; John Wiley & Sons: New York, **2002**.

(16)   Wales, D. J.; Doye, J. P. K. Global Optimization by Basin-Hopping and the Lowest Energy Structures of Lennard-Jones Clusters Containing up to 110 Atoms. *J. Phys. Chem. A* **1997**, *101* (28), 5111–5116.